


Precision spectroscopy of molecular hydrogen ions: an introduction

S. Schiller

To cite this article: S. Schiller (2023): Precision spectroscopy of molecular hydrogen ions: an introduction, Contemporary Physics, DOI: [10.1080/00107514.2023.2180180](https://doi.org/10.1080/00107514.2023.2180180)

To link to this article: <https://doi.org/10.1080/00107514.2023.2180180>

 View supplementary material 

 Published online: 01 Sep 2023.

 Submit your article to this journal 

 View related articles 

 View Crossmark data 



Precision spectroscopy of molecular hydrogen ions: an introduction

S. Schiller 

Institut für Experimentalphysik, Heinrich-Heine-Universität Düsseldorf, Düsseldorf, Germany

ABSTRACT

The molecular hydrogen ions (MHI) are composed of only two nuclei and a single electron. These simplest molecules are fascinating systems at the interface of atomic and molecular physics. Compared to atoms, they present the additional degrees of freedom of vibration and rotation. The spectrum of rovibrational energies provides an exceptionally large number of transitions that are potentially measurable with extremely small fractional uncertainty. After two decades of theoretical and experimental efforts, precision studies of the vibrational transition frequencies have now reached fractional uncertainties in the low- 10^{-12} range. This is nearing the level of the most accurate experiment-theory comparisons in physics, performed on the hydrogen atom and on the g-factor of the electron. We describe the motivation for the study of MHI, present some relevant theoretical and experimental issues, indicate a few salient results and give an outlook towards future opportunities.

ARTICLE HISTORY

Received 10 October 2022
Accepted 24 January 2023

KEYWORDS

molecular hydrogen ions;
fundamental constants;
proton radius; electron mass;
proton mass; quantum
electrodynamics

1. Introduction

1.1. The precision physics ecosystem

Precision physics is a field that includes the study of ‘simple’ quantum systems. These are systems where the properties of and interactions between individual particles, rather than the properties of interacting ensembles are of interest. ‘Simple’ does not imply ‘undercomplex’, but rather that an appropriate theory can provide a high and competitive level of accuracy, i.e. a level that matches the accuracy of experimental measurements, at least within an order of magnitude. At present, we are concerned with fractional accuracies in the $10^{-9} - 10^{-13}$ range. Thus, ‘simple systems’ are few-body systems, containing up to three constituents – only for these can current theory predictions reach uncertainty levels lower than approximately 10^{-9} . Accordingly, helium-like atoms are simple but lithium-like atoms and neutral hydrogen molecules (containing 4 particles) are complex. The distinction simple-complex may well evolve since experimental and theoretical accuracy levels improve in the course of time. Advances on the theoretical front often motivate the next generation of measurements, and vice-versa.


Figure 1 gives an overview of a multitude of simple systems. Starting from the left, we have the fundamental constituents of matter: electrons, protons, neutrons, deuterons, positrons, antiprotons, etc. These can all be cooled and trapped in appropriate traps. Traps are

predominantly Penning traps or, in case of neutrons, magnetic bottles. The fundamental properties of the particles are measured, such as the masses (actually, if high accuracy is desired *ratios* of masses of different particles are measured), the g-factors, and in the case of the neutron, also the lifetime. The g-factor measurement of the electron, performed with an accuracy of 1.7×10^{-13} [1] on single electrons in a Penning trap, is a celebrated example because the *ab initio* calculation of the g-factor using quantum electrodynamics (QED) theory provides competitive accuracy.

In the same box ‘single particles’ we include precision measurements on complex atoms, e.g. cesium and rubidium. Although these are many-body systems containing a large number of electrons, their internal complexity may be ignored for certain aspects of the behaviour of the atom as a whole, such as its interaction with radiation and its motion. Thus, atom interferometry is employed to accurately measure the acceleration of gravity and the mass of the atom, with accuracy at the 10^{-10} level.

A second group of systems are two-body systems. The hydrogen atom is its time-honored member. The Rydberg constant is determined mostly from optical spectroscopy of hydrogen. Several other members pertain to the group, in particular the muonic hydrogen and deuterium, that serve to measure the proton and deuteron charge radius, and hydrogenic ions. The low-mass hydrogen-like ions have already had an important impact in the field through

CONTACT S. Schiller  step.schiller@hhu.de

 Supplemental data for this article can be accessed here. <https://doi.org/10.1080/00107514.2023.2180180>

Precision physics with „simple“ quantum systems

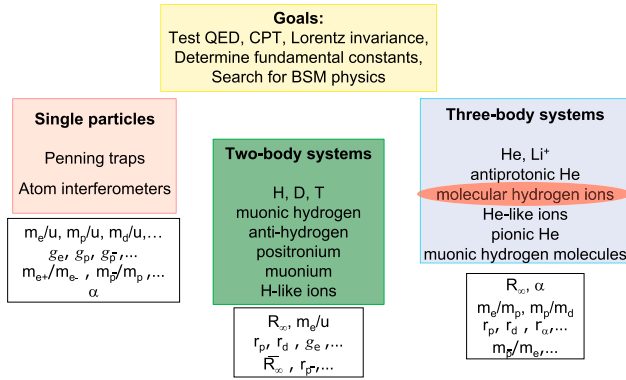


Figure 1. The precision physics ecosystem. The boxes indicate the fundamental constants that can be determined by experiments using the different physical systems. Overbars refer to antimatter. CPT: charge, parity, time reversal; BSM: beyond-the-Standard-Model.

the measurement of the g -factor of the bound electron in He^+ [2] and C^{5+} [3]. High-mass hydrogen-like ions show promise as test beds for the theory of QED in strong electric field. Muonium (the bound state of a positive muon and an electron) is of interest as a pure leptonic system, therefore promising particularly clean tests of QED.

Progressing to more complicated systems, we have three-body systems. These comprise first of all the classic helium atom. Theory and measurement of its electronic fine structure can be combined to determine the fine structure constant α . Precision measurements and theory on trapped and cooled helium-like ions may in the future provide improved determinations of α or searches for hypothetical ‘beyond-the-Standard-Model’ (BSM) forces between electrons.

A family of three-body systems that has become relevant in the context of precision measurements are the molecular hydrogen ions (MHI). Six different isotopologues exist, three homonuclear (H_2^+ , D_2^+ , T_2^+) and three heteronuclear (HD^+ , HT^+ , DT^+). A visualisation of these systems by their electron cloud is presented in Figure 2.

The goal of this paper is to furnish an introduction aimed at non-specialists. Focusing on recent developments, the paper is complementary to very early reviews on the precision physics of MHI [4–6] and also to an overview of some more recent developments until 2015 [7]. A detailed introduction to the elementary non-relativistic physics of the MHI is given in the textbook on quantum mechanics by Cohen-Tannoudji, Diu and Laloe; that treatment will not be repeated here.

It is planned to make available updates and corrections to this paper online [8].

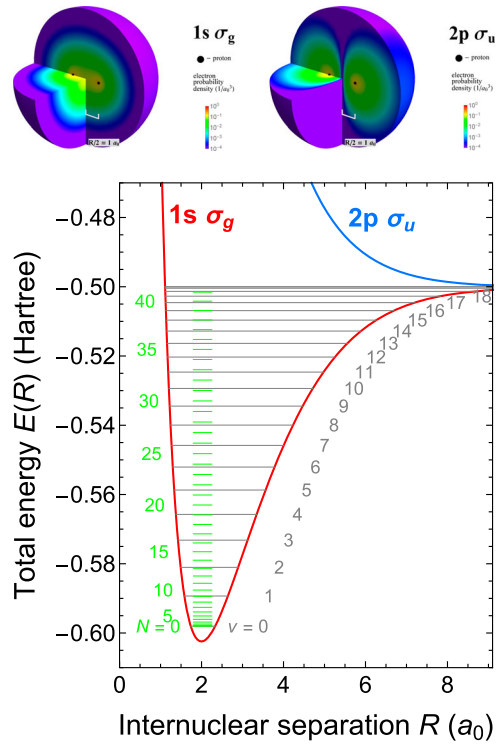


Figure 2. Top: The electron probability density (electronic wave function squared) of the two lowest-energy electronic states of the MHI. It is very nearly equal for all MHI isotopologues. The chosen distance R between the two nuclei corresponds to the mean bond length R_e in the ground rovibrational level $v = 0$, $N = 0$ (Figure by M.R. Schenkel). Bottom: Total (nuclear plus electronic) energy $E(R)$ of the MHI, and a subset of rovibrational energy levels of HD^+ . The gray lines denote the rotationless vibrational level energies $E(v, N = 0)$, while the green lines are the rotational ladder of the vibrational ground state, $E(v = 0, N)$. $1 \text{ Hartree} = 2E_R \simeq 27.2 \text{ eV}$.

Briefly, the contents is as follows: in the remainder of this first chapter the physics motivation is detailed, and some historical remarks are given. There follow Chapter II, presenting the fundamentals of MHI, Chapter III on the experimental studies of MHI performed in the past several years. In Chapter IV precision theory is confronted to precision experiments. Chapter V deals with applications in fundamental physics, Chapter VI and VII offer an extended outlook and a short conclusion, respectively. We point to an extended Supplemental Material available online, treating explicitly the quantum theory of the hyperfine structure and of the Zeeman effect.

1.2. Motivation

Why are studies of MHI important, given that there are so many other systems that can be studied with high accuracy? The emerging answer is that they provide a new

link between the fields of one-body systems and two-body systems. In concrete terms, it is a link between the field of mass measurements of simplest charged particles in Penning traps (mass spectrometry of electron, proton, deuteron, triton) and the determination of the properties of the hydrogen atom, i.e. the binding energies of a single electron to a single simple nucleus (Rydberg constant), and the charge radii of the simplest nuclei. Put in flashy terms, MHI effectively realise a miniature, high-accuracy mass spectrometer for the masses of electron, proton, deuteron and triton. Decades ago, before the advent of the Penning traps, diatomic molecules were considered to be systems suitable for precisely determining the masses of isotopes. At least for the isotopes of hydrogen, this is now becoming a reality, thanks to the huge advances both in experimental techniques and in the *ab initio* theory of the MHI. In addition, MHI potentially offer an alternative approach to determination of the Rydberg constant and the nuclear charge radii.

Concerning fundamental aspects, the MHI are of interest because the motion of and the force between two baryons (the nuclei) are a crucial aspect. This force is not present in any atom. In this sense, the MHI are complementary to the ‘simple’ atomic systems: in hydrogen only the force between a lepton and a baryon is of relevance. In two-electron systems (helium and helium-like ions, neutral molecular hydrogen), the electron–electron (lepton–lepton) interaction is also involved. The hydrogen atom, the MHI, and the helium-like atoms form a triad on which to test for the existence of BSM forces between any of the fundamental (i.e. simplest) stable constituents of matter.

This triad does not exhaust all possible forces, since there also exists antimatter. Obviously, the corresponding antimatter systems could be studied with the same aim concerning anti-matter forces, and this is in part already being done: on anti-hydrogen. Finally, there are ‘hybrid’ systems, such as antiprotonic helium and positronium, that could search for BSM forces between matter and antimatter. In Section 5.2 we shall mention additional topics in fundamental physics accessible to the MHI.

1.3. Brief historical notes on spectroscopy of MHI

Over the decades, spectroscopy of MHI has been performed in a number of ways by several research groups. Key efforts may be categorised as follows (additional references appear in the subsequent text):

- 1960s – end 1980s: magnetic resonance and spin resonance of trapped MHI ensembles at room temperature (Dehmelt et al., Jefferts, Werth et al. [9])

- 1969–1970: first observations of rovibrational energies by classical optical and photoelectron spectroscopy (Herzberg et al., Takezwa, Asbrink; see ref. [10] and refs therein)
- mid-1970s – end 1990s: laser and microwave spectroscopy of MHI beams (Lamb et al. [11], Carrington et al.)
- late 1980s – ongoing: laser and microwave spectroscopy of Rydberg states of neutral molecular hydrogen (Lundeen et al. [12], Merkt et al. [13])
- 2005 onward: rotational and vibrational spectroscopy on trapped and sympathetically cooled MHI ensembles (Universität Düsseldorf [14]; Univ. Amsterdam)
- 2021 onward: single MHI in a radiofrequency trap [15,16] and in a Penning trap (with nondestructive spectroscopy [17]).

The experimental research of the last two decades on trapped MHI has focused on studying the MHI that is most practical: HD^+ . It is heteronuclear and non-radioactive. Experiments are in preparation to tackle other MHI as well.

2. Fundamentals of MHI

2.1. Electronic and rovibrational energies

In the present tutorial, it is sufficient to consider the two lowest-energy electronic states of the MHI, the $1s\sigma_g$ ground state and the higher-energy $2p\sigma_u$ state. We depict the squared electronic wave functions in Figure 2 top. These two wave functions are axially symmetric (σ) around the line joining the nuclei, implying zero electronic angular momentum around the nuclear axis. Furthermore, in case of H_2^+ , these wave functions are, respectively, mirror symmetric and antisymmetric with respect to a plane orthogonal to this line and placed at its midpoint, and inversion symmetric (g) and antisymmetric (u) with respect to the mid-point. In case of HD^+ these symmetries are slightly violated; the electron’s mean axial position deviates from the midpoint by $\simeq 6 \times 10^{-4} a_0$ towards the deuteron. The notation of the states carries information about the atomic character acquired in the united-nucleus limit: it can easily be pictured that when the separation R between the two nuclei is hypothetically made to go to zero, the $1s\sigma_g$ state becomes the $1s$ ground state of a fictitious helium ion (nuclear charge $Z_{\text{nuc}} = 2e$), while the $2p\sigma_u$ state becomes its first excited electronic state, the $2p$ state.

Let us introduce the total non-relativistic energy $E_{\text{BO}}(R)$ as the sum of the electron’s energy (kinetic plus potential) and the potential energy associated with the

repulsion between the nuclei, assumed to be fixed in space at a distance R . The state $1s\sigma_g$ is a bound molecular state: as a function of R , a moderately deep minimum of the total energy (2.79 eV, one fifth of the Rydberg energy $E_R = m_e c^2 \alpha^2 / 2$) occurs at a distance R_e nearly equal to 2 Bohr radii (a_0). The minimum arises from a subtle interplay between the electron's (negative) potential energy in the field of the two nuclei, its (positive) kinetic energy and the (positive) nuclear repulsion energy. At $R = R_e$, the first ($-2.4E_R$) is substantially larger in absolute terms than the sum of the latter two, the kinetic energy being $\simeq +1.2E_R$ and the nuclear repulsion being $\simeq +E_R$.

The $2p\sigma_u$ state on the other hand does not exhibit any deep minimum, only a very shallow minimum at large internuclear separation, $R'_e \simeq 12.5a_0$ [18]. In the context of the present discussion, the $2p\sigma_u$ state is only important for enabling photodissociation spectroscopy, see Section 3.1.4.

The concept of a total energy $E_{BO}(R)$ results from the Born-Oppenheimer approximation, i.e. a separation of electronic and nuclear dynamics based on the fact that the electron's motion adapts nearly instantaneously to changes in the positions of the nuclei. Such changes do indeed occur, since the nuclei may vibrate against each other and rotate in space. (Even if these motions are minimised, zero-point motion remains.) In an improved, so-called 'adiabatic' approximation $E(R)$, one can include the effects of the finite speed of the electron at lowest order and also the relativistic corrections of the electron's kinetic energy at lowest order. These adiabatic corrections are isotopologue-dependent.

The function $E(R)$ [19] becomes an effective potential for nuclear motion: the rotations and vibrations of the two nuclei occur in this potential. These two types of motion are quantised, i.e. discrete energies $E(\nu, N)$ result, indicated in Figure 2 bottom. Here, we introduce the basic quantum numbers of the MHI, the vibrational quantum number $\nu = 0, 1, 2, \dots$ and the rotational quantum number $N = 0, 1, 2, \dots$. The energies $E(\nu, N)$ are the solutions of a one-dimensional Schrödinger equation for nuclear motion, that also furnishes the nuclear wavefunctions.

One can find an early calculation of the adiabatic energies in ref. [19]. There it was shown that for the case of HD^+ the largest possible vibrational quantum number is $\nu_{\max} = 21$, and the largest rotational quantum number is $N_{\max} = 41$, occurring for $\nu = 0$. More precise later calculations [20] showed that there exists an additional weakly bound vibrational level with $\nu = 22$ (the corresponding nuclear wavefunction has 22 nodes!). Thus, a total of 637 rovibrational levels exist. These numbers change for the other MHI, because of their differing

reduced nuclear masses, the crucial parameter entering the nuclear Schrödinger equation. The surprising and fascinating aspect of the level structure is that most levels (the fraction is estimated as 80%) have natural lifetimes larger than 10 ms, which qualifies them as metastable (see Section 2.4.2).

Transitions between rovibrational levels can be induced by applying appropriately tuned radiation from a huge spectral range, from THz to UV. As described in Section 2.4.1, in heteronuclear MHI, excitation rates are large only for transitions obeying the rotational selection rule $\Delta N = N' - N = \pm 1$. (Unprimed (primed) quantities refer to the lower (upper) state). Electric-dipole (E1) transitions are transitions of this kind. There is no strict vibration selection rule for $\Delta \nu = \nu' - \nu$. Thus, there are on the order of 8 000 E1 transitions, most of which will have a very high natural quality factor (transition frequency divided by natural linewidth) exceeding 1×10^{12} , because both upper and lower level are metastable.

2.2. Elementary considerations

2.2.1. The rotational transition frequencies

Consider a dumbbell model of a diatomic molecule, the two nuclei of mass m_1, m_2 being rigidly connected to each other at a distance R_e (Figure 3). The rotation of the molecule is quantised. This is described by the rotational hamiltonian (first discussed by Schrödinger in 1926)

$$H_{\text{rot}} = \frac{\mathbf{N}^2}{2I_0},$$

where \mathbf{N} is the rotational angular momentum and I_0 is the moment of inertia around the centre of mass. Quantisation of angular momentum implies that the energies are $E_{\text{rot}}(N) = \hbar^2 N(N+1)/2I_0$. If we neglect the electron's mass, we can express $I_0 = \mu R_e^2$, in terms of the internuclear separation and of the reduced nuclear mass $\mu = m_1 m_2 / (m_1 + m_2)$. Expressing R_e in units of the Bohr radius a_0 , and the reduced nuclear mass in units of the

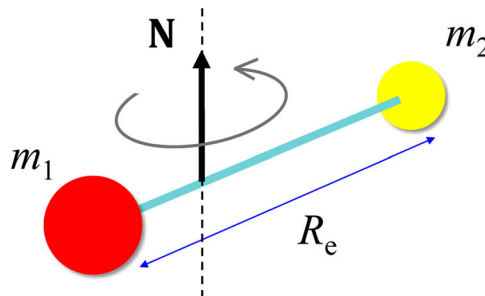


Figure 3. A simple model for a quantum rotor: two masses are rigidly connected and rotate around an axis going through the centre of mass. The angular momentum \mathbf{N} is quantised.

electron mass m_e , we obtain

$$E_{\text{rot}}(N) = N(N+1) \left(\frac{a_0}{R_e} \right)^2 \frac{m_e}{\mu} E_R.$$

This shows that the rotational energies are proportional to the Rydberg energy $E_R \simeq 13.6$ eV, rescaled by the ratio of electron mass to reduced nuclear mass.

The transition frequency between the non-rotating state $N = 0$, and the first excited rotational state $N = 1$ (semiclassically, the slowest rotating dumbbell) is thus

$$f_{\text{rot}} = 2 \left(\frac{a_0}{R_e} \right)^2 \frac{m_e}{\mu} cR_\infty. \quad (1)$$

We have expressed the rotational transition frequency in terms of the Rydberg constant R_∞ , where $cR_\infty = E_R/h \simeq 3.3 \times 10^{15}$ Hz. Since $R_e \simeq 2a_0$ and $\mu/m_e \simeq 1.2 \times 10^3$ for HD^+ , the fundamental rotational frequency is $f_{\text{rot}} \simeq 1.3$ THz.

Classically, the rotating dumbbell molecule with dissimilar masses m_1, m_2 but equal nuclear charges $Z_1 = Z_2$ represents a rotating electric dipole because the rotation is around the centre of mass while the ‘centre of charge’ is midway between the two masses, the electron’s charge being smeared out symmetrically over the molecule, Figure 2. Therefore, one can expect that transitions between rotational states can be excited by an alternating electric field. These are electric-dipole (E1)-allowed transitions in the THz range.

2.2.2. The vibrational transition frequencies

We proceed to estimate the vibrational frequency of a diatomic molecule characterised by an effective nuclear potential $E(R)$ as in Figure 2. Near the minimum at $R = R_e$, the variation will be approximately quadratic, $E(R) \simeq k(R - R_e)^2/2$, with the force constant $k = d^2E(R_e)/dR^2$. So, we have a harmonic oscillator system for a fictitious nuclear particle of mass equal to the reduced mass μ . The classical vibrational frequency is then

$$f_{\text{vib}} = \frac{1}{2\pi} \sqrt{\frac{k}{\mu}}.$$

Quantum-mechanically, the vibrational level energies are $E_{\text{vib}}(\nu) = (\nu + \frac{1}{2})hf_{\text{vib}}$. We wish to estimate the value of the force constant k . Because the MHI is a system bound by the Coulomb forces between singly-charged nuclei and the electron, the potential well has a width on the order of the Bohr radius and its depth is of the order of the Rydberg energy E_R . The actual depth is one-fifth of that. Therefore, $k \sim \mathcal{O}(E_R/a_0^2)$. This can be re-expressed

as $\mathcal{O}(m_e(cR_\infty)^2)$, resulting in

$$f_{\text{vib}} \sim \frac{\mathcal{O}(1)}{2\pi} \sqrt{\frac{m_e}{\mu}} cR_\infty.$$

The transition frequency between two vibrational energy levels ν, ν' is $f_{\nu\nu'} = (E_{\text{vib}}(\nu') - E_{\text{vib}}(\nu))/h = (\nu' - \nu)f_{\text{vib}}$. These transition frequencies scale with the Rydberg frequency, as do the rotational frequencies, but their scaling with the reduced mass is different. Also, the vibrational frequencies are substantially higher than the rotational frequency: $f_{\text{vib}} \simeq 60$ THz for HD^+ .

The first-order dependencies of the rotational and vibrational frequencies on the mass ratio μ/m_e and on the Rydberg constant R_∞ are the key points of interest for the field of metrology of fundamental constants. As ν, ν' become larger than 1, the dependencies deviate increasingly from the simple square-root or linear dependencies, but remain important for most transitions, if not all. The precise dependencies can be calculated (Section 2.3.6). It is useful to contrast them with those in a hydrogen-like atom. For a nuclear mass m_n the non-relativistic transition frequencies are given by $f_i(m_n) = f_i(\infty)/(1 + m_e/m_n)$, where $f_i(\infty)$ are the frequencies of the infinite-nuclear mass system and depend only on the electron mass. The fractional mass shift $f_i(m_n)/f_i(\infty) - 1 \simeq -m_e/m_n$ is particularly large for the light atoms hydrogen, deuterium and tritium, but still a factor $2m_e/m_n$ smaller compared to an MHI vibrational frequency. The atomic mass shift is therefore not large enough for determining the hydrogen isotope masses at a competitive level.

2.3. Precision theory

2.3.1. Overview

We have so far presented rough estimates and introduced the adiabatic approximation. While the latter reflects the theory status of half a century ago, the energies of the states in the $1s\sigma_g$ manifold can nowadays be computed with exquisite accuracy, *ab initio*. This is the result of work by V. I. Korobov, D. Bakalov, J.-Ph. Karr, L. Hilico and coworkers, spanning two decades [21]. The theoretical effort was in part triggered [22] by the plans of precision spectroscopy experiments that were conceived in the late 1990s by the author and his team [23] and spurred by the early experimental developments at the Universität Düsseldorf [14,24]. It is not possible or necessary to give a complete account of the theory, here; instead we shall highlight a few aspects only.

The *ab initio* energy of a rovibrational level, ignoring the influence of the magnetic moments of the constituents but not of the electron spin, is denoted by

$E_{\text{spin-avg}}$ and can be separated into three contributions,

$$E_{\text{spin-avg}}(\nu, N) = E_{\text{nonrel}}(\nu, N) + E_{\text{rel}}(\nu, N) + E_{\text{QED}}(\nu, N). \quad (2)$$

$E_{\text{spin-avg}}$ contains first of all the non-relativistic energies $E_{\text{nonrel}}(\nu, N)$. Their computation is a solved problem. Next, the relativistic energies $E_{\text{rel}}(\nu, N)$. They have been computed with accuracy such that the resulting uncertainties on the transition frequencies are smaller than 10^{-12} fractionally and thus do not affect the interpretation of the current experiments [25]. Third, the computation of $E_{\text{QED}}(\nu, N)$, the energy contribution arising from QED, has been and continues to be a very challenging problem.

Finally, due to the non-zero magnetic moments of the particles, there occurs a hyperfine structure (HFS, spin structure) in each level (ν, N) , with several spin states, except in special cases. Different spin states are denoted by p and have corresponding (positive or negative) ‘spin’ energies $E_{\text{spin}}(\nu, N, p)$. The total energy E_{tot} of a particular quantum state (ν, N, p) is given by

$$E_{\text{tot}}(\nu, N, p) = E_{\text{spin-avg}}(\nu, N) + E_{\text{spin}}(\nu, N, p). \quad (3)$$

A weighted average over all spin states’s total energies for given ν, N , yields the spin-averaged energy $E_{\text{spin-avg}}(\nu, N)$ [26], explaining its name. Only very recently, also the computation of the spin energies with uncertainty at the level of today’s most accurate experiments has been accomplished.

In experimental studies, one measures frequencies of individual spin (HFS) components $i: p \rightarrow p'$ of a rovibrational transition $(\nu, N) \rightarrow (\nu', N')$ (‘lines’):

$$f(\nu, N, p \rightarrow \nu', N', p') = (E(\nu', N', p') - E(\nu, N, p))/h.$$

Following Equation (3) this frequency is split into a spin-averaged and a purely spin contribution,

$$\begin{aligned} f(\nu, N, p \rightarrow \nu', N', p') &= f_{\text{spin-avg}}(\nu, N \rightarrow \nu', N') \\ &\quad + f_{\text{spin}}(\nu, N, p \rightarrow \nu', N', p'), \\ f_{\text{spin}}(\nu, N, p \rightarrow \nu', N', p') &= (E_{\text{spin}}(\nu', N', p') \\ &\quad - E_{\text{spin}}(\nu, N, p))/h. \end{aligned}$$

To a pair (p, p') we may assign a sequence number i , so that the ‘spin frequency’ may be abbreviated as $f_{\text{spin}, i}$ and the rovibrational spin component frequency (line) as $f_{\text{line } i}$.

The main aspects of the four energy contributions are as follows.

1. E_{nonrel} : This is the largest contribution; it is the energy obtained from the solution of the Schrödinger

equation for the MHI, *nota bene* a Schrödinger equation for the *three* particles, in the centre of mass frame. This is therefore non-relativistic physics. It should be pointed out that for the axially symmetric $1s\sigma_g$ state the three-body Schrödinger equation reduces to a second-order partial differential equation in three scalar variables: these can be taken to be the nuclear separation R , and the two distances of the electron from the two nuclei, r_1, r_2 . This equation must be solved without any approximation (i.e. without assuming that m_e/m_n is small) in order to guarantee sufficient accuracy for confrontation with experiment. The solution method [22] is reviewed in ref. [27]. It is a variational expansion containing a very large set of appropriately chosen three-body basis wavefunctions, typically, 5000–20,000. The expansion coefficients are the variational parameters. They are optimised to find stationary values of the energy E_{nonrel} . Note that these are of the order of $-E_R$ (Figure 2). They are accurate to approximately 20 digits. This is so high that at present it does not limit the accuracy of the total energy E_{tot} . In fact, it is the difference between two such rather large energies, $E_{\text{nonrel}}(\nu', N') - E_{\text{nonrel}}(\nu, N)$, which must be computed with appropriately high accuracy because it is the dominant contribution to any transition frequency f . This is particularly important for the fundamental rotational transition, where the transition frequency is only a small fraction of the level energies, $hf_{\text{rot}} \simeq E_{\text{nonrel}}(\nu, N = 1) - E_{\text{nonrel}}(\nu, N = 0) \simeq 4 \times 10^{-4} E_R$.

2. E_{rel} : As for atoms, a non-relativistic description of the MHI is insufficient if high accuracy of the energy values is desired. Qualitatively speaking, the electron in the $1s\sigma_g$ state has a momentum that is weakly relativistic, on the order of $p \sim m_e \alpha c$. This is the same situation as in the $1s$ state of hydrogen. In the Taylor expansion of the electron’s kinetic energy,

$$\sqrt{m_e c^2 + (cp)^2} \simeq m_e c^2 + \frac{p^2}{2m_e} - \frac{(p^2/2m_e)^2}{2m_e c^2} + \dots,$$

the third term represents one of the two dominant relativistic corrections. It can be evaluated in first-order perturbation theory; numerically it is of order $-E_R^2/(2m_e c^2) = -\alpha^2 E_R/4$. The precise relativistic correction E_{rel} contains in addition the equally important Darwin term for the electron, and much smaller nuclear terms, terms that scale in the same way with α [25]. Thus, the total E_{rel} is of order $\alpha^2/4 \simeq 10^{-5}$ smaller than the non-relativistic energy.

3. E_{QED} : This energy arises from the interaction of the electron with the radiation field. For the MHI, where the electron is weakly relativistic, it has been computed by perturbation theory, applied to the non-relativistic QED (NRQED) expansion (for a tutorial, see [28]). The

Table 1. Contributions to the *ab initio* spin-averaged frequency $f_5^{(\text{theor})} = f_{\text{spin-avg}}(0, 0 \rightarrow 5, 1)$ [49].

Relative order	Value (kHz)	Contributions
α^0	259,760,034,608.88	energies from 3-body Schrödinger equation, non-relativistic
α^2	4,008,944.07	Relativistic corrections in Breit–Pauli approximation; finite-size nuclei ([†])
α^3	−1,065,424.00	Leading-order radiative corrections (e.g. leading-order Lamb shift, anomalous magnetic moment of electron)
α^4	−7,544.12	1-loop, 2-loop radiative corrections; more relativistic corrections
α^5	468.43	Radiative corrections up to 3-loop diagrams; Wichmann–Kroll contribution
α^6	−3.39	Higher-order radiative corrections (1-loop self-energy, 2-loop radiative)
Other	1.11	Muonic and hadronic vacuum polarisation corrections for the electron
Total	259,762,971,051.0	Uncertainty of QED contributions: 2.1 kHz

Notes: The computation of the QED contributions (relative order α^3 and higher) employed NRQED theory and followed ref. [50]. A total of 41 individual contributions were calculated for both upper and lower rovibrational levels. The left column indicates the order relative to the transition frequency, which itself is of order $cR_\infty\sqrt{m_e/\mu} = \alpha^2 m_e c^2 \sqrt{m_e/\mu}/2h$. The named individual contributions in column 3 are a subset of those included. ([†]) The term of relative order α^2 includes the nuclear volume shift, $-73.0(3)_{\text{CODATA18}}$ kHz from the proton and $-465.9(3)_{\text{CODATA18}}$ kHz from the deuteron. These uncertainties arise from the uncertainties or the nuclear charge radii. The 2-loop radiative corrections have contributions of different orders. From [51].

calculation builds on the extensive theoretical work performed for the hydrogen atom over more than half a century. The perturbation theory expresses E_{QED} as a power series in the inverse electron mass, in the inverse nuclear mass, and in α . The α -series coefficients have themselves a dependence on α , for example containing contributions proportional to $\ln(\alpha^{-2})$. Here, we will not describe the calculation of E_{QED} [7], but we mention two aspects. First, the largest QED energy contribution is of order $\alpha^3 E_R$; this results in a very relevant contribution to the transition frequencies, see Table 1. Second, the uncertainty with which E_{QED} can today be computed is a crucial limitation for the reach of MHI spectroscopy. The uncertainty amounts to $u_{r,\text{QED}} \simeq 8 \times 10^{-12}$ for vibrational transition frequencies between level pairs with small or moderately large ν, ν' . For the fundamental rotational frequency the uncertainty is approximately twice as large [21]. $u_{r,\text{QED}}$ stems from not-yet calculated contributions that also limit the accuracy of the theory of the hydrogen atom: the contributions of order $R_\infty\alpha^6$ and higher to the one-loop self-energy [29] and to the two-loop radiative corrections [30] for the electron. These could so far only be computed up to residual uncertainties.

4. Finally, the spin energy E_{spin} is due to the interactions between the magnetic moments carried by the particles and the magnetic fields generated by the electron motion, the nuclear magnetic field and the molecular rotation. When a MHI contains a deuterium nucleus, notably in HD^+ , its non-zero electric quadrupole moment Q_d gives rise to a further interaction, with the gradient of the electric field at its location. The first theoretical account of spin interactions (for H_2^+) goes back more than 60 years [31], well before the first experimental observation [32]. Subsequent refined theory work allowed interpreting the HFS observed in experiments of the 1960s to 1980s. Starting 15 years ago,

an *ab initio* theory of the spin interactions has been developed [33–40]. Here, one derives an effective hamiltonian $H_{\text{spin}}(\nu, N)$ by obtaining the spin interactions from an expansion in orders of α and projecting the general hamiltonian onto the manifold of spin states with definite values of ν and N .

2.3.2. Hyperfine structure theory: principles

(a) HD^+

In the following, we emphasise this molecule, because it is the subject of the recent experimental studies.

The spin interactions in HD^+ are expressed in terms of the angular momentum operators $\mathbf{s}_e, \mathbf{I}_p, \mathbf{I}_d, \mathbf{N}$. Here, proton spin $I_p = 1/2$, deuteron spin $I_d = 1$, electron spin $s_e = 1/2$, rotation $N = 0, 1, \dots$. The situation is depicted in Figure 4 top.

The spin hamiltonian contains a perhaps surprisingly large number of terms [33],

$$\begin{aligned}
 H_{\text{spin}}(\nu, N) = & \mathcal{E}_1 \mathbf{N} \cdot \mathbf{s}_e + \mathcal{E}_2 \mathbf{N} \cdot \mathbf{I}_p + \mathcal{E}_3 \mathbf{N} \cdot \mathbf{I}_d \\
 & + \mathcal{E}_4 \mathbf{I}_p \cdot \mathbf{s}_e + \mathcal{E}_5 \mathbf{I}_d \cdot \mathbf{s}_e \\
 & + \mathcal{E}_6 \left\{ 2\mathbf{N}^2 (\mathbf{I}_p \cdot \mathbf{s}_e) - 3 [(\mathbf{N} \cdot \mathbf{I}_p) (\mathbf{N} \cdot \mathbf{s}_e) \right. \\
 & \left. + (\mathbf{N} \cdot \mathbf{s}_e) (\mathbf{N} \cdot \mathbf{I}_p)] \right\} \\
 & + \mathcal{E}_7 \left\{ 2\mathbf{N}^2 (\mathbf{I}_d \cdot \mathbf{s}_e) - 3 [(\mathbf{N} \cdot \mathbf{I}_d) (\mathbf{N} \cdot \mathbf{s}_e) \right. \\
 & \left. + (\mathbf{N} \cdot \mathbf{s}_e) (\mathbf{N} \cdot \mathbf{I}_d)] \right\} \\
 & + \mathcal{E}_8 \left\{ 2\mathbf{N}^2 (\mathbf{I}_p \cdot \mathbf{I}_d) - 3 [(\mathbf{N} \cdot \mathbf{I}_p) (\mathbf{N} \cdot \mathbf{I}_d) \right. \\
 & \left. + (\mathbf{N} \cdot \mathbf{I}_d) (\mathbf{N} \cdot \mathbf{I}_p)] \right\} \\
 & + \mathcal{E}_9 \left[\mathbf{N}^2 \mathbf{I}_d^2 - \frac{3}{2} \mathbf{N} \cdot \mathbf{I}_d - 3 (\mathbf{N} \cdot \mathbf{I}_d)^2 \right].
 \end{aligned} \tag{4}$$

This form is consistent with current experimental results. Additional small contributions are discussed in ref. [41]. The nine spin hamiltonian coefficients

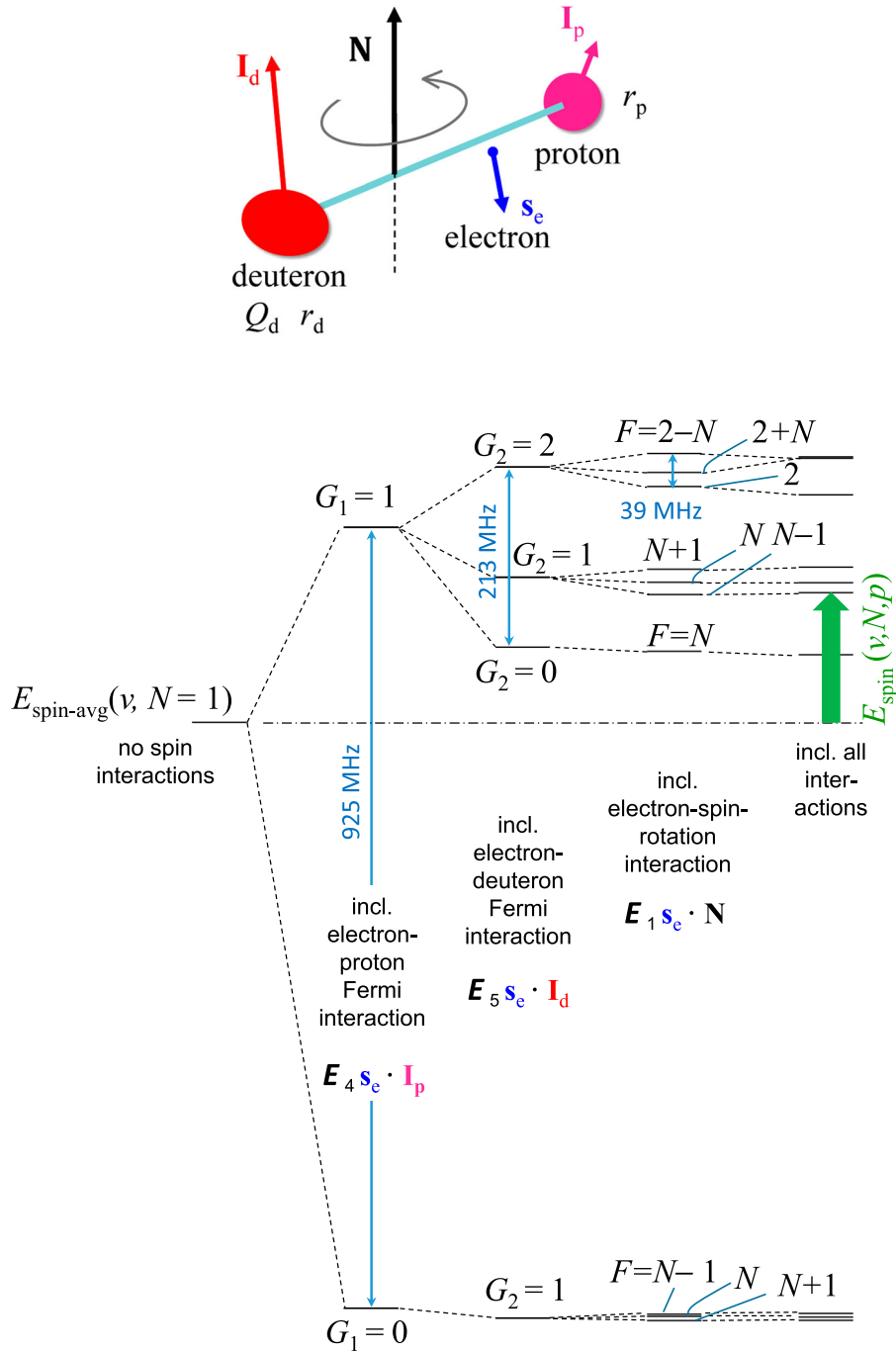


Figure 4. Top: Angular momenta and quadrupole moment in HD^+ . Bottom: The spin structure for a rovibrational level with $N = 1$, indicating the effect of ‘turning on’ the main interactions in sequence, proportional to \mathcal{E}_4 , \mathcal{E}_5 , \mathcal{E}_1 , and finally to all remaining \mathcal{E}_i . The numerical values of the splittings apply to $\nu = 0$. G_1 is an approximate quantum number for the coupling of electron and proton spin, G_2 for the coupling of G_1 and the deuteron spin, and F refers to coupling of G_2 and the rotational angular momentum N .

$\mathcal{E}_1(\nu, N), \dots, \mathcal{E}_9(\nu, N)$ are functions of the rovibrational level and can be nowadays computed *ab initio* with impressive accuracy. The eigenstates of this hamiltonian are the spin (or hyperfine) states $\{p\}$, collectively referred to as spin (HFS) structure.

We may take as basis for the description of the spin structure of a given rovibrational level the states resulting from the addition (coupling) of the angular

momenta \mathbf{s}_e , \mathbf{I}_p , \mathbf{I}_d , \mathbf{N} . Independently of the particular sequence in which they are added, one finds that there are 4 eigenstates of total angular momentum if $N = 0$, 10 if $N = 1$, and 12 if $N \geq 2$. These numbers hold when the orientational degree of freedom of the total angular momentum is ignored. These states are non-degenerate because of the couplings contained in the hamiltonian. Examples can be seen in Figures 4

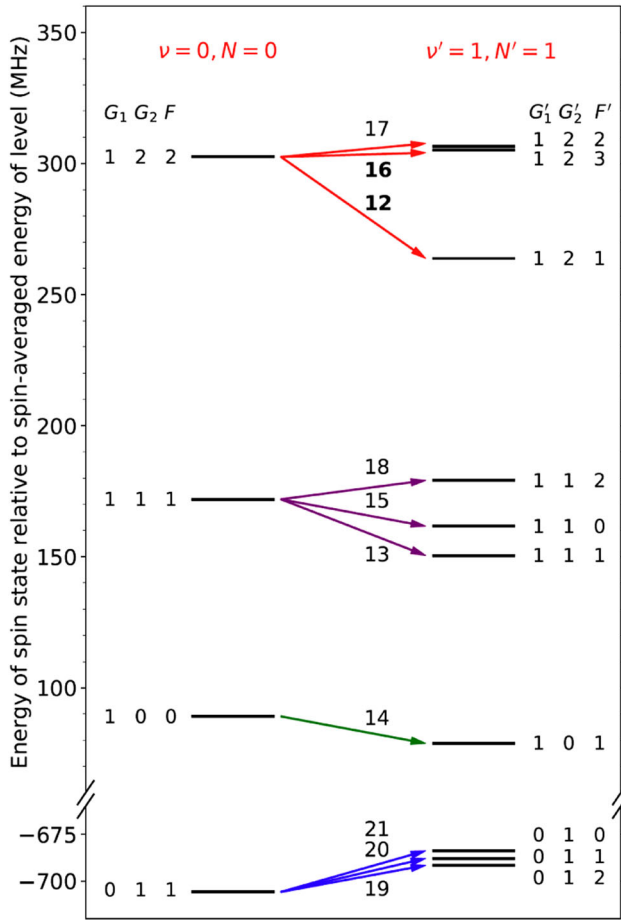


Figure 5. Hyperfine structure of a $N = 0$ and a $N' = 1$ level of HD^+ and the favoured electric-dipole (E1) transitions, in zero magnetic field. These transitions (coloured arrows) connect lower (p) and upper (p') hyperfine states that have the same particle spin coupling, $G_1 = G_1'$ and $G_2 = G_2'$. The transitions are given a line label $i = i(p, p')$. Their frequencies are $f_{\text{line},i} \simeq 58 \text{ THz}$. G_1, G_2, F are approximate or exact quantum numbers that identify the spin state $p = (G_1, G_2, F)$. Black lines on the left indicate spin states p and the values $E_{\text{spin}}(\nu, N, p)/h$ for the lower rovibrational level, on the right they are $E_{\text{spin}}(\nu', N', p')/h$ for the upper level. Energy differences between the left and right black lines correspond to spin frequencies $f_{\text{spin},i}$. The ground rovibrational level has zero rotational angular momentum, $N = 0$, giving rise to 4 spin states with total angular momentum $F = 0, 1, 2$. Levels with $N = 1$ exhibit more (10) spin states because of the additional angular rotational momentum, and the additional spin interactions. The additional splittings seen in $N = 1$ compared to $N = 0$ are associated with the electron-spin-to-rotation interaction. Note the shift of the mean frequencies of the (G_1', G_2') multiplets compared to the (G_1, G_2) states, resulting from the ν -dependence of the hamiltonian coefficients. Spin states are $(2F + 1)$ -fold degenerate in zero magnetic field (not shown). From ref. [43].

bottom and 5. Including the orientational degree of freedom, there are a total of $n_{\text{spin}} = (2s_e + 1)(2I_p + 1)(2I_d + 1)(2N + 1)$ states. In a finite magnetic field, they are all non-degenerate.

It is reasonable to add the four angular momenta in a sequence corresponding to decreasing interaction strength as exhibited in the hamiltonian (Figure 4

bottom). The main interaction is due to the electron–proton interaction $\mathcal{E}_4(\nu, N)\mathbf{I}_p \cdot \mathbf{s}_e$. It corresponds to the hyperfine interaction in the $1s$ state of the hydrogen atom, there leading to the well-known 1.4 GHz (wavelength 21 cm) hyperfine splitting between the states with total angular momentum $F = 0$ and $F = 1$. In HD^+ the interaction is weaker, $\mathcal{E}_4(\nu = 0, N) \simeq 0.92 \text{ GHz}$. Thus, one couples $\mathbf{I}_p + \mathbf{s}_e = \mathbf{G}_1$, with allowed quantum numbers $G_1 = 0, 1$.

Next in strength is the deuteron–electron interaction $\mathcal{E}_5(\nu, L)\mathbf{I}_d \cdot \mathbf{s}_e$ with $\mathcal{E}_5(\nu = 0, N) \simeq 0.14 \text{ GHz}$, corresponding to the hyperfine interaction in atomic deuterium. Note that $\mathcal{E}_4, \mathcal{E}_5$ are of order $\alpha^2 E_R(m_e/m_p)$. Hence, we further couple $\mathbf{I}_d + \mathbf{G}_1 = \mathbf{G}_2$, with allowed quantum numbers $G_2 = 1$ if $G_1 = 0$, otherwise $G_2 = 0, 1, 2$.

Then follows the electron spin–rotation interaction $\mathcal{E}_1(\nu, N)\mathbf{N} \cdot \mathbf{s}_e$, with $\mathcal{E}_1(\nu = 0, N) \simeq 0.03 \text{ GHz}$. Therefore, we couple $\mathbf{N} + \mathbf{G}_2 = \mathbf{F}$, and the quantum numbers follow as $F = \text{Max}(G_2 - N, N - G_2), \dots, N + G_2$. The number of allowed ‘pairings’ (G_1, G_2, F) for a given value of N corresponds to the number of spin states n_{spin} mentioned above.

The coefficients $\mathcal{E}_2, \mathcal{E}_3, \mathcal{E}_6, \mathcal{E}_7, \mathcal{E}_8, \mathcal{E}_9$ do not cause further splittings but slightly shift the already split states. As for \mathcal{E}_1 , they all are only relevant if the molecule is rotating, $N > 0$. \mathcal{E}_9 is proportional to the electric quadrupole moment Q_d of the deuteron. It has a very small value, e.g. $\mathcal{E}_9(\nu = 0, N = 1) \simeq 5.6 \text{ kHz}$. All coefficients are found in ref. [33] and subsequent works.

With the above sequence of angular momentum addition, the basis states are denoted by $|G_1, G_2, F\rangle$ and may be called ‘pure’ because they are eigenstates of $\mathbf{G}_1^2, \mathbf{G}_2^2, \mathbf{F}^2$. However, because of the couplings in the spin hamiltonian, $\mathbf{G}_1^2, \mathbf{G}_2^2$ do not commute with it and therefore the pure states are not eigenstates of the hamiltonian. Thus, G_1, G_2 are mostly not good quantum numbers, while F remains a good quantum number in absence of magnetic field. Then, $|G_1, G_2, F\rangle$ has $2F + 1$ – fold degeneracy.

Eigenstates p and their spin energies $E_{\text{spin}}(\nu, N, p)$ are found by diagonalising the effective hamiltonian $H_{\text{spin}}(\nu, N)$ in the introduced basis. The eigenstates are mostly (but not always) linear combinations of the pure states. For identification of an eigenstate p we can use the quantum numbers G_1, G_2, F of the particular pure state to which p would evolve if all interactions were reduced to very small strengths. The results of the diagonalisation for the two ‘simplest’ rotational levels $N = 0, 1$ are shown in Figure 5, together with the state labels p . The calculation of the spin structure is presented in the Supplemental Material.

The spin interactions, proportional to $\mathcal{E}_k(\nu, N)$, weaken with increasing distances between the particles. Since with increasing vibrational level ν the vibrational

wave function extends to larger internuclear separations R , the coefficients \mathcal{E}_k decrease markedly with ν . Also the rotation modifies the wave function of the molecule and therefore the coefficients \mathcal{E}_k are also N -dependent, albeit with a much weaker dependence than on ν . Summarising, the basic spin structure remains the same for all ν for a given N , and for all $N > 2$, given ν . But the detailed splittings between the spin states p vary with ν and N , even in zero magnetic field [33,34]. Figure 5 shows an example of the ν, N -dependence.

The spin structure theory can be extended to take into account the interaction of the magnetic moments with an external magnetic field, leading to the Zeeman effect [42]. The component of the total angular momentum \mathbf{F} along the magnetic field direction, $F_z = s_{e,z} + I_{p,z} + I_{d,z} + N_z$, is an observable with an associated good quantum number m_F . The calculation of the Zeeman effect is also outlined in the Supplemental Material.

(b) H_2^+

Being a homonuclear diatomic molecule containing fermionic nuclei, the total wave function of H_2^+

must be antisymmetric under exchange of the protons. The electronic wave function is symmetric, therefore the total nuclear wave function must be antisymmetric. It is a product of a nuclear-spin function and a rovibrational spatial wave function. In levels that have even $N = 0, 2, \dots$ (so-called para- H_2^+) the rovibrational wave function is even under exchange of the protons. Therefore, the nuclear spin wave function must be odd. This forces the two proton spins to couple to zero total nuclear spin angular momentum, $I = 0$. This leaves an uncoupled electron spin, leading to $G = 1/2$. \mathbf{G} couples with the rotational angular momentum \mathbf{N} to form the total angular momentum \mathbf{F} . As a consequence, the levels $(\nu, N = 0)$ have only one spin state, $|I = 0, G = 1/2, F = 1/2\rangle$. Levels $(\nu, N = 2, 4, \dots)$ have two spin states, $|I = 0, G = 1/2, F = N \pm 1/2\rangle$. This simplification compared to HD^+ is notable. We show the hyperfine structure of some rovibrational levels of H_2^+ in Figure 6.

The case of odd N implies instead a total nuclear spin $I = 1$ (ortho- H_2^+). The particular case $N = 1$, when there are 5 spin states, is also exemplified in Figure 6. For more details, see Supplemental Material.

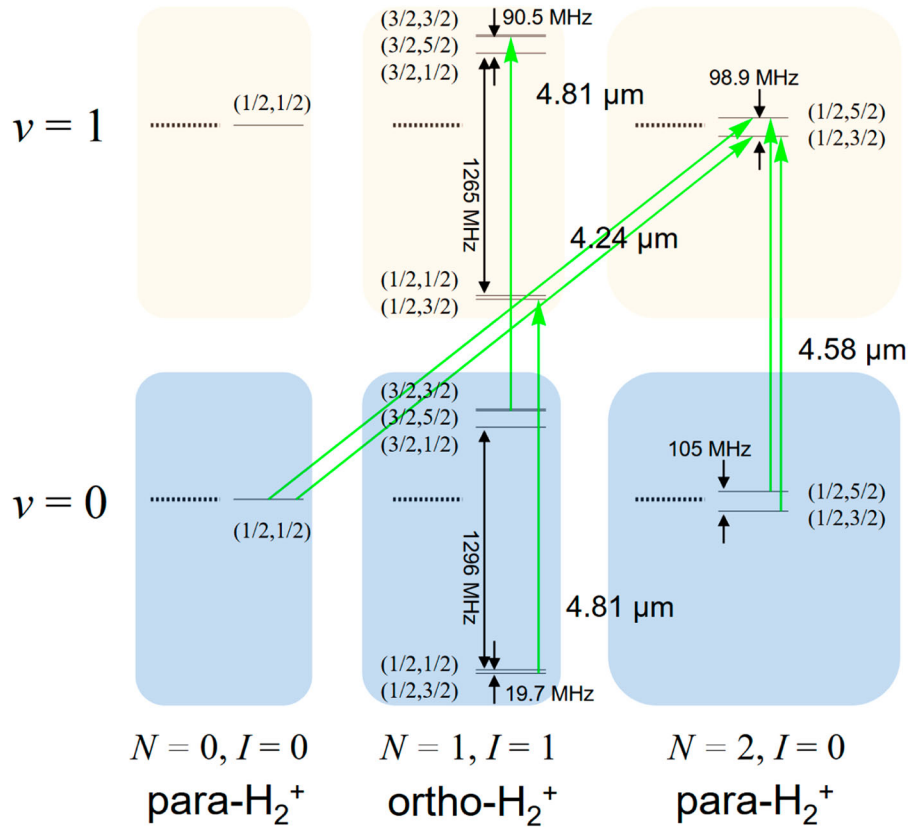


Figure 6. Hyperfine structure of H_2^+ for small ν, N . A spin state is denoted by the quantum numbers $p = (l, G, F)$. The values shown in parentheses are (G, F) , where G is the total particle spin and F is the total angular momentum of the molecule, including rotation. Green arrows: selected spin components of E2 transitions having particularly small systematic effects, suitable for frequency metrology. Their approximate wavelengths are indicated. From Ref. [48], corrected.

2.3.3. Accurate hyperfine theory: motivation and status

As mentioned, substantial effort has been devoted to developing a highly accurate theory of the hyperfine (spin) structure of the MHI. Why was this important?

First, many molecules exhibit hyperfine structure (NMR spectroscopy is based on it); therefore studying it at the finest level in the simplest molecule is an exploration of the foundations of this kind of physics.

Second, pushing the accuracy of the spin theory to the same level as existing or near-future data is a typical challenge in precision physics. Added complexity comes from the presence of up to four angular momenta in the MHI. Similar to the computation of the rovibrational energies, an accurate solution of the hyperfine structure problem must include QED contributions and must therefore start from the fundamental interactions (obtainable from NRQED) [44]. Then, tools for the computation of the actual hamiltonian coefficients need to be established.

Third, there is an opportunity to search for spin-dependent BSM interactions by comparing theoretical spin structure predictions with experimental data. Obviously, for maximum reach, the predictions should be as accurate as possible.

Fourth, accurate predictions of the spin frequencies can ease the experimenters' work load when they aim at determining spin-averaged transition frequencies $f_{\text{spin-avg}}^{(\text{exp})}$ from measured frequencies $f_{\text{line } i}^{(\text{exp})}$, which invariably include also corresponding spin frequencies $f_{\text{spin}, i}$. While a precise determination of the spin-averaged transition frequencies from experimental rovibrational spectroscopy data is in principle possible *without* knowledge about spin frequencies at all [26], or with only approximate knowledge, this requires measuring many spin components of the given rotational or rovibrational transition [45], or determining a suitable number of hyperfine splittings by radiofrequency spectroscopy. Since this is not always possible, accurate spin frequencies must be provided by theory. Therefore, on one hand researchers welcome accurate theoretical spin frequencies, for which accurate predictions of the coefficients \mathcal{E}_i are essential. On the other hand, whenever researchers measure more than just one spin component of a rovibrational transition the data can be used to confront the HFS theory, confirming or falsifying it.

(a) Spin theory of HD^+

Recently, $\mathcal{E}_4, \mathcal{E}_5$ have been computed for many rovibrational levels [46] with account of all contributions of fractional order α^2 , so that their fractional uncertainty is of order α^3 , specifically $u_{4,r} \simeq 9 \times 10^{-7}$ and

$u_{5,r} \simeq 6 \times 10^{-7}$. To achieve this level of theory uncertainty, elegant use has been made of the experimental data on the hyperfine structure of the hydrogen atom. The coefficients $\mathcal{E}_1, \mathcal{E}_6, \mathcal{E}_7$ have also recently been theoretically computed with reduced theory uncertainty of $u_{1,r} \simeq 3 \times 10^{-6}$, $u_{6,r}, u_{7,r} \simeq 2 \times 10^{-6}$ [38,46,47]. The remaining coefficients $\mathcal{E}_2, \mathcal{E}_3, \mathcal{E}_8, \mathcal{E}_9$ have been computed within the Breit–Pauli approximation, i.e. their fractional uncertainties are approximately equal to α^2 .

Current theoretical uncertainties of the spin frequencies of recently studied HD^+ rovibrational transitions are on the order of 0.1 kHz or less [47]. This is a consequence of (1) the high theoretical accuracies of the \mathcal{E} coefficients and (2) the correlations between the theoretical uncertainties of the \mathcal{E} coefficients for the upper (v', N') and the lower rovibrational level (v, N).

(b) Spin theory of H_2^+

The HFS theory formalism is the same for all MHI family members. For H_2^+ the hamiltonian coefficients have been computed to the similar accuracy as for HD^+ , and there is substantial decades-old experimental data to compare to, see Section 4.1.

2.3.4. The effect of finite nuclear size

Nuclei are not point particles but exhibit a spatial distribution of mass, charge, magnetisation, and other properties. The fact that the nuclear charge is smeared out leads to a 'nuclear volume shift' of the energy of an orbiting electron. This is a well-known effect in atomic physics and is a relevant effect in MHI precision spectroscopy as well. Because the electron's wavefunction is non-zero inside the nucleus, one must consider that there, the electrostatic interaction V_{nuc} between the electron and the extended distribution of nuclear charge differs from the point-charge-type Coulomb interaction $V_C(\mathbf{r}_e) \propto -Z_{\text{nuc}}e^2/r_e$ that is a sufficiently accurate description when the electron is outside. Here, \mathbf{r}_e is the electron's position operator relative to the centre of the nucleus *nuc*. The resulting energy shift may be calculated in first-order perturbation theory as $E_{\text{nuc}} = \int_{\text{nuc}} |\psi_{el}(\mathbf{r}_e)|^2 (V_{\text{nuc}}(\mathbf{r}_e) - V_C(\mathbf{r}_e)) d^3\mathbf{r}_e$, where the integration is over the nuclear volume. Since the nuclear diameter is so small ($\sim 10^{-5}a_0$) compared to the extent of the electron wavefunction ($\sim a_0$), the latter can be taken as constant over the nuclear volume, $\psi_{el}(\mathbf{r}_e) \approx \psi_{el}(\mathbf{r}_e = 0)$. Obtaining E_{nuc} then involves the evaluation of the volume integral over the nuclear electrostatic potential, which requires nuclear physics data or theory. In the approximation of a constant nuclear charge density ρ_{nuc} , $E_{\text{nuc}} =$

$2E_R(2\pi/3)Z_{\text{nuc}}(r_{\text{nuc}}^2/a_0^2)\langle\delta(\mathbf{r}_e)\rangle_{at.u.}$ [25]. The expression introduces the ‘nuclear charge radius’ $Z_{\text{nuc}}e r_{\text{nuc}}^2 = \int_{\text{nuc}} r^2 \rho_{\text{nuc}}(r) d^3\mathbf{r}$. For the proton and deuteron the values are $r_p = 0.8414(19) \times 10^{-15}\text{m}$ and $r_d = 2.12799(74) \times 10^{-15}\text{m}$. Also, $\langle\delta(\mathbf{r}_e)\rangle_{at.u.} = |\psi_{el}(\mathbf{r}_e = 0)|^2 a_0^3$ is the electron density in atomic units (dimensionless). Because $a_0 \propto \alpha^{-1}$, E_{nuc} is therefore of order $\alpha^2 E_R$ and in the framework of the separation Equation (2) is assigned to E_{rel} .

The molecular orbital figure for the $1s\sigma_g$ state (Figure 2) shows that there is substantial – actually, highest – electron density at the two nuclei, and so all rovibrational levels are affected by the nuclear volume shift. The density value is $\langle\delta(\mathbf{r}_e)\rangle_{at.u.} \approx 0.2$, which may be compared with $\langle\delta(\mathbf{r}_e)\rangle_{at.u.} = Z_{\text{nuc}}^2/(\pi n^3)$ for an s -electron of principal quantum number n in a hydrogen-like atom, in the approximation of infinite nuclear mass. The total E_{nuc} is the sum of the contributions from each nucleus. The densities at the two nuclei are exactly equal in the case of the homonuclear MHI, and are nearly equal, to sub-percent level, in the case of the non-symmetric HD^+ [25].

It is intuitively clear that the density $|\psi(\mathbf{r}_e = 0)|^2$ depends on the distance R between the two nuclei. Indeed, in the limiting case of large distance, the density at each nucleus would approach one-half the value for the hydrogen atom ($Z_{\text{nuc}} = 1$), because the wavefunction near each nucleus approaches the hydrogen wavefunction times $1/\sqrt{2}$. For very close nuclei, $R \rightarrow 0$, the density would take on the value for the helium ion ($Z_{\text{nuc}} = 2$), i.e. four times as large as in hydrogen. Now, in different vibrational states ν , the wavefunction of the nuclear oscillation is spread over a R -range increasing with ν , and also the mean internuclear distance $\langle R \rangle$ increases. Thus, with increasing ν the electron density at the nuclei decreases and so does the nuclear volume shift $E_{\text{nuc}}(\nu)$. The decrease can be accurately computed [25] and is approximately 2% for each subsequent ν level. For a given vibrational level, there is also a decrease with increasing rotational angular momentum N , because the mean value $\langle R \rangle$ increases due to centrifugal stretching. As this is a comparatively small effect, also the decrease of the nuclear shift is small, e.g. 0.1% in going from $N = 0$ to $N = 1$.

When we consider rotational and vibrational transitions, a nuclear shift effect on the frequencies occurs precisely because of said *variation* with ν , N . On one hand, the transition frequency shift is therefore substantially reduced compared to the level shift. On the other hand, a typical vibrational energy difference is also much smaller than the absolute energy of the level. These effects combine into a fractional shift $\simeq -2 \times 10^{-9}$ for a HD^+ vibrational transition frequency having moderate ν , ν'

Table 2. Main dependencies of HD^+ transition frequencies $f_{\text{line}} = f_{\text{spin-avg}} + f_{\text{spin}}$ on the fundamental constants.

Quantity	Contribution	Main dependencies	Relative magnitude
$f_{\text{spin-avg}}$	f_{nonrel}	$R_\infty, m_e/m_p, m_e/m_d$	1
	f_{rel}	α, r_p, r_d	2×10^{-5}
	f_{QED}	α	4×10^{-6}
f_{spin}		g_e, g_p, g_d, Q_d	$\begin{cases} \mathcal{O}(10^{-5}) \\ \text{(rot. transition)} \\ \mathcal{O}(10^{-7} - 10^{-8}) \\ \text{(vibr. transition)} \end{cases}$

Notes: Rightmost column: the indicated relative magnitude of f_{spin} holds for transitions between levels having moderate values of ν, N, ν', N' , and between spin states p, p' that have $G_1 = G'_1, G_2 = G'_2$ (favoured E1 transitions). Then, f_{spin} is of order 10 MHz or less.

(see also caption of Table 1), while for the fundamental rotational transition, the fractional shift is actually approximately twice as large.

Summarising, whereas the nuclear volume shift appears at first glance to be a minor effect, it is not, given today’s 10^{-12} -level experimental and theoretical accuracies. For comparison, in fractional terms the shift is comparable to that of the $1s - 2s$ transition in atomic hydrogen. Accounting for the nuclear volume shift in the MHI is essential for being able to contribute to the field of precision physics at state-of-the-art level. Moreover, the proton charge radius is of decided interest in the field of metrology of the fundamental constants (so-called ‘proton radius puzzle’ [1]).

2.3.5. An example of spin-averaged *ab initio* frequency

Table 1 presents an example of a theoretical spin-averaged frequency $f_{\text{spin-avg}}$, and its contributions, for a fourth overtone transition at 260 THz. Note that the size of the QED contribution is substantial, approximately -1 GHz, and its uncertainty is 2.1 kHz. These values should be compared with the current experimental uncertainty, approximately 1 kHz.

2.3.6. Transition frequencies and fundamental constants

It is useful to summarise the most relevant dependencies of the contributions to a transition frequency on the fundamental constants, see Table 2. The table does not show all dependencies, but only those that could, at least in principle, lead to a determination of the respective constant at an interesting level of accuracy.

To start with, all contributions are proportional to the Rydberg constant. However, because $f_{\text{rel}}, f_{\text{QED}}, f_{\text{spin}}$ are several orders smaller than f_{nonrel} , the current uncertainty of R_∞ , 1.9×10^{-12} [1] is irrelevant in comparison to the theoretical uncertainty of the three quantities. Therefore, only f_{nonrel} has a relevant dependence on R_∞ .

$f_{\text{rel}}, f_{\text{QED}}, f_{\text{spin}}$ are proportional to powers of the fine-structure constant α . But it is today known with uncertainty $\simeq 1.5 \times 10^{-10}$, which is so small that a determination of α from MHI is not realistic. We recall that α does not enter as a separate quantity into f_{nonrel} , but only in the combination with the electron mass, in R_∞ .

We come next to the mass ratios m_i/m_e ($i = p, d, t$ depending on the particular MHI), whose determination is one of the main opportunities of the precision physics of MHI. As shown in Section 2.2 the mass ratios appear at order unity in f_{nonrel} and therefore also in $f_{\text{spin-avg}}$. The sensitivities $\partial f_{\text{spin-avg}}(v, N \rightarrow v', N')/\partial(m_i/m_e)$ are required in order to extract the mass ratios from experimental data. The sensitivities follow from the sensitivities of the level energies, $\partial E_{\text{spin-avg}}(v, N)/\partial(m_i/m_e)$. Since $E_{\text{nonrel}}(v, N)$ is the dominant contribution to $E_{\text{spin-avg}}(v, N)$, it is sufficient to compute the former's sensitivities. Further, in this context, a good approximation to $E_{\text{nonrel}}(v, N)$ are the adiabatic energies $E(v, N)$ introduced above. Indeed, the so-called non-adiabatic corrections turn out to be only $\simeq 8 \times 10^{-5}$ fractionally for a fundamental vibrational transition frequency [52]. When expressed in units of E_R , the adiabatic level energies are the eigenvalues of a dimensionless Schrödinger equation for motion of a particle of dimensionless mass μ/m_e in one spatial dimension, as mentioned earlier. Thus, for a heteronuclear MHI, instead of separate sensitivities of $E_{\text{spin-avg}}/E_R$ to the two nuclear mass ratios (given in rows 18, 19 of Table 4), we are left, to a good approximation, with a single sensitivity to the reduced mass ratio μ/m_e alone [53]. Thus, the approximate calculation of the sensitivities $\partial(E(v, L)/E_R)/\partial(\mu/m_e)$ is easily done.

Finally, we have the nuclear volume contribution to the transition frequencies discussed in Section 2.3.4.

The above considerations can be expressed by giving the main dependencies of the spin-averaged transition frequencies in numerical form. As an example, consider $f_5 = f_{\text{spin-avg}}(0, 0 \rightarrow 5, 1)$,

$$\begin{aligned} f_5^{(\text{theor})}/\text{kHz} &= 259762971051.0(2.1)_{\text{QED}} + 0.50\Delta_r R_\infty \\ &\quad - 5.1\Delta_r \mu/m_e - 0.33\Delta_r r_p - 0.32\Delta_r r_d \\ &= 259762971051.0(2.1)_{\text{QED}}(5.1)_{\text{CODATA18}}. \end{aligned} \quad (5)$$

Here, the deviations of the fundamental constants from their current nominal (CODATA 2018 [1]) values are expressed in normalised form, $\Delta_r X = (X - X_{\text{CODATA18}})/u_{\text{CODATA18}}(X)$ where $u_{\text{CODATA18}}(X)$ is the absolute uncertainty of constant X . (The near-equality of the last two coefficients is due to the fact that the difference $r_d^2 - r_p^2$ has been measured very accurately with atomic hydrogen spectroscopy.)

Expression (5) indicates, via the absolute values of the numerical prefactors, how much the uncertainty of today's value of each fundamental constant contributes to the predicted transition frequency. For this, set $\Delta_r X = 1$. (For precise considerations, the correlations between the uncertainties $u_{\text{CODATA18}}(X)$ must be taken into account.) We recognise that it is the uncertainty of the mass ratio μ/m_e ($u_{r, \text{CODATA18}}(\mu/m_e) = 4.6 \times 10^{-11}$) that dominates the uncertainty of $f_5^{(\text{theor})}$.

We also recognise that for a deviation $\Delta_r X_i$ to become discernible in a comparison between experiment and prediction, a necessary condition is $|\Delta_r X_i| > u_{\text{QED}}(f_5^{(\text{theor})})/|\partial f_5^{(\text{theor})}/\partial \Delta_r X_i|$. This is also the lower bound (since experimental uncertainty is not included) for the reachable uncertainty in the determination of X_i via MHI spectroscopy. Given today's state-of-the-art $u_{\text{QED}}(f_5) = 2.1$ kHz, we realise that even in case of a negligible experimental accuracy the comparison of the measured transition frequency $f_5^{(\text{exp})}$ with its predicted value is not sensitive enough for allowing a competitive determination of either the nuclear charge radii, or the Rydberg constant. Since similar fractional theoretical uncertainties are achieved for other transitions between rovibrational levels having moderate rotational and vibrational quantum numbers, this inability also extends to any such transition, if considered individually. Unfortunately, the inability apparently also persists if a rather large set of accurate transition frequencies comprising both H_2^+ and HD^+ were to become available [54]. The only option at this time appears to be an accurate determination of the value of the normalised reduced mass μ/m_e .

We now turn to the spin frequencies f_{spin} . Although they directly depend on the g-factors of the electron, proton and deuteron, it will not be possible to determine these g-factors with accuracy competitive with direct measurements on the particles in Penning traps (e.g. for the proton, $u_r(g_p) \simeq 3 \times 10^{-10}$, currently). One issue is that the hamiltonian coefficients \mathcal{E}_i have uncertainties larger than 6×10^{-7} . A second issue is that one requires knowledge of the correction factors for the g-factors of the particles, arising because they are bound or shielded. The theory of bound-particle g-factors in MHI has so far only made the first steps [55,56], and to achieve vast improvements will be challenging, although not impossible, given the progress on hydrogenlike systems [2].

The spin frequencies also depend on higher moments of the nuclear structure, but it does not appear possible to extract them from MHI studies. In any case, those moments are also accessible via the hyperfine structure of atomic hydrogen and deuterium.

One dependence on nuclear properties that is potentially relevant for near-future precision studies is that on the electric quadrupole moment Q_d of the deuteron. The current uncertainty of this quantity (8×10^{-5} [57]) is comparable with or larger than the uncertainty of the *ab initio* spin theory of the corresponding energy contribution ($\simeq \alpha^2 = 5 \times 10^{-5}$). Further considerations are given in Sections 4.1 and 6.3.

2.4. Transitions

2.4.1. Excitation

We distinguish electric-dipole (E1), electric-quadrupole (E2), and two-photon (TP) transitions. Stimulated Raman transitions are a further possibility for, in particular, homonuclear MHI, but will not be discussed here.

In homonuclear diatomic molecules, the absence of a permanent dipole moment and the vanishing of electric-dipole transition matrix elements between rovibrational levels having moderate ν, ν' means that E1 transitions are forbidden, whereas E2 and TP transitions are allowed. Because of the fundamental importance of the H_2^+ molecule, its E2 transitions were discussed theoretically already in 1953 [58] – and to this day they have not been observed. Nevertheless, there is no doubt that they will become relevant in the near future. E2 transitions are possible also in heteronuclear diatomics; indeed, a E2 transition has recently been observed in HD^+ [59].

For heteronuclear MHI, the standard transition type used in experiments is E1. E2 transitions are useful for test purposes, and might become useful for exploring the HFS.

The three types of transitions obey selection rules and ‘strength rules’. There is a selection rule for the rotational angular momentum:

- E1 transitions: $N' - N = \pm 1$,
- E2 transitions: $N' - N = 0, \pm 2$, $N = 0 \rightarrow N' = 0$ is not allowed,
- TP transitions: $N' - N = 0, \pm 2$.

There is no strict selection rule for $\nu' - \nu$, but in general the transition rate will significantly decrease with increasing $|\nu' - \nu|$.

The theory for the transition rates, taking into account that the transitions occur between spin states, has been worked out for the different transition types for several MHI [40,42,60,61]. As an example, Figure 5 presents, for HD^+ , the so-called favoured spin components of a rovibrational transition, i.e. those E1 transitions having a large electric-dipole transition moment. For these, a ‘spin selection rule’ holds, requiring that the approximate

quantum numbers G_1, G_2 do not change, allowing only for changes of the total angular momentum, $F' - F = 0, \pm 1$. Figure 6 instead shows examples of (proposed) E2 transitions in the homonuclear H_2^+ .

2.4.2. Spontaneous decay

Spontaneous decay in heteronuclear MHI proceeds via E1 transitions. The rates for HD^+ for a set of transitions were computed in ref. [62] and a more extensive tabulation is found in ref. [63]. Two main features may be noted: the decay of a vibrationally excited upper state ν' proceeds dominantly via a reduction of the vibrational quantum number by one unit, $\Delta\nu = \nu' - \nu = +1$, and the lifetime is a few tens of milliseconds. This rather long lifetime is due to its scaling with the inverse square of the transition dipole moment and with the inverse cube of the transition frequency. The latter is comparatively small between neighbouring vibrational levels ($\simeq 60$ THz), and transition dipole moments for $\Delta\nu = 1$ are moderate, less than $0.1 \times e a_0$ [64]. The rate for spontaneous transitions with $\Delta\nu > 1$ is smaller than for $\Delta\nu = 1$ because the squared transition dipole moment decreases faster with $\Delta\nu$ than the cube of the transition frequency increases [64]. In $\nu = 0$, spontaneous decay occurs only via rotational transitions. Due to the even smaller transition frequencies, the decay rate between adjacent rotational levels in this manifold is much smaller than between vibrational levels, resulting in e.g. a long lifetime of 140 s for the level ($\nu = 0, N = 1$) against decay to $N = 0$.

In homonuclear ions, only E2 transitions can occur, and the lifetimes are days to weeks [65,66]. Amazingly, such extremely slow decays can actually be followed ‘in real time’: a single H_2^+ ion stored for weeks in a cryogenic vacuum in a Penning trap has been followed as it decayed step-wise from $\nu = 9$ to $\nu = 0$ within one month [67]. It should be noted that decay rates in the strong magnetic field of a Penning trap are somewhat modified compared to free space [68].

2.4.3. Black-body radiation-induced transitions

In heteronuclear MHI the black-body radiation (BBR) associated with the finite temperature T_{bb} of the vessel surrounding the MHI can induce E1 transitions from lower-energy to higher-energy levels [69,70]. Given the large energy separations between vibrational levels (e.g. $E(\nu' = 1, N' = 1) - E(\nu = 0, N = 0) \simeq k_B \times 2700$ K) compared to room-temperature thermal energy, this effect does not in practice induce vibrational excitation at a relevant rate, but only rotational excitation. Furthermore, it is only effective between rotational levels in the $\nu = 0$ manifold, since these have long natural lifetimes against spontaneous emission. Besides this absorption of BBR, also stimulated emission by BBR is possible,

a ‘downward’ process. The two types of processes are responsible for establishing thermal equilibrium between the rotational level population and the BBR heat bath.

As a result, in a heteronuclear MHI the thermal population of levels $\nu \geq 1$ is negligible. The fractional populations of levels ($\nu = 0, N$) are given by $P(N) = S(N) / \sum_{N=0}^{\infty} S(N)$, with $S(N) = (2N + 1) \exp(-\delta E_{\text{spin-avg}}(\nu = 0, N) / k_B T_{bb})$. Note the factor $(2N + 1)$ describing the degeneracy of a level of given rotational angular momentum. (The degeneracy of the particle spins does not appear in the formula because it is the same in all rotational levels and thus cancels). A reasonable approximation for the energy offset is $\delta E_{\text{spin-avg}}(\nu = 0, N) \simeq N(N + 1) h f_{\text{rot}} / 2$. This becomes exact in the absence of centrifugal stretching. The fundamental rotational frequency is given in Equation (1). Figure 9, right panel, indicates graphically by the green discs’ areas the relative populations $P(N)$ for HD^+ at $T_{bb} = 300$ K. Several rotational levels are substantially populated, and the largest population is $P(N = 2) \simeq 0.27$.

For homonuclear MHI, the expression for $P(N)$ differs, because the rotational wavefunction symmetry must be taken into account. Due to the absence of E1 transitions, a thermal equilibrium is not naturally present in a trapped homonuclear ensemble in ultra-high vacuum. One situation where thermal equilibrium might be reached is under collisions with a helium buffer gas [48].

3. Recent experimental studies

3.1. The experimental technique

3.1.1. Introduction

Given that spectroscopy of the MHI had been performed with various techniques over the course of several decades (see Sec. 1.3), in the mid-1990s it became clear to the author that a new approach was needed for progressing towards much higher accuracy. Sympathetic cooling of MHI by laser-cooled beryllium atomic ions in a linear radiofrequency (RF) ion trap was expected to provide a suitable environment for accurate spectroscopy of MHI, namely ultra-low ion temperature in the milli-kelvin range and spatial localisation. A line of research based on this idea was initiated by the author in the late 1990s [23,75]. The stated conditions promised a small Doppler width of the spectral lines and eventually spectroscopy in the Dicke regime, without time-of-flight broadening and with only a moderate second-order Doppler shift. If UHV conditions were achieved in the trap, also a nearly collision-free environment would be provided, virtually removing collision-induced broadening and frequency shifts, and allowing level lifetimes close to their natural values and thus narrowest spectroscopic linewidths. The

localisation would also simplify the determination of systematic shifts, for example due to any applied or residual magnetic field.

3.1.2. Trapping of ions

The linear ion trap, in combination with laser-cooling, is today a well-established tool for precision spectroscopy of atomic ions, including the realisation of quantum information processing. Textbooks treating the fundamentals of ion trapping are refs. [72–74]. The precision spectroscopy of molecular ions in ion traps is still not a widely employed technique, because of the complexity of preparing and controlling the molecular species in addition to the necessary atomic species.

Briefly, the linear ion trap consists of four, often cylindrical electrodes aligned parallel along the z axis, the so-called trap axis. A transverse two-dimensional (x, y), alternating electric field is established between them by a radio-frequency (RF) amplifier circuit, with a typical frequency of 15 MHz. When the amplitude of the electric field is suitably chosen, a charged particle can be trapped in transverse direction, meaning that it oscillates back and forth in the $x - y$ -plane. This motion can be described as occurring in an effective (time-averaged) potential, called secular potential, that is approximately parabolic, $V_{\text{sec}}(x, y) \propto x^2 + y^2$.

One also desires that the axial (z) motion of the ion remains bounded. This is accomplished by adding two sets of electrodes at positions $\pm z_e$ and applying an equal positive static voltage to them; this confines positively charged particles.

A linear ion trap is rather ‘spacey’; therefore it is possible to simultaneously confine many ions of equal charge sign in it. It is even possible to confine ions of different mass-to-charge ratio m/Q , although there are limits to the allowed disparity of their m/Q values. A trap can be loaded with ions by ionising gas phase neutral atoms or molecules that happen to be in the inner trap volume. Ionisation can occur via bombardment with electrons emitted towards that volume by an electron gun, or by laser photoionisation.

A crucial extension of the capability of ion trapping is laser cooling. Trapped atomic ions can be laser-cooled by a suitable laser. The process vastly reduces the kinetic energy of the atomic ions, and the residual kinetic energy is associated with random motion. Therefore one speaks about an ion temperature, T_{sec} .

It is feasible to simultaneously trap atomic ions that are directly laser-cooled and other (atomic or molecular) ions that are not laser-cooled. Although the interaction between the dissimilar ions is repulsive, the laser-cooled ions remove kinetic energy from the non-laser-cooled ions. This is called sympathetic cooling. The end result

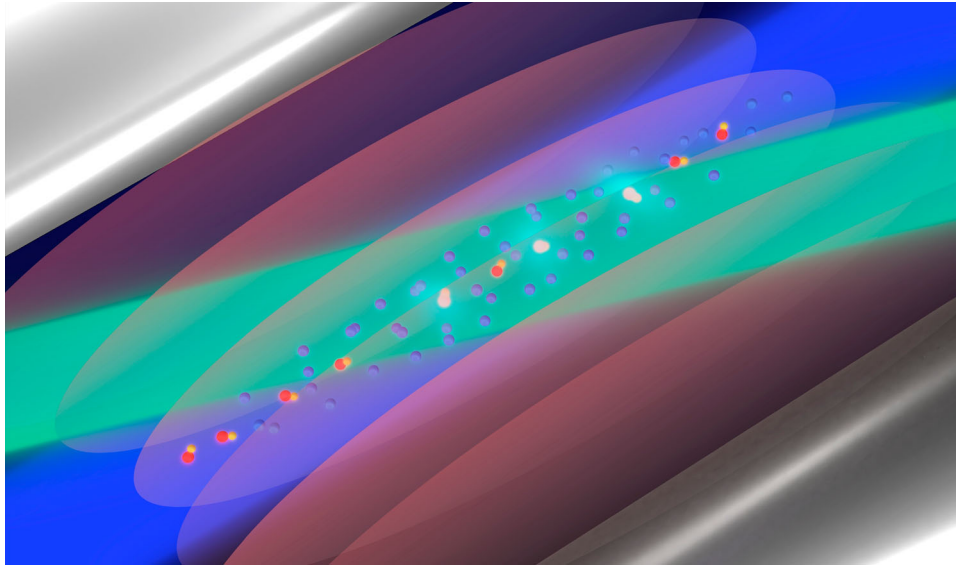


Figure 7. Spectroscopy of sympathetically cooled HD^+ ions: an artist's impression. The z axis runs from the lower left corner to the upper right corner of the image. Two of the four axial electrodes are shown in gray. The laser-cooled atomic ions are shown as blue balls, the sympathetically cooled MHI as yellow-red dumbbells. Blue is the cooling laser beam, green are the REMPD beams. The brown ellipses symbolise the spectroscopy radiation propagating along the transverse direction. Picture from S. Alighanbari, M. G. Hansen, S. Schiller.

is that the kinetic energy of all ions is reduced to a very large extent, especially if the non-laser-cooled ions have a larger charge-squared-to-mass ratio. An early review on sympathetic cooling of molecular ions is ref. [75].

Interestingly, when the field was nascent it had been stated in a theoretical study that sympathetic cooling of MHI in a linear RF trap would not be possible. For this reason, extensive numerical simulations were performed to verify this claim [76]; fortunately they pointed to the contrary. Finally, the experimental proof of the feasibility occurred in 2004 [24]. Figure 7 gives an artist's view of an ensemble of trapped and sympathetically cooled MHI undergoing spectroscopic excitation.

3.1.3. Mixed-species Coulomb clusters

An ensemble of cold beryllium ions (mass $m = 9u$) trapped in a RF trap arrange in an ellipsoid-shaped cluster if the axial (z) trapping potential is sufficiently weaker than the radial (x, y) trapping potential [77]. ‘Cold’ refers to the kinetic energy and this state is achieved by laser cooling the beryllium ions. If MHI are added to the beryllium ensemble, and if their number N_{MHI} is much smaller than the number of beryllium ions, they are efficiently cooled as well. The overall shape of the cold two-species cluster does not change substantially since the MHI arrange close to or on the trap axis z . The underlying reason for this arrangement is that the secular radial potential experienced by an ion, $V_{\text{sec}}(x, y) = m\omega_{\text{sec},m}^2(x^2 + y^2)/2$ scales approximately *inversely* with the mass m of the ion. Indeed, the radial secular oscillation frequency $\omega_{\text{sec},m} \propto Q/m$, approximately, for typical trap operating

parameters [78]. Thus, the total energy (secular potential energy plus inter-particle potential energy) of the two-species ensemble is minimised in static equilibrium (i.e. if the ions are cold) if the lighter MHI, instead of the heavier beryllium ions, arrange close to or on the z axis, where this secular potential is weak or zero. When the number of MHI is quite small, the ions arrange in a string on the z -axis. This string expands to a tube as the number increases, simply because there are ‘no vacancies left’ on the trap axis. These simple facts are easily found by performing molecular dynamics simulations of two-species clusters [24] or by simply calculating minimum-total-energy configurations of a mixed ion ensemble in their respective secular potentials (e.g. using *Mathematica*). Figure 8 shows an experimental CCD image of a Be^+/HD^+ Coulomb cluster and a computed image of a typical cluster. We point out an experimental study [79] of a two-*atomic*-species Coulomb cluster that beautifully imaged the arrangement of the lighter ions into a string surrounded by heavy ions, via laser-induced fluorescence of the lighter ions.

The particular interest of Be^+/MHI clusters in which the MHI arrange into a string is that this leads, ideally, not only to zero time-averaged radial coordinates, $\langle x_j \rangle = \langle y_j \rangle = 0$ for each ion j but also to small radial position spreads $\sqrt{\langle x_j^2 \rangle}, \sqrt{\langle y_j^2 \rangle}$. The spreads are approximately equal and will be denoted by x_{rms} . They are the consequence of the residual thermal (Brownian) motion of the MHIs, under the influence of all forces. This motion remains present even under sympathetic cooling, since the laser cooling is not able to cool the atomic

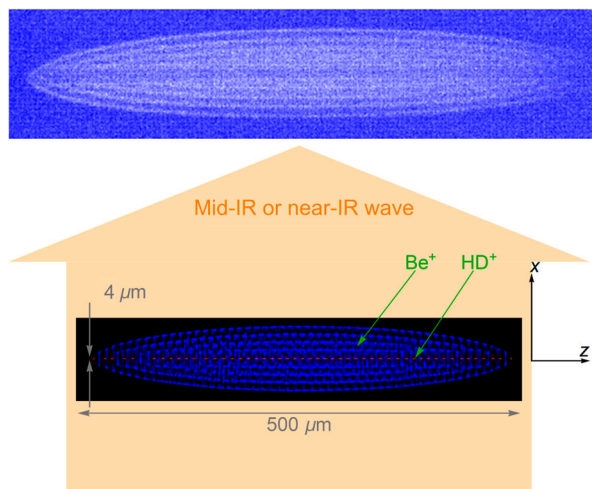


Figure 8. Top: CCD image of the 313 nm Be^+ ion fluorescence of a two-species Coulomb cluster. The darker horizontal line contains sympathetically cooled HD^+ ions. Bottom: A cluster simulated by molecular dynamics calculation. The propagation direction of a spectroscopy wave used for one-photon spectroscopy is superposed. The simulation was performed for 2000 Be^+ ions, 50 HD^+ ions, $T_{\text{sec}} = 10$ mK. The indicated HD^+ x coordinate range ($4 \mu\text{m}$) is approximate. Data from S. Alighanbari *et al.*

ions to absolute zero temperature, but only to the so-called Doppler limit. Thus, their residual motion affects also the MHI via the Coulomb interaction. Additional heating effects may occur, but this issue and the topic of micromotion are beyond the scope of this introduction.

If we assume that the MHI transverse motion is mostly influenced by the secular potential, then we can invoke the equipartition law to relate one ‘unit’ of secular thermal energy to the r.m.s. secular potential energy of one transverse degree of freedom, $k_B T_{\text{sec}}/2 = \langle V_{\text{sec}}(x) \rangle = m_{\text{MHI}} \omega_{\text{sec,MHI}}^2 x_{\text{rms}}^2/2$. Numerically, for a secular temperature $T_{\text{sec}} \simeq 1$ mK (a value moderately larger than the Doppler cooling limit for Be^+), $x_{\text{rms}} \simeq 0.3 \mu\text{m}$ if the secular frequency $\omega_{\text{sec,HD}^+} \simeq 2\pi \times 0.8$ MHz, typical for a macroscopic RF trap.

3.1.4. Spectroscopy

All rotational and vibrational MHI spectroscopy experiments to date [11,14,80–82] have used techniques in which the MHI was destroyed after its excitation. Figure 9 (left) shows one recent spectroscopy scenario applied to trapped MHI. Both spectroscopy radiation and additional optical radiation for achieving photodissociation from the excited state are applied. Molecules remaining in the lower spectroscopy state are not or not substantially affected by the photodissociation field. This is a simple example of ‘resonance enhanced multi-photon dissociation (REMPD)’. The products of a dissociated MHI (in case of HD^+ , a neutral D atom and a proton) do not

remain trapped, since the ion trap field does not support a stable confinement of the light proton. Thus, the spectroscopic excitation of a MHI results in its removal from the trap. Figure 10 shows a timing diagram of the relevant processes. A refinement consists in applying the two radiation fields in alternating manner, in order to avoid the light shifts that the photodissociation field may induce on the spectroscopy states. This is possible thanks to the metastability of the upper spectroscopy state (Section 2.4.2).

The MHI loss can be detected by the technique of secular excitation as follows. The radial secular oscillation of the trapped MHI, at frequency $\omega_{\text{sec,MHI}}$, can be resonantly excited by applying a small a.c. voltage having the same frequency to an electrode close to the trap. Via Coulomb ion-ion interactions, the MHIs’ oscillations pump energy also into the beryllium ion ensemble, that consequently heats up. This leads to a detectable change in its fluorescence, as follows. The beryllium ions are usually continuously irradiated by the cooling laser that is kept at a fixed negative detuning from atomic resonance, so as to effect the laser cooling. Any induced increase in beryllium temperature leads to spectral broadening of the atomic transition line due to an increased thermal Doppler effect. This causes a change of absorption from the cooling laser and consequently of fluorescence rate. The change is approximately proportional to the number of MHI and the secular excitation voltage amplitude. Finally, the molecules’ spectroscopic signal is the difference between the Be^+ fluorescence level recorded during a secular excitation before and after the application of the spectroscopy and REMPD waves (dashed horizontal lines in Figure 10), normalised to the first level. The figure presents one single spectroscopy cycle, generating a single data point, said fractional difference of beryllium fluorescence level. The spectroscopy cycle must be repeated many times for a given frequency of the spectroscopy wave. The mean value of the acquired data set represents the strength of the spectroscopic excitation at that frequency. To obtain the full lineshape of a spectroscopic transition line, the procedure is repeated for a (typically small) set of frequencies. Because the experiments are performed with small MHI ensembles, new ensembles must be loaded after typically every five cycles. This leads to long experiment durations for acquiring even a single line.

3.1.5. Rotational cooling

Optionally, a rotational cooling phase precedes the spectroscopy, in particular if the level ($v = 0, N = 0$) of a heteronuclear MHI is selected to be the lower level for spectroscopic excitation. In thermal equilibrium, only a fraction $P(N = 0) \simeq 0.10$ of HD^+ ions are in this level

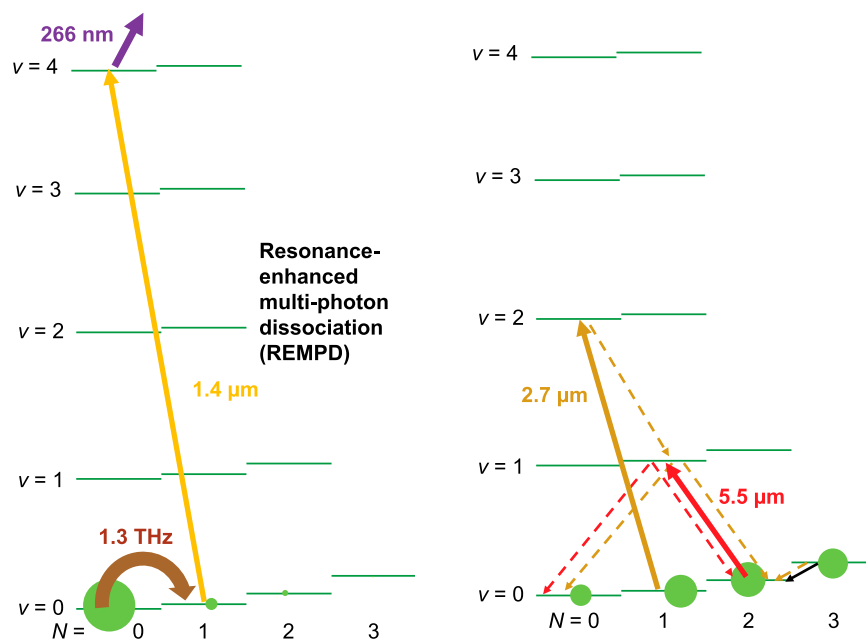


Figure 9. Left: Rotational spectroscopy by REMPDP. The green disk areas represent the populations after rotational cooling and before subsequent REMPDP. The thick brown arrow is the spectroscopy radiation. Right: Rotational laser cooling phase optionally preceding the spectroscopy phase. Full arrows are laser-driven transitions. The dashed light brown arrows indicate relevant spontaneous emission processes. The black line is a BBR-driven emission process. Green disk areas represent the fractional populations in thermal equilibrium at 300 K.

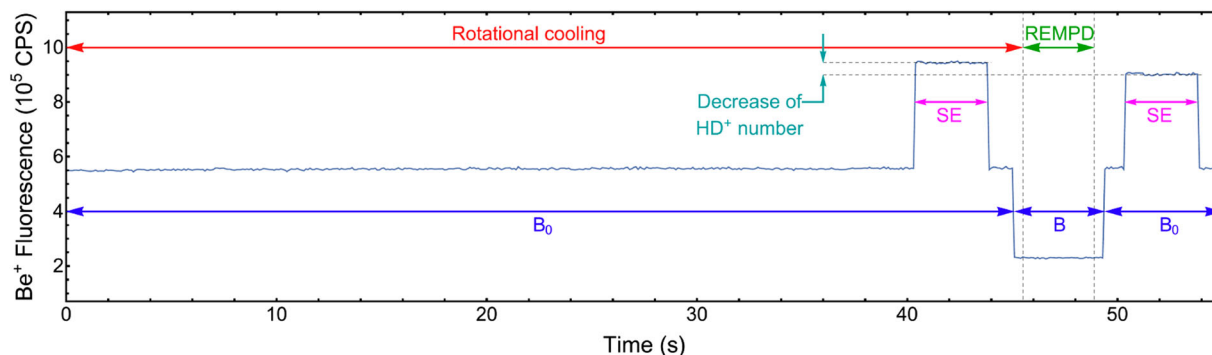


Figure 10. Timing diagram and data of one cycle of state preparation and spectroscopy. Beryllium laser cooling is on all the time. Rotational cooling (red) is performed first. Green, 'REMPD': rotational spectroscopy phase, i.e. the spectroscopy wave and the REMPDP lasers are turned on. Magenta, SE: secular excitation of the MHI is turned on (simultaneously or alternately). Grey: the fluorescence rate of the laser-cooled beryllium ions. Cyan and dotted horizontal lines: the change of fluorescence rate after application of REMPDP; it is proportional to the number of dissociated MHI. 'B': a magnetic flux strength B is applied during REMPDP. 'B₀': a different strength B_0 is applied during rotational laser cooling. CPS: counts per second. From ref. [45].

(Section 2.4.3). Laser rotational cooling [70] is able to increase substantially this fraction, by transferring population residing in levels ($v = 0, N > 0$) to the level ($v = 0, N = 0$). The principle is presented in Figure 9, right panel. Two mid-infrared laser waves excite those MHI that happen to be in level ($v = 0, N = 1$) or ($v = 0, N = 2$). Spontaneous emission from the respective excited levels (2, 0) or (1, 1) leads to partial decay into the ground rovibrational level (0, 0) according to corresponding branching ratios. If decay occurs into other levels, further laser excitation will take place until the MHI end

up in (0, 0). In practice, in steady-state, some 60–75% of the MHI are transferred into the goal level (0, 0). Although this is not perfect, the substantial increase in population has allowed the precision measurements of refs. [43,45,51].

Accurate vibrational spectroscopy has also been achieved without laser rotational cooling [82]. In order to obtain sufficiently large signals, the lower spectroscopy level was chosen to be ($v = 0, N = 3$), whose thermal occupation probability $P(N = 3)$ is maximum in thermal equilibrium.

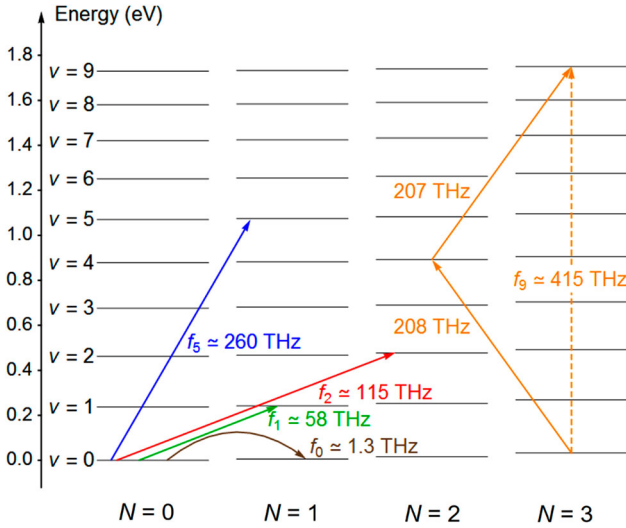


Figure 11. Overview of transitions measured with high accuracy (f_0, f_1, f_5, f_9) or high resolution (f_2 [59]).

3.2. Results

3.2.1. Observation of ultranarrow transitions

Figure 11 shows the MHI rotational and vibrational transitions measured to date with accuracy better than 1 part in 10^9 . These measurements were all done on spectral lines whose Doppler broadening was suppressed. Therefore, the experiments could resolve individual spin components $(v, N, p) \rightarrow (v', N', p')$. The absence of Doppler broadening was a result of either the employed spectroscopic technique (two-photon spectroscopy), or of particularly good spatial confinement of the MHI.

Confinement can lead to linewidth narrowing via the Dicke effect. The simplest model of this effect considers an atom moving between two walls separated by a distance a . When $a < \lambda/\pi$ the probability of emission with the recoil momentum being given to the walls becomes substantial, i.e. the emission spectrum consists mostly of a sharp line with a weak Doppler-broadened background. The recoil-free probability steadily decreases with increasing a , nevertheless a sharp line still occurs even if $a \simeq 3\lambda/2$.

In Section 3.1.3 we discussed the radial range x_{rms} of the MHI confined near the axis of the trap. We may make the approximate correspondence $a \simeq 2x_{\text{rms}}$, implying that the regime of dominant recoil-free emission is $\lambda > 2\pi x_{\text{rms}}$ for one-photon transitions. In absorption, which is relevant for MHI spectroscopy, the same condition holds. An alternative description of the condition for the Dicke effect is $\langle \exp(i\mathbf{k} \cdot \mathbf{r}_j(t)) \rangle \lesssim \mathcal{O}(1)$, where $\mathbf{r}_j(t)$ is the position of MHI j , and $\langle \dots \rangle$ is the time average, and \mathbf{k} is the wavevector of the spectroscopy radiation.

According to molecular dynamics simulations, the radial confinement in a string of MHI is $x_{\text{rms}} \simeq 0.3 \mu\text{m}$

when $T_{\text{sec}} \simeq 1 \text{ mK}$, increasing to $x_{\text{rms}} \simeq 1.7 \mu\text{m}$ when $T_{\text{sec}} \simeq 12 \text{ mK}$. For the tube configuration, the value at this temperature is substantially larger, $x_{\text{rms}} \simeq 8.4 \mu\text{m}$ [83]. These levels of confinement can be taken advantage of by directing the spectroscopy radiation at right angle to the trap axis.

Thus, for spectroscopy of the fundamental rotational transition ($f_0 \simeq 1.3 \text{ THz}$, $\lambda \simeq 230 \mu\text{m}$) the wavelength is larger than $2\pi x_{\text{rms}}$ even with the MHI at 12 mK and arranged in a tube. In case of the fundamental vibrational transition ($v = 0 \rightarrow v' = 1$, $\lambda = 5.1 \mu\text{m}$) the Dicke condition is satisfied if the ions are at 1 mK and in a string configuration [43]. High overtone transitions have spectroscopy wavelengths so short (e.g. f_5 with $1.1 \mu\text{m}$) that the the Dicke condition is not satisfied any more.

The situation is different for experiments employing two-photon spectroscopy with counter-propagating beams of (nearly) equal frequency. The net momentum associated with simultaneous absorption of one photon from each beam is (nearly) zero. Past studies unrelated to MHI have demonstrated that a narrow Doppler-free line occurs in two-photon spectroscopy with equal-frequency beams even in a low-density gas, where the particle motion is unrestricted. In the two-photon spectroscopy of the $(0, 3) \rightarrow (9, 3)$ transition of trapped cold HD^+ (f_9 [82]) two counter-propagating waves with dissimilar wavelengths 1442.4 nm, 1445.3 nm were employed. This was required in order to obtain a near-resonance with an intermediate level, $(4, 2)$. The effective two-photon wave vector $\mathbf{k}_1 - \mathbf{k}_2$, with $|\mathbf{k}_1 - \mathbf{k}_2|^{-1} \simeq 9 \times 10^{-3} / \mu\text{m}$, is so small that the condition for occurrence of a Dicke-narrowed line, $\langle \exp(i(\mathbf{k}_1 - \mathbf{k}_2) \cdot \mathbf{r}_j(t)) \rangle \lesssim \mathcal{O}(1)$, is satisfied even if the ions are contained in a tube of relatively large radius, $\simeq 50 \mu\text{m}$, instead of in a string.

3.2.2. Status of experiments

The importance of a particular spectroscopy experiment depends on the achieved level of control or determination of the systematic shifts. This level can be the better, the higher the achieved line resolution. One fundamental contribution to the line resolution is the spectral linewidth of the employed spectroscopy radiation source. In rotational spectroscopy, use has been made of a THz source that is implemented as an upconverter of a microwave. When referenced to a hydrogen maser, such a THz source exhibits a linewidth at the sub-Hz level, as measurements have shown [83,84], and its frequency instability is smaller than this level. The sub-Hz level is much smaller than the current theory uncertainty of both the spin frequencies (20–120 Hz, Table 3) and the QED contributions (19 Hz, Table 4), and therefore such a source is a powerful spectroscopy tool to measure the hyperfine structure precisely. While it has been

used only on HD^+ , it could in the future equally well be used on HT^+ or DT^+ . The narrowest line (in absolute terms) observed to date is indeed a spin component of the HD^+ rotational transition, having approximately 4 Hz linewidth [45].

In the rotational transition study [45], typical spectroscopic linewidths were approximately 20 Hz. With such linewidths and the need to determine the substantial systematic shifts, the uncertainties of the transition frequencies of various spin components resulted being $(1.3 - 5) \times 10^{-11}$. These are approximately one order less accurate than vibrational results and thus individually moderately competitive for most applications of MHI. However, the absolute uncertainties, 17–64 Hz,

were small enough to yield upper-state hyperfine splittings $E_{\text{spin}}(v', N', p) - E_{\text{spin}}(v', N', p')$ and combinations of spin frequencies ($\Delta f_{\text{spin},i,j} = f_{\text{spin},i} - f_{\text{spin},j}$) having substantially better accuracy than what has been obtained so far from vibrational spectroscopy. Therefore the rotational data can be used to test the spin structure theory and in this respect, rotational spectroscopy is a useful addition to RF spectroscopy.

Turning to vibrational transitions, we point out their advantage that several of the systematic shifts enumerated in the next subsection are only weakly dependent on the vibrational quantum number and therefore become smaller in fractional terms with increasing vibrational transition frequency. The fractional contribution is

Table 3. Comparison between the HD^+ hyperfine structure theory prediction and data from high-accuracy rotational and vibrational transition frequency measurements. In the analyses leading to the shown numbers, no fits of HFS hamiltonian coefficients were performed.

transition $(v, N) \rightarrow (v', N')$	n	exp.–theory (kHz)	u_{exp} (kHz)	u_{theor} (kHz)	$\partial \Delta f_{\text{spin}} / \partial Q_d$
$f_0: (0, 0) \rightarrow (0, 1)$	6	−0.95 to + 0.30	0.04 to 0.09 [45]	0.02 to 0.12	27 kHz/ Q_d (*)
$f_1: (0, 0) \rightarrow (1, 1)$	2	0.39	0.32 [43]	0.12	14 kHz/ Q_d
$f_5: (0, 0) \rightarrow (5, 1)$	2	0.6	1.2 [51]	0.1	12 kHz/ Q_d
$f_9: (0, 3) \rightarrow (9, 3)$	2	8.4	0.9 [85]	0.3	0.004 kHz/ Q_d

Notes: Columns 3 to 6 refer to spin frequency differences $\Delta f_{\text{spin},i,j} = f_{\text{spin},i} - f_{\text{spin},j}$. n is the number of measured spin components. The values in columns 3, 5 are from ref. [47]. The values in the last column are obtained from the sensitivities $\gamma'_{i,9} = \partial f_{\text{spin},i}^{(\text{theor})} / \partial \mathcal{E}'_9$ and, if $N \neq 0$, $\gamma_{i,9} = \partial f_{\text{spin},i}^{(\text{theor})} / \partial \mathcal{E}_9$ reported in the listed references or computed here, using the values of $\mathcal{E}_9(v, N)$ from ref. [33] and [49]. (*) This value refers to a spin frequency difference ($i = 20, j = 12$) for which $u_{\text{exp}} = 0.072$ kHz, $u_{\text{theor}} = 0.064$ kHz, exp.–theory = −0.95 kHz. See text for a discussion.

Table 4. Transitions of the HD^+ molecule that have been measured and calculated with high accuracy [43,45,51,85]. In the analysis leading to the rotational transition frequency f_0 two HFS hamiltonian coefficients were fitted.

Transition Reference	(0, 0 \rightarrow (5, 1) Alighanbari et al. (2020, 2023)	(0, 0) \rightarrow (0, 1) Alighanbari et al. (2020, 2023)	(0, 0) \rightarrow (1, 1) Kortunov et al. (2021)	(0, 3) \rightarrow (9, 3) Germann et al. (2021)*	row
Experiment	f_5	f_0	f_1	f_9	1
Frequency (kHz)	259762971051.24	1314925753.000	58605052164.19	415264925501.43	2
exp.unc.(frac., abs.)	$2.3 \times 10^{-12}, 0.60$ kHz	$1.2 \times 10^{-11}, 0.015$ kHz	$2.6 \times 10^{-12}, 0.15$ kHz	$1.1 \times 10^{-12}, 0.46$ kHz	3
Theory	f_5	f_0	f_1	f_9	4
Frequency (kHz)	259762971050.97	1314925752.932	58605052163.92	415264925502.84	5
Spin theory unc.(frac., abs.)	$1.4 \times 10^{-13}, 0.036$ kHz	$2 \times 10^{-12}, 0.002$ kHz	$4.1 \times 10^{-13}, 0.024$ kHz	$1.9 \times 10^{-13}, 0.081$ kHz	6
QED theory unc.(frac., abs.)	$8.1 \times 10^{-12}, 2.1$ kHz	$1.4 \times 10^{-11}, 0.019$ kHz	$8.5 \times 10^{-12}, 0.50$ kHz	$7.9 \times 10^{-12}, 3.3$ kHz	7
CODATA 2018 unc.(frac., abs.)	$1.9 \times 10^{-11}, 5.1$ kHz	$4.6 \times 10^{-11}, 0.061$ kHz	$2.2 \times 10^{-11}, 1.3$ kHz	$1.6 \times 10^{-11}, 6.6$ kHz	8
Experiment – theory (kHz)	0.27(5.5) _{tot}	0.069(0.066) _{tot}	0.27(1.4) _{tot}	−1.4(7.4) _{tot}	9
frac. tot. unc.	2.1×10^{-11}	5.0×10^{-11}	2.4×10^{-11}	1.8×10^{-11}	10
theor. frac. contrib. from:					
nuclear radii	-2.1×10^{-9}	-3.6×10^{-9}	-2.2×10^{-9}	-2.0×10^{-9}	11
$O(\alpha^2)$ incl. nucl. radii	1.5×10^{-5}	3.7×10^{-5}	1.7×10^{-5}	1.4×10^{-5}	12
$O(\alpha^3)$	-4.1×10^{-6}	-7.1×10^{-6}	-4.3×10^{-6}	-4.0×10^{-6}	13
$O(\alpha^4)$	-2.9×10^{-8}	-5.0×10^{-8}	-3.0×10^{-8}	-2.8×10^{-8}	14
$O(\alpha^5)$	1.8×10^{-9}	3.0×10^{-9}	1.9×10^{-9}	1.8×10^{-9}	15
$O(\alpha^6)$	-1.3×10^{-11}	-1.2×10^{-11}	-1.3×10^{-11}	-1.3×10^{-11}	16
Other	$4. \times 10^{-12}$	$7. \times 10^{-12}$	$4. \times 10^{-12}$	$4. \times 10^{-12}$	17
$d(\ln f / d(\ln(m_p/m_e)))$	-2.82×10^{-1}	-6.58×10^{-1}	-3.23×10^{-1}	-2.35×10^{-1}	18
$d(\ln f / d(\ln(m_d/m_e)))$	-1.41×10^{-1}	-3.29×10^{-1}	-1.62×10^{-1}	-1.17×10^{-1}	19
	$\mu/m_e = m_p m_d / m_e (m_p + m_d)$				
HD^+ spectroscopy	1223.899228720(25)	1223.899228658(23)	1223.899228711(22)	1223.899228735(28)	20
CODATA 2018		1223.899228723(56)			21
Penning Traps		1223.899228642(37)			22

Notes: In rows 11 to 19 we present the fractional contributions to the transition frequencies, as computed *ab initio*, as well as the fractional sensitivities of the frequencies to the mass ratios. In the bottom section of the table the values of the normalised reduced nuclear mass are given, respectively determined from the individual HD^+ transition frequencies, reported by the CODATA 2018 committee, and from Penning trap measurements. The latter is computed using the CODATA 2018 value for m_e/u (that relies mostly on ref. [92]), m_d/u [93], and m_d/m_p [67]. * Reanalyzed in ref. [51].

approximately two orders smaller than for the rotational transition. Taking advantage of these facts is of crucial importance for most applications of MHI. The Zeeman shift is a particularly important example in this respect.

However, the linewidths of the optical radiation delivered to MHI in vibrational spectroscopy have, until to date, been substantially larger in absolute terms than in the case of rotational spectroscopy. One reason is the complexity of production and transport of ultranarrow-linewidth optical radiation from the source – invariably some laser stabilised to an ultrastable optical cavity – to the ion trap. Another reason is that the spectroscopy wave intensity may have to be set so as to obtain sufficiently strong signals and this may also cause undesired power (saturation) broadening of the transition. Among published results, the vibrational transition with the highest observed line resolution showed a linewidth of approximately 400 Hz, at a frequency $f_5 \simeq 260$ THz [51]. It is a notable result that the corresponding line resolution is equal to the best value observed so far in rotational spectroscopy. After correction for the systematic shifts, the accuracies of the spin component transition frequencies of the f_5 transition were $\simeq 0.8$ kHz (3.3×10^{-12}). The spin components of the two-photon transition f_9 have the highest fractional accuracy achieved experimentally to date, $\simeq 1.5 \times 10^{-12}$ ($\simeq 0.6$ kHz) [85]. These values (and the quality of spin theory) imply that spin-averaged frequencies can be derived with excellent fractional uncertainties. However, the combinations of spin frequencies, $\Delta f_{\text{spin},i,j}$, obtained from these vibrational transitions carry $\simeq 1$ kHz experimental uncertainty, much larger than obtained with the rotational transition, and are thus less useful for testing HFS precisely.

3.2.3. Systematic shifts

As in atomic ion spectroscopy, a sizable number of systematic shifts are encountered in precision MHI spectroscopy. The reasons for their presence range from fundamental to technical. The following must be taken into account:

- (1) The Zeeman effect, present because a magnetic field is applied in the trapping region for laser cooling of the beryllium ions, or because the environmental field has not been fully compensated.
- (2) A light shift (a.c. Stark shift) caused by the laser light required for beryllium ion laser cooling, if it is kept on during MHI spectroscopy. In current experiments using ion clusters, it is not possible, in terms of spatial overlap, to avoid the cooling laser wave irradiating the MHI. However, the power of this cooling light (313 nm) is low (tens of μW), so the light shift is small.

- (3) Light shifts caused by the laser wave(s) involved in the REMPD process, in particular the photodissociation wave, unless they are turned off during MHI excitation. These light shifts, and the previous one, are proportional to the corresponding frequency-dependent molecular polarisability.
- (4) The spectroscopy wave has a finite intensity and also potentially causes a light shift.
- (5) The vacuum chamber hosting the ion trap is typically at room temperature. Thus, a BBR-induced light shift occurs.
- (6) The MHI are subjected to a trap-related electric field gradient that couples to the molecular electric quadrupole moment and produces shifts.
- (7) The absorption of the photon may cause the MHI to recoil. The corresponding kinetic energy must be provided by the photon. As a consequence, the resonance would be shifted to higher frequency, by an amount $\Delta f_{\text{rec}} = hf^2/2m_{\text{MHI}}c^2$.
- (8) An important shift is caused by the trap RF electric field [45]. The shift has been found to increase with the square of the RF drive voltage amplitude, which indicates that it may be due to the a.c. Stark shift and/or the a.c. Zeeman shift. The a.c. Stark shift is proportional to the squared electric field and to the a.c. polarisability of the molecule, and occurs both in homo- and heteronuclear MHI. The polarisability values are species- and state-dependent [86]. A non-zero time-averaged squared electric field may occur if the MHI is not confined to a node of the RF field, and this can result from the finite temperature, spurious d.c. potentials, electrical noise and ion-ion interactions. An a.c. Zeeman shift would be caused by the a.c. currents flowing in and out of the trap electrodes, producing an a.c. magnetic field at the frequency of the RF drive. If an MHI experiences a non-zero mean electric field, an additional shift may occur, the d.c. Stark shift, proportional to the d.c. polarisability of the MHI.

The molecular sensitivities to some of these shifts can be computed *ab initio*, e.g. the Zeeman shift [42], the electric quadrupole shift [87], the BBR shift, and spin-state dependent a.c. Stark (light) shift [86] (see also [45,51]). Together with a measurement or estimate of the relevant perturbing field (e.g. laser intensity), the corresponding shift can then be estimated.

In practice, it is desirable to determine the shifts, or the absence thereof, experimentally, whenever possible. For this, one repeats the measurement of transition frequency under different conditions: different values of the

applied magnetic field, the cooling laser intensity, the spectroscopy laser intensity, and the dissociation laser intensity. As mentioned earlier, it is possible to irradiate the REMPD laser(s) and the spectroscopy laser alternately for a desired total duration. Then, the spectroscopic transition is not influenced by the REMPD laser(s). The temperature of the BBR is not easily changed substantially, therefore one relies on the theoretical calculation. It predicts the shift to be negligible. The trap-drive-related shifts may be characterised by repeating the measurements (i) for different RF amplitudes, (ii) at non-nominal trap operating conditions. The latter is implemented by applying substantial d.c. voltages to some trap electrodes, causing a substantial (visible) displacement of the atomic ion subensemble in transverse direction.

The presence or absence of a recoil shift cannot be ascertained easily, unless it would be possible to study the same transition under two fundamentally different conditions, e.g. under one-photon and under two-photon excitation, or in a cluster and on an isolated single ion. For a rotational transition, Δf_{rec} is of 1-hertz level and negligible, if at all present. For a high overtone transition, for example f_5 , if present, the recoil shift would be so large ($\simeq 50$ kHz) as to be well beyond any theoretical, CODATA 2018, or experimental uncertainty (after correcting for the other systematic shifts described here). Its presence or absence could then be determined with a high degree of confidence. This has indeed been done. More challenging is the case of the fundamental vibrational transition, where a hypothetical recoil shift (2.5 kHz) is comparable to the total uncertainty arising from theory, CODATA, and experiment. The current understanding of recoil shift effects is reported in [51].

Finally, a rather important shift, wholly unrelated to the experiment proper, may arise if the frequency standard that serves as reference for synthesisers and frequency counters has a systematic error. This error can only be identified by comparing the standard, at least occasionally, to a different, trustable standard. In the work of refs. [43,45,51] a hydrogen maser was used as the frequency standard. Since these instruments can exhibit substantial, but stable systematic frequency offsets at 1×10^{-11} level, they need to be calibrated. One option to do so is with the help of a GNSS receiver that provides a 1-pulse-per-second signal derived from the atomic time scale.

As an example of experimental efforts on the topic of the systematic shifts, we may contrast two studies: in the study of the rotational transition ($f_0 \simeq 1.3$ THz) several shifts were clearly observed thanks to the high spectral resolution, and found to be important. For the

overtone transition ($f_5 \simeq 259$ THz) systematic shifts were barely detected: on one hand because the shifts are not proportional to the transition frequency and thus were substantially smaller in fractional terms, and on the other hand because the experimental resolution was limited.

4. The confrontation between experiment and theory

4.1. The hyperfine structure

(a) H_2^+

Figure 6 displays the HFS structure for $\nu = 0, 1$; it remains qualitatively the same for higher ν . As early as 1969, Jefferts [32] reported on precision radiofrequency spectroscopy of the hyperfine structure of H_2^+ in levels ($\nu = 4, 5, 6, 7, 8, N = 1, 2$), i.e. in both ortho- and para- H_2^+ . Frequencies of transitions between spin states of a given rovibrational level were measured with 1.5 kHz uncertainty. Because of the small uncertainty and the substantial number of transitions reported, the results are still relevant today. In $N = 1$ levels, there are five hyperfine states; Jefferts' data covers all splittings within. In $N = 2$ levels, there exists only a pair of states $|I = 0, G = 1/2, F = N - 1/2\rangle$ and $|I = 0, G = 1/2, F = N + 1/2\rangle$, split in energy by the interaction between the electron spin $G = 1/2$ and the rotational angular momentum $N = 2$ (Supplemental Material). This splitting was also determined; it decreases with increasing ν , from 81 MHz ($\nu = 4$) to 60 MHz ($\nu = 8$). The HFS theory as of 2016 [37] computed splittings that are in agreement with the experimental data, within the above experimental uncertainty. An improved later calculation [46] allowed a more detailed look at the coefficient $b_F \approx 0.8$ GHz of the dominant interaction term $b_F \mathbf{s}_e \cdot (\mathbf{I}_{p1} + \mathbf{I}_{p2})$ and found agreement with the experimental counterpart to within 0.8 kHz or less, the theoretical and experimental uncertainties both being 0.8 kHz.

In the 1970s, Menasian and Dehmelt [88] reported higher-accuracy results on three transitions previously reported by Jefferts. These were particular spin-rotation splittings in ortho- H_2^+ ($N = 1, \nu = 4, 5, 6$), namely the splitting between $(I = 1, G = 1/2, F = 3/2)$ and $(I = 1, G = 1/2, F = 1/2)$ due to the interaction between the total particle spin $G = 1/2$ and the rotational angular momentum $N = 1$. The measured splittings were ≈ 14 MHz and their experimental uncertainties 2 Hz, exceptionally small. Recent HFS theory [89] predicts the splittings with uncertainty of $\simeq 50$ Hz and is in agreement with experiment.

(b) HD⁺

Important early studies were performed by Carrington et al. using the ion beam technique. Hyperfine components were observed in rovibrational transitions between highly excited vibrational levels and in rotational transitions in highly excited vibrational levels. Transition frequencies were in the far infrared or microwave range. Differences between transition frequencies of spin components and absolute frequencies, respectively, were determined with uncertainties of 0.5 to several MHz. Furthermore, using an infrared/radiofrequency double resonance approach the team was able to observe a substantial number of transitions between spin states *within* the same rovibrational level, again for high vibrational levels ($\nu = 17, 21$). The radiofrequency transitions had uncertainties 0.01–0.7 MHz. The data was compared with the spin theory of the time [80].

For vibrational transitions with small vibrational quantum numbers, individual hyperfine components were first observed only much later, in 2012 [90]. Although that spectroscopy was not Doppler-free, the Doppler broadening was smaller than the typical spacing between hyperfine components, so that these could be resolved. Electron-spin-to-nuclear-spin coupling strengths ($\mathcal{E}_4, \mathcal{E}_5$) in a low-lying vibrational level of HD⁺ were determined. In 2018 a hyperfine component of a rotational transition was observed [83] with sub-Doppler resolution, soon followed by a higher-accuracy measurement of six components [45]. Finally, beginning in 2020 hyperfine components in optical transitions with sub-Doppler resolution were reported [43,51,82].

Since the HFS theory of HD⁺ is closely related to that of H₂⁺ and the latter is well confirmed by comparison with experimental radiofrequency spectroscopy data (see Section 4.1a), one can take the standpoint that the HD⁺ spin theory predictions can be used (i) to check on the correctness of the experimental measurements, and (ii) to deduce spin-averaged frequencies from experimentally measured spin component frequencies (see Section 4.2).

To implement (i), the experiment must measure two or more components (lines) $f_{\text{line } i}$ of a rotational or rovibrational transition. Pairwise differences are spin frequency differences, $f_{\text{line } i} - f_{\text{line } j} = f_{\text{spin},i} - f_{\text{spin},j} = \Delta f_{\text{spin},i,j}$, and have numerical values less or equal to approximately 1 GHz in magnitude. The differences correspond either to a HFS splitting within one rovibrational level (if the two lower states $p(i), p(j)$, or the two upper states $p'(i), p'(j)$, of the two components are identical) or to a double difference of hyperfine energies of the two levels, $E_{\text{spin}}(\nu', N', p'(i)) - E_{\text{spin}}(\nu', N', p'(j)) - (E_{\text{spin}}(\nu, N, p(i)) - E_{\text{spin}}(\nu, N, p(j)))$. It should be noted

that a predicted spin frequency difference $\Delta f_{\text{spin},i,j}^{(\text{theor})}$ is a function of either 11 or 18 (if $N, N' \geq 1$) individual \mathcal{E}_k coefficients. As all coefficients have been assigned a theoretical uncertainty and the correlations between their uncertainties have been determined, also the theoretical uncertainty of $\Delta f_{\text{spin},i,j}^{(\text{theor})}$ can be given. The experimental difference frequencies must be determined with account of the measurable systematic shifts. But they may still be affected by unidentified systematic shifts that act differently on the individual components. Thus, the comparison between experimental difference frequencies $\Delta f_{\text{spin},i,j}^{(\text{exp})}$ and calculated values $\Delta f_{\text{spin},i,j}^{(\text{theor})}$ probes not only the spin theory, but also the quality of the experiments.

Table 3 summarises the recent precision measurements of the HD⁺ spin structure. For transitions f_1 and f_5 the experimental spin structure data and currently most accurate theoretical prediction are consistent. Discrepancies at the level of up to 1 kHz exist for the rotational transition f_0 . In order to obtain a better agreement, ref. [47] the data of the rotational transition has been used to fit the three most critical \mathcal{E} coefficients, and the largest difference between experiment and theory was found to be $\mathcal{E}_1^{(\text{exp})} - \mathcal{E}_1^{(\text{theory})} = -0.5(1)_{\text{exp}}(1)_{\text{theor}}$ kHz, i.e. 3.3σ . In ref. [51], a different analysis was performed. After excluding two spin transitions from the analysis, a fit of $\mathcal{E}_1, \mathcal{E}_2$ resulted in values that differed from the theoretical predictions by -5.4 ± 0.4 and -5.4 ± 2.8 times their respective theory uncertainty. For the two-photon transition $f_9: \nu = 0 \rightarrow \nu' = 9$ the discrepancy between theory and experiment is 8.4 kHz (i.e. 9σ) [47]. Resolving these discrepancies is an important near-term task, in order to achieve consistency of all experiments.

Finally, we mention the sensitivity of the HFS splittings to the electric quadrupole moment of the deuteron Q_d , in order to assess the potential of HD⁺ spectroscopy for its determination, further discussed below in Section 6.3. The sensitivities for the already studied transitions are indicated in the last column of Table 3. Only transitions f_0, f_1, f_5 have relevant sensitivities, one reason being their small values of N, N' compared to the case of transition f_9 . Considering the total (experimental and theoretical combined) uncertainties u_{tot} of the spin differences, we see that the rotational transition f_0 offers the highest effective sensitivity, $Q_d(\partial \Delta f_{\text{spin}} / \partial Q_d) / u_{\text{tot}} \simeq 3 \times 10^{-3}$. To take advantage of this opportunity, first the consistency of the rotational transition data and the HFS theory must be established. An earlier fit of Q_d to the rotational data yielded an uncertainty of 1.5% [45]. For vibrational transitions f_1, f_5 there is agreement between data and HFS theory. From the values of line f_1 in Table 3 one may conclude that the literature value of Q_d is confirmed at the $Q_d(\partial \Delta f_{\text{spin}} / \partial Q_d) / u_{\text{tot}}(f_1) \simeq 2.5\%$ level.

4.2. The spin-averaged transition frequencies

A measured transition is always a spin component i , its frequency is (theoretically) to be interpreted as a sum $f_{\text{line } i} = f_{\text{spin-avg}} + f_{\text{spin},i}$. As mentioned earlier (Section 2.3.3), it is in principle possible to obtain the spin-averaged frequency without knowledge of theoretical spin frequency values if *all* favoured spin components of a transition are measured [26]. The fewer spin components are measured, the more accurate the spin theory values must be. For example, in ref. [45] (reanalysed in ref. [51]) six out of ten favoured spin components were measured, and by an appropriate combination, the spin theory uncertainties were suppressed so well that the spin-averaged frequency was obtained with spin-theory related uncertainty negligible compared to the QED uncertainty (column 3, row 6 in Table 4). In the extreme case that only a single component $f_{\text{line } i}$ is measured, one must fully rely on the availability of an accurate value $f_{\text{spin},i}^{(\text{theor})}$ and the uncertainty of the deduced $f_{\text{spin-avg}}$ will be at least $u(f_{\text{spin},i}^{(\text{theor})})$, currently $\simeq 0.1$ kHz.

In each of three recent vibrational spectroscopy experiments f_1, f_5, f_9 (columns 2,4,5 in Table 4), two spin components $f_{\text{line } a}^{(\text{exp})}, f_{\text{line } b}^{(\text{exp})}$ were measured. One forms the linear superposition

$$f_{\text{spin-avg}}^{(\text{exp})} = d(f_{\text{line } a}^{(\text{exp})} - f_{\text{spin},a}^{(\text{theor})}) + (1-d)(f_{\text{line } b}^{(\text{exp})} - f_{\text{spin},b}^{(\text{theor})}), \quad (6)$$

with the dimensionless weight d . (The superscript on the l.h.s. is not fully accurate, but chosen for simplicity.) If the spin components had no experimental uncertainty and the theoretical spin frequency no theory uncertainty, the value of d would be arbitrary, since both terms in parentheses would then be equal. As this is not the case, $f_{\text{spin-avg}}^{(\text{exp})}$ will have a slight dependence on d . One can therefore choose the value d so as to minimise the total uncertainty of $f_{\text{spin-avg}}^{(\text{exp})}$, taking into account correlations between the uncertainties of the four contributions on the r.h.s., if any. It is notable that because of the high accuracy reached in the spin theory, the spin frequency corrections $f_{\text{spin},a}^{(\text{theor})}, f_{\text{spin},b}^{(\text{theor})}$ applied in the mentioned three experiments do not contribute any substantial uncertainty.

Table 4 presents the spin-averaged transition frequencies related to the four experiments introduced above. Row 3 shows the experimental uncertainties of the spin-averaged frequencies, which range from 1.1 to 13×10^{-12} . Row 9 and 10 contain the main results: experiment and theory of the individual transitions agree at levels between 1.8 and 2.1×10^{-11} , and in all cases the main contribution is the uncertainty coming from the fundamental constant μ/m_e , that enters the theory predictions.

A few comments are in order. Agreement between experiment and theory for transition f_5 is only found if the recoil shift is subtracted. Concerning transition

f_1 , agreement between experiment and theory for the ratio f_5/f_1 (see next subsection) is only obtained if no recoil shift correction is applied to the f_1 experimental frequency. The mentioned (current) incomplete agreement of the experimental and theoretical spin structure for transitions f_0 and f_9 implies that the shown results for $f_{\text{spin-avg}}^{(\text{exp})}$ should be taken cautiously. For the rotational transition f_0 , the reanalysis of ref. [51] is shown.

4.3. Frequency ratios

The ratio $\mathcal{R}_{a,b} = f_a/f_b$ of two vibrational transition frequencies is independent of the Rydberg constant. It is also only weakly dependent on μ/m_e , if the involved vibrational quantum numbers are not large, the residual dependence stemming from the anharmonicity of the nuclear potential. By considering slightly more complicated functions, $f_a/(f_b)^\epsilon$, with $\epsilon \neq 1$, the sensitivity to the mass ratio can be reduced further. Furthermore, the contributions from nuclear, relativistic and from QED effects scale, for vibrational transitions, approximately linearly with the transition frequency. The comparison of column 2 and 4 of Table 4 shows this clearly. This implies that their fractional contributions to frequency ratios \mathcal{R} are substantially reduced, by approximate factors 10–100. Thus, the ratios deemphasise the influence of fundamental constants $R_\infty, \mu/m_e, r_p, r_d$, and of the QED corrections, enhancing the non-relativistic contributions. As a result, the combined theory and CODATA uncertainty is low, e.g. 2.6×10^{-12} for the ratio $f_5/f_1^{0.87}$. (The value depends on the assumed correlation of the uncertainties of the QED contributions.) Note that this is substantially smaller than the QED uncertainty of an individual theoretical transition frequency. Then, the comparison of experimental and theoretical frequency ratios may be used for verifying the consistency of experimental results obtained, by the same or different research groups, on different vibrational transitions. The mentioned ratio $f_5/f_1^{0.87}$ showed an experiment-theory agreement with combined uncertainty 4.2×10^{-12} [51]. Another way to look at this result is to realize that it is one of the most accurate comparisons between a theory prediction and its experimental value. To the best of the author's knowledge, there exist only two instances of higher accuracy: ratios of transition frequencies in atomic hydrogen and the g-factor of the electron.

5. Applications

5.1. Determination of fundamental constants

We discussed earlier that at present the transition frequencies of HD^+ can furnish values for the reduced nuclear mass in units of the electron mass. Thus, one may

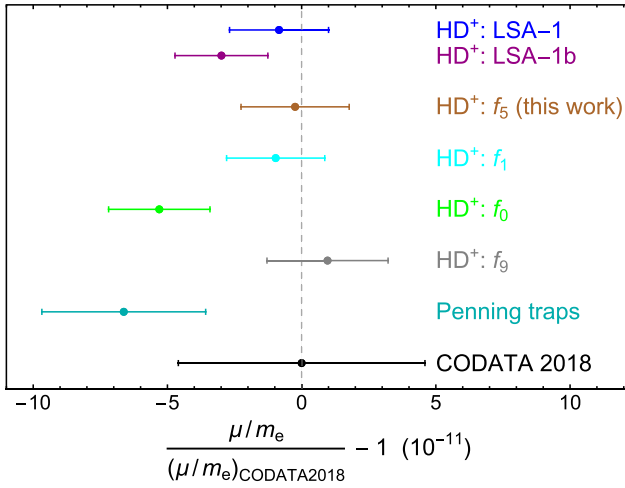


Figure 12. Comparison of values of the mass ratio μ/m_e . $\mu = m_p m_d / (m_p + m_d)$ is the reduced proton-deuteron mass. ‘LSA-1’ (blue): a least-squares fit based on f_1, f_5 . ‘LSA-1b’ (purple): a least-squares fit based on f_0, f_1, f_5 . Measurements: f_5 (brown) [45] (with additional correction); f_1 (cyan) [43] (with additional correction); f_0 (green) [51], f_9 (gray) [85]. ‘Penning traps’ (turquoise): computed using the CODATA 2018 value for m_e/u (that relies mostly on ref. [92]), m_d/u [93], m_d/m_p [67]. ‘CODATA 2018’ (black): μ/m_e computed using only the CODATA values for $m_e/u, m_p/u, m_d/u$. Note that the value and uncertainty of the ‘CODATA 2018’ entry is significantly correlated with the ‘Penning traps’ entry. The ‘LSA-1’ value is offset compared to the values from the individual frequencies because the theory uncertainties of the latter are strongly correlated. From [51].

fit μ/m_e by requiring

$$f_{\text{spin-avg}}^{(\text{theor})}(\mu/m_e) = f_{\text{spin-avg}}^{(\text{exp})}.$$

The quantity on the l.h.s carries the QED theory uncertainty and the CODATA 2018 uncertainties of the fundamental constants R_∞, r_p, r_d , but not of μ/m_e . The r.h.s. comes with the experimental uncertainty. In addition, the r.h.s. will usually also include a spin theory-related uncertainty, since the spin theory results are invoked to obtain the spin-averaged frequency. By using the Taylor expansion of the l.h.s. around the CODATA 2018 value of the fundamental constants, Equation (5), one obtains a value for μ/m_e and an associated uncertainty. For the transitions measured so far, the results are reported in line 20 of Table 4. Figure 12 is a graphic depiction. We see that the uncertainties of the respective μ/m_e values from each of the four HD^+ transitions are moderately smaller than for the value obtained from Penning trap data. LSA-1 (blue) is simultaneous fit of μ/m_e to the two transitions f_1, f_5 .

From the values of μ/m_e one can further obtain the proton-electron mass ratio if one takes into account the value of m_d/m_p determined by the most accurate Penning trap experiment [67]. For example, experiment f_5

yields

$$m_p/m_e = 1\,836.152\,673\,463\,(10)_{\text{exp}}^{(35)}{}_{\text{theor,QED}} \times (1)_{\text{theor,spin}}^{(6)}{}_{\text{CODATA18,Fink-Myers}}, \quad (7)$$

with total fractional uncertainty $u_r = 2.0 \times 10^{-11}$. The value is consistent with m_p/m_e obtained from the atomic masses of electron [1] and proton [94], 1 836.152 673 390 (81), but is two times more accurate.

5.2. Fundamental physics tests

Most if not all precision experiments can be interpreted as tests of fundamental physics principles. Perhaps the most visible example are measurements performed with atomic clocks, whose uncertainty is today reaching less than 1 part in 10^{18} . The measurement of the ratio of the frequencies of two dissimilar atomic clocks, if repeated in time, can be used to constrain a hypothetical time-dependence of fundamental constants, or (for co-located clocks) a hypothetical dependence on the Sun’s gravitational potential. The measurement of the time dilation effect in a gravitational field is a further use of optical clocks in fundamental physics. Such tests are noteworthy in that they do not require an *ab initio* theory capable of predicting the frequency of the clock(s). Concerning precision experiments on MHI, one can similarly consider tests where *ab initio* theory is secondary [53]. However, given that an accurate *ab initio* theory exists (contrary to the atomic clocks), one can also envisage tests where its input is essential.

5.2.1. Confrontation of experiment and theory, testing for the existence of additional interactions

It has been a fundamental endeavour of Physics to determine the forces of nature as precisely as possible. The theoretical description of the forces of the microscopic world is contained in the Standard Model. Nowadays, one seeks to search for effects ‘beyond the Standard Model’, and this includes searches for new forces, that obviously must be weak, if they exist at all. MHI are unique within the ‘ecosystem of precision physics’ outlined in the introduction in that their energies are immediately connected to the force between the two baryons. Of course, the electron-baryon force is also present and equally affects the energies. But on this force, the one-electron atoms provide precise information. Thus, with precision data on such atomic systems as foundation, there arises the opportunity to use MHI experimental data and *ab initio* theory to constrain the strength of a hypothetical additional force between the two baryons. (Just as well, we may view such a force as a modification of the usual Coulomb force).

It is necessary to make an assumption about the form of the additional force. Actually, it is more useful to consider an additional interaction potential $V_{BSM}(R)$, since its effect for any rovibrational level can be computed by first-order perturbation theory as the expectation value $\Delta E_{\text{nonrel}}(\nu, N) = \langle V_{BSM}(R) \rangle_{\nu, N}$. This is the mean of $V_{BSM}(R)$ weighted with the squared nuclear vibrational wavefunction. A well-motivated functional form for V_{BSM} is a Yukawa-type interaction, $V_{BSM}(R) = 2\beta_{pd}R^{-1} \exp(-R/\Lambda)$, which arises from the exchange of a particle of mass proportional to the inverse of the range Λ . (The factor 2 is introduced because of the mass 2 u of the deuteron.) The value of Λ is unknown, so the analysis is performed for different values. A simplified analysis consists in assuming that a BSM force indeed exists and computing its strength $\beta_{pd} = \beta_{pd}(\Lambda)$ from

$$\begin{aligned} hf_{\text{spin-avg}}^{(\text{exp})}(\nu, N, \nu', N') &= hf_{\text{spin-avg}}^{(\text{theor})}(\nu, N, \nu', N') \\ &+ 2\beta_{pd}(\Lambda) (\langle R^{-1} \exp(-R/\Lambda) \rangle_{\nu', N'} \\ &- \langle R^{-1} \exp(-R/\Lambda) \rangle_{\nu, N}). \end{aligned}$$

The solution also yields the uncertainty $u(\beta_{pd}(\Lambda))$; it originates from the uncertainties of $f_{\text{spin-avg}}^{(\text{exp})}$ and of $f_{\text{spin-avg}}^{(\text{theor})}$, and therefore includes all uncertainties discussed so far, including the CODATA uncertainty of the fundamental constants. As is seen from Equation (5) for example, it is indeed the CODATA 2018 uncertainty of the masses that will determine the uncertainty of β and therefore the reach of the test.

Two generalisations are worth mentioning: with a set of HD^+ data available, one can simultaneously determine μ/m_e and β_{pd} [51]. This circumvents the need to use the CODATA 2018 value of μ/m_e and its inaccuracy. The most important uncertainty is then the QED theory uncertainty. The HD^+ data available as of today does not show evidence of the existence of an additional proton-deuteron force.

A second, major generalisation is the following. In the considerations so far, it has been assumed that all is well with the electron-baryon interaction, which in the MHI is as significant as the baryon-baryon interaction [51,85]. That this is so, is shown by hydrogen atom spectroscopy. However, the interpretation of hydrogen spectroscopy data is affected by the charge radii of the proton and the deuteron. These values today come from muonic hydrogen spectroscopy, a system whose forces, the muon-proton force and the muon-deuteron force, could also contain deviations from the Coulomb force.

Thus, we see that a major goal would be an encompassing analysis of the results of all few-body systems, including two-electron systems, leading to bounds to a set of BSM forces. This set is particularly large if one

wishes to differentiate between the baryons p, d, t, e.g. between a proton-proton and a proton-deuteron force.

5.2.2. Testing for deviations from standard quantum mechanics

One can consider deviations from standard quantum mechanics at the level of the Schrödinger equation, i.e. the existence of additional terms. For example, one can consider a local self-interaction term of the form $U_{\text{self}} = \eta |\Psi(\{\mathbf{r}_i\})|^2$, where Ψ is the wavefunction of the system, \mathbf{r}_i are the particle coordinates, and η is an unknown dimensional parameter to be bounded by experiments. The analysis approach is similar to above. It is interesting to note that the vibrational transition frequency ratios mentioned above are sensitive to this type of self-interaction. A preliminary bound to η has been derived [51].

5.2.3. Testing for non-standard quantum physics without the need of *ab initio* theory

A second topic are generalisations of standard quantum mechanics. S. Weinberg has analysed possible experimental consequences of so-called Lindblad quantum mechanics [95]. He suggested to consider atomic clocks with three metastable levels a, b, c and measure the three transition frequencies f_{ab}, f_{bc}, f_{ac} . Then one should verify whether indeed $f_{ab} + f_{bc} = f_{ac}$. No *ab initio* theory of the transition frequencies is required. The present author has suggested to use the MHI for this purpose, since they provide a multitude of metastable levels and the potential for high metrological accuracy [96,97]. A preliminary test of Weinberg's suggestion, relying instead on *ab initio* theory, is discussed in ref. [51].

A (far) future opportunity is a test of the time-independence of the electron-nuclear mass ratio; it is elaborated on below in Section 6.3.

6. Outlook

6.1. Upcoming studies

The current line of work on HD^+ can be pursued to higher experimental accuracy and extended to more transitions. Taking advantage of the correlation of the QED uncertainties it should be possible to improve on some of the physics tests described above. Resolution of the current questions about the hyperfine structure will require a repeat of previous or additional measurements.

6.2. Experiments with single ions

Nowadays, the most accurate spectroscopy of ions is the spectroscopy of atomic ions for optical clocks. It is performed on a single ion or, if necessary because of the

lack of an accessible cycling transition, on a pair of ions, the spectroscopy ion and the ‘logic’ ion [98]. It has been established that under such conditions the control of systematic shifts is possible to a very high degree, down to 1×10^{-18} , currently. It is natural to ask whether similar uncertainties might be achievable for MHI. This question has been analysed theoretically [96,97] and it has been estimated that uncertainties in the 10^{-17} range should be achievable, a level far beyond the present status. Clearly, it is of interest to develop the field in that direction.

A first task consists in developing the methods for preparing single ultracold MHI in a trap. In the field of precision mass spectroscopy in Penning traps, this is today almost standard. Moreover, as the traps are nowadays cryogenic and thus exhibit negligible black-body radiation intensity and excellent vacuum, the MHI are eventually cooled internally to the rovibrational ground state ($v = 0, N = 0$), regardless of being hetero- or homonuclear [19,67]. Currently, the translational energy of the single MHI in Penning traps is several kelvin. In the future, advanced cooling methods (e.g. sympathetic cooling) may allow to lower the temperature. Recently, also in RF traps single MHI, sympathetically cooled by a single beryllium ion, have been prepared [15,16].

A second task is providing methods to detect a spectroscopic transition in the single MHI. For a single HD^+ in a Penning trap this has been achieved for the first time in 2021 using the continuous-Stern-Gerlach-effect technique. Direct spectroscopy of the spin structure was accomplished [19]. This result promises to be useful also for optical spectroscopy of MHI in a Penning trap, as proposed in ref. [99]. In a RF trap one requires a different technique, quantum logic or optical force detection [69,100]. For MHI, these have not yet been shown to be feasible, but experiments are in preparation.

6.3. Possible future studies

1. Obviously, the most important evolution from the present state-of-the-art will be to perform spectroscopy on other MHI species, with the goal of determining the mass ratios m_p/m_e , m_d/m_e , m_t/m_e individually. One approach would involve measuring the three heteronuclear MHI HD^+ , HT^+ and DT^+ , and deducing the ratios from the three corresponding reduced masses. However, this would involve working with radioactive MHI, an endeavour that poses certain safety challenges. m_p/m_e , m_d/m_e can be determined individually by complementing the HD^+ measurements with measurements on H_2^+ or D_2^+ . For example, it has been proposed to measure the ($v = 0, N = 2$) \rightarrow ($v' = 1, N' = 2$) fundamental vibrational transition of H_2^+ by two-photon, Doppler-free spectroscopy using a 9.2 μm laser [60,101]. Electric

quadrupole (E2) one-photon transitions are an alternative [61]. Doppler-free signals should be obtainable as is feasible with E1 transitions in HD^+ . A proof-of-principle experiment has recently shown this [59] (Figure 11).

2. The ‘big goal’ of MHI precision physics in the context of BSM physics consists in setting improved bounds on BSM forces between any two particles. There are four particles (e, p, d, t) and thus potentially 10 different BSM interactions. Taking into account that one must also determine three mass ratios, three nuclear charge radii and the Rydberg constant, the magnitude of the effort appears daunting, especially if no input data from other systems (hydrogen, muonic hydrogen, mass spectrometry) is used. A reduced research program could focus on H_2^+ only, aiming to determine m_p/m_e , β_{ep} , β_{pp} , r_p , R_∞ from a sufficiently large set of vibrational transition frequencies. Input could come from atomic hydrogen spectroscopy, contributing to β_{ep} , r_p , R_∞ .

3. The electric quadrupole moment of the deuteron, Q_d . The most accurate determination of this quantity is from a comparison of precision radiofrequency spectroscopy of neutral molecular hydrogen performed more than half a century ago by Ramsey *et al.* and the recent accurate *ab initio* theory of the molecule. This resulted in $Q_d = 0.285699(15)_{\text{theo}}(18)_{\text{exp}} \text{fm}^2$ [57]. Note the impressive total uncertainty below 1×10^{-4} . The theory uncertainty arises because the hyperfine interactions were treated in Breit–Pauli approximation, which omits terms of fractional order α^2 . It is also notable that the total uncertainty is 200 times smaller than the most accurate value obtained from nuclear physics experiment and theory [102]. As described, the spin frequencies of HD^+ , D_2^+ and DT^+ are also affected by Q_d . The computation of the spin hamiltonian coefficients (in HD^+ , $\mathcal{E}_9 \propto Q_d$, in D_2^+ , $\mathcal{E}_6 \propto Q_d$ [40]) and of the spin structure yields the sensitivities of the spin frequencies to Q_d . Values of up to approximately 100 kHz/ fm^2 are found, see [40] and Table 3. An experimental spectroscopic accuracy at the level of 1 Hz is therefore required in order to obtain a competitive uncertainty for Q_d . This appears possible using radiofrequency spectroscopy, either in an RF trap or in a Penning trap. Achieving this accuracy in rovibrational spectroscopy would be challenging; moreover, at least two spin components would need to be measured, in order not to incur the QED uncertainty of the spin-averaged frequency. Similar to neutral molecular hydrogen, also for the MHI the computation of $\mathcal{E}_{6,9}/Q_d$ has so far been performed only in Breit–Pauli approximation. The prospect of more accurate experimental measurements may motivate a more accurate theory.

4. The triton is a three-nucleon system with spin 1/2 and zero quadrupole moment. Its charge radius is

experimentally determined as $r_t^{(\text{es})} = 1.755(86)$ fm from electron scattering (es) experiments. The 5% fractional uncertainty is substantially larger than that of r_p and r_d . The triton is of particular interest in nuclear physics because a quantity related to the charge radius, the *point* charge radius δr_C , can be computed using effective field theory. A recent theoretical calculation yielded $\delta r_C = 1.62(3)$ fm [103]. The value extracted from experimental data via the relation $(\delta r_C^{(\text{exp})})^2 = (r_t^{(\text{exp})})^2 - (r_p^{(\text{exp})})^2 - 2(r_n^{(\text{exp})})^2$ is in agreement, $\delta r_C^{(\text{exp})} \simeq 1.598(40)$ fm (n is the neutron). Very recently, a different calculation [104] yielded a preliminary value $r_t = 1.773(9)$ fm, where the experimentally determined ^3He charge radius was used as one input datum. It is more accurate than $r_t^{(\text{es})}$, thus prompting the need for more accurate measurements. This might be accomplished combining precision theory and spectroscopy of HT^+ . The nuclear volume shift in HT^+ due to the triton may be estimated [36] as $-302(30)_{\text{es}}$ kHz for the $f_5 : (0, 0) \rightarrow (5, 1)$ transition. The stated uncertainty (from $u(r_t^{(\text{es})})$) may be compared with the uncertainty arising from undetermined QED corrections, which is likely to be similar to that for HD^+ , $\simeq 2$ kHz, and from the reduced mass uncertainty, $\simeq 7$ kHz, which is dominated by $u(m_p/m_e)$. Thus, there is the prospect of determining r_t more accurately by factor of approximately four. Once the value of m_p/m_e is determined more precisely via HD^+/H_2^+ spectroscopy, a further improvement of r_t may follow.

5. Intercomparisons of atomic and molecular frequency standards performed over long time spans can be used to search for a hypothetical drift of the fundamental constants. Atomic transition frequencies are sensitive to the fine-structure constant (in all standards) and, in microwave standards, additionally to the proton-to-electron mass ratio and nuclear g -factors. Inter-comparisons of optical atomic standards (optical clocks) have set impressive upper bounds to a drift of α . A few measurements on molecules have been performed in the past, with metrological performance weak compared to today's performance of atomic clocks. Comparisons between cesium fountain clocks and an optical atomic ion clock have been performed over nearly a decade, leading to a strong bound on the drift rate of m_p/m_e , $-0.8(3.6) \times 10^{-17}/\text{yr}$ [105]. In view of this, could the MHI play a role [53]? It has been argued that the transition frequencies of MHI can be determined with uncertainties in the low 10^{-17} range. Thus, MHI precision spectroscopy could eventually lead to stricter bounds than those obtainable with the Cs clock. It is important to remark that also many other molecules, including other molecular ions, that can be provided trapped and ultracold, are candidates for performing such tests. In addition, hyperfine transitions in

highly charged ions, at optical frequencies, are suitable candidates [106]. Theoretical analyses on the metrological potential of such systems have been performed and experimental studies are under way.

6.4. Spectroscopy of anti-MHI

A key test of CPT invariance is being pursued by optical spectroscopy of antihydrogen. The $1s - 2s$ transition frequency of hydrogen is proportional to the Rydberg constant, i.e. to $m_e q_e^2 q_p^2$ (q is the charge), with a small correction ($\propto m_e/m_p$ fractionally) arising from centre-of-mass motion, and a 4×10^{-10} fractional contribution from the finite charge radius of the proton. Thus, the comparison of hydrogen and antihydrogen optical frequencies tests for CPT invariance concerning several particle properties. Furthermore, independent experiments have determined that the charges of electron and proton are equal and opposite to an extreme degree; for antimatter this has been verified with lower precision (1×10^{-12} level). In terms of parameters of the Standard Model, the comparison tests for CPT invariance of the fine-structure constant (i.e. the strength of the lepton-baryon interaction), the electron mass and, via the nuclear radii, the QCD energy scale.

It is conceivable that the anti-hydrogen optical spectroscopy reaches the 10^{-17} uncertainty level. However, because the sensitivity of the (anti)hydrogen spectroscopy to the (anti)proton mass is small, other approaches for testing the equality of antiproton and proton mass are desirable. Measurement of the charge-to-mass ratios of the proton and of the antiproton in a Penning trap is such an approach, and a test at the 1.6×10^{-11} level has been achieved at CERN, with prospects of further improvement.

One can argue that a powerful test of CPT symmetry could also be implemented by comparison of vibrational transition frequencies of H_2^+ and anti- H_2^+ . This 'holy grail' of MHI spectroscopy was originally proposed by Dehmelt [107] and recently analysed by Myers [99]. The possibility of producing anti- H_2^+ has been discussed [108], and modelling has suggested associative ionisation of two anti-hydrogen atoms in the $2s$ - state to be a possible pathway.

Because the accuracy potential of MHI vibrational spectroscopy is the 10^{-17} level [96,97], and because of the first-order dependence of the vibrational transition frequencies on the electron-proton mass ratio, a MHI-CPT test of proton-antiproton mass equality could be orders of magnitude more accurate than current alternatives.

It is pertinent to reexamine the dependence of the vibrational frequencies on the fundamental constants. In Sec. 2.2.2. we derived the scaling $f_{\text{vib}} \propto$

$R_\infty m_e^{1/2} m_p^{-1/2}$. This is valid for transitions between levels with small ν, ν' . For a general vibrational transition, the second and third factors are replaced by $(m_e/m_p)^\zeta$. The factor R_∞ is to be replaced by $R_\infty q_e^{4+\kappa} q_p^{-\kappa}$, where q is now the charge of the particle relative to its nominal charge ($-e$ or $+e$). The exponents $\zeta((\nu, N), (\nu', N'))$ and $\kappa((\nu, N), (\nu', N'))$ can be computed approximately in the Born-Oppenheimer approximation or precisely from numerical solutions of the nonrelativistic three-body problem. From the latter, we find that κ varies strongly with ν, ν' . For example, $\kappa((0, 0), (1, 0)) \simeq -0.087$, $\kappa((1, 0), (3, 2)) \simeq 0.023$. For the anti- H_2^+ , for simplicity we assume that the antiproton-antiproton interaction retains the R^{-1} dependence, and at most the antiproton and positron charges are modified.

The MHI-CPT test consists in measuring the frequency ratio

$$\frac{f_{\text{vib}}(\nu, \nu')}{\bar{f}_{\text{vib}}(\nu, \nu')} = \frac{q_e^{4+\kappa} q_p^{-\kappa} m_e^{1+\zeta} m_p^{-\zeta}}{q_{e^+}^{4+\kappa} q_{\bar{p}}^{-\kappa} m_{e^+}^{1+\zeta} m_{\bar{p}}^{-\zeta}}.$$

Here, \bar{f}_{vib} is the frequency of the same transition in anti- H_2^+ . The r.h.s. is a (symbolic) expression that describes the sensitivity of the experimentally measurable frequency ratio on the particle properties (assuming their deviations from the nominal values to be small). Not shown is a small (3×10^{-10}) contribution from the proton and antiproton charge radii, as discussed in Sec. 2.3.4.

Unless the independent verification of charge neutrality for antimatter improves by five orders of magnitude compared to the present status, it would be advantageous to choose a transition for which κ differs substantially from zero, so as to allow a verification.

Thus, the test would be sensitive to all those constants and interactions that are tested separately in other experiments: comparisons of $e - e^+$ mass-to-charge ratio, $p - \bar{p}$ charge-to-mass ratio, $\text{H} - \bar{\text{H}}$ electronic transition frequency, $g_e - g_{e^+}$ (i.e. QED), $g_p - g_{\bar{p}}$ (i.e. nuclear structure). Arguably, a MHI-CPT test could reach higher accuracy than the first and second test; comparable accuracy to even future versions of the second and third test; but lower accuracy than the fifth test. Moreover, the MHI-CPT test would also comprise a CPT test of the otherwise not precisely testable $\bar{p} - \bar{p}$ interaction.

7. Conclusion

As a consequence of continued developments performed over the past two decades, precision rovibrational spectroscopy of the MHI today stands at the low- 10^{-12} uncertainty level for one species, a noteworthy improvement

from the 1×10^{-6} level set nearly half-a century ago by Lamb and coworkers. This has been possible by radically changing the experimental approach. Equally impressive have been the advances in *ab initio* theory, which have covered a comparable factor. Based on the progress in these two areas, the established result as of today is the possibility of determining a particular combination of fundamental constants, $m_e/m_p + m_e/m_d$, with accuracy competitive with the most precise alternative determination via Penning trap mass spectrometry on the individual particles. With this achievement, MHI spectroscopy has been demonstrated to represent a link between the mass spectrometry of the simplest particles and the spectroscopy of the hydrogen atom. The determination of the above mass ratio combination by MHI spectroscopy has only been possible after the proton and deuteron charge radii were determined by other means (hydrogen and muonic hydrogen spectroscopy). Four precision spectroscopy studies on HD^+ have been performed and their experimental accuracies were at or below the level of the current QED theory uncertainty. Substantial improvements in the accuracy of the above mass ratio are therefore not straightforward. The confrontation of MHI theory and MHI experiment has also permitted realising some novel and improved tests of fundamental physics. It is noteworthy that the confrontation of frequency ratios appears to be the third-most accurate confrontation in all of physics.

It is expected that further improvements in experimental accuracy of HD^+ spectroscopy will be achieved in the near future, using single- or two-ion trapping and interrogation techniques. There are also plenty of opportunities to perform precision measurements on other MHI, such as H_2^+ , D_2^+ , HT^+ ; these MHI can be investigated using similar approaches as those demonstrated on HD^+ and on altogether different diatomic molecular ions. This should lead to determinations of the individual nuclear mass ratios and to additional and more accurate tests of fundamental physics concepts. The author hopes that the success achieved so far and the probable progress on the experimental side will stimulate strong efforts on the QED theory front. Such efforts appear very worthwhile, albeit challenging.

Acknowledgments

The manuscript benefited from many helpful comments by M. R. Schenkel and D. Bakalov. I wish to express my sincere gratitude to the present and past members of my team who contributed to developing the field of precision spectroscopy of MHI during the last decade: S. Alighanbari, I. Kortunov, M. R. Schenkel, C. Wellers, G. S. Gouri, M. G. Hansen, V. Vogt, E. Wiens, J. Shen, U. Bressel, A. Borodin. Continued skilled technical support has been given by U. Rosowski, D. Iwaschko, R.

Gusek, P. Dutkiewicz. I appreciate the contribution of the visiting scientists K. R. Brown and F. Constantin. V. I. Korobov and D. Bakalov have been crucial partners in the development of the field and I am deeply thankful for our joint cooperation spanning two decades. I also appreciate the recently initiated cooperation with S. Sturm, F. Heiße, C. König, K. Blaum.

Disclosure statement

No potential conflict of interest was reported by the author.

Funding

Some of the work described here has received funding from the European Research Council (ERC) under the European Union's Horizon 2020 research and innovation programme [grant agreement No. 786306, 'PREMOL'] and from both DFG and the state of Nordrhein-Westfalen via grants INST 208/737-1 FUGG, INST 208/774-1 FUGG, INST 208/796-1 FUGG, DFG grant Schi 431/23-1 and finally via scholarships of the Prof.-W.-Behmenburg-Schenkung.

Notes on contributor

S. Schiller graduated from Technische Universität München in 1987 and received a Ph.D. in Applied Physics from Stanford University in 1993. He was a group leader and lecturer at Universität Konstanz until 1999, when he moved to Heinrich-Heine-Universität Düsseldorf as full professor of experimental physics. He made early contributions to the development of continuous-wave optical parametric oscillators, turning them into devices suitable for spectroscopy, to quantum nondemolition measurements, and to quantum tomography. He and his team introduced cryogenic optical resonators and performed highly sensitive tests of the isotropy of light propagation. He introduced and patented the concept of dual frequency comb spectroscopy. Last, but not least, he initiated the field of spectroscopy of sympathetically cooled molecular ions.

ORCID

S. Schiller  <http://orcid.org/0000-0002-0797-8648>

References

- [1] Tiesinga E, Mohr PJ, Newell DB, et al. CODATA recommended values of the fundamental physical constants: 2018. *Rev Mod Phys.* 2021;93:025010. DOI:10.1103/RevModPhys.93.025010
- [2] Schneider A, Sikora B, Dickopf S, et al. Direct measurement of the $^3\text{He}^+$ magnetic moments. *Nature.* 2022;606:878–883. DOI:10.1038/s41586-022-04761-7
- [3] Sturm S, Köhler F, Zatorski J, et al. High-precision measurement of the atomic mass of the electron. *Nature.* 2014;506:467–470. DOI:10.1038/nature13026
- [4] Carrington A, Kennedy RA. Chapter 26 – Spectroscopy and structure of the hydrogen molecular ion. In: Bowers MT, editor. *Ions and light.* Academic Press; 1984. p. 393–442. DOI:10.1016/B978-0-12-120803-5.50016-4
- [5] Carrington A, McNab IR, Montgomerie CA. Spectroscopy of the hydrogen molecular ion. *J Phys B: At Mol Opt Phys.* 1989;22:3551–3586. DOI:10.1088/0953-4075/22/22/006
- [6] Leach CA, Moss RE. Spectroscopy and quantum mechanics of the hydrogen molecular cation: a test of molecular quantum mechanics. *Annu Rev Phys Chem.* 1995;46:55–82. DOI:10.1146/annurev.pc.46.100195.000415
- [7] Zhong Z-X, Tong X, Yan Z-C, et al. High-precision spectroscopy of hydrogen molecular ions. *Chin Phys B.* 2015;24:053102. DOI:10.1088/1674-1056/24/5/053102
- [8] Schiller S. Corrections and Addenda to 'Precision spectroscopy of molecular hydrogen ions: an introduction'. 2023. available at <https://www.exphy.uni-duesseldorf.de/arbeitsgruppen/arbeitsgruppe-prof-schiller/publikationen/precisionspectroscopyofmhi>
- [9] Loch R, Stengler R, Werth G. Measurement of the electronic g factor of H_2^+ . *Phys Rev A.* 1988;38:5484–5488. DOI:10.1103/PhysRevA.38.5484
- [10] Aasbrink L. The photoelectron spectrum of H_2 . *Chem Phys Lett.* 1970;7:549–552. DOI:10.1016/0009-2614(70)80169-5
- [11] Wing WH, Ruff GA, Lamb WE, et al. Observation of the infrared spectrum of the hydrogen molecular ion HD^+ . *Phys Rev Lett.* 1976;36:1488–1491. DOI:10.1103/PhysRevLett.36.1488
- [12] Arcuni PW, Fu ZW, Lundeen SR. Energy difference between the ($\nu = 0, R = 1$) and the ($\nu = 0, R = 3$) states of H_2^+ , measured with interseries microwave spectroscopy of H_2 Rydberg states. *Phys Rev A.* 1990;42:6950–6953. DOI:10.1103/PhysRevA.42.6950
- [13] Cruse HA, Jungen C, Merkt F. Hyperfine structure of the ground state of para- D_2^+ by high-resolution Rydberg-state spectroscopy and multichannel quantum defect theory. *Phys Rev A.* 2008;77:042502. DOI:10.1103/PhysRevA.77.042502
- [14] Roth B, Koelemeij JCJ, Daerr H, et al. Rovibrational spectroscopy of trapped molecular hydrogen ions at millikelvin temperatures. *Phys Rev A.* 2006;74:040501. DOI:10.1103/PhysRevA.74.040501
- [15] Wellers C, Schenkel MR, Giri GS, et al. Controlled preparation and vibrational excitation of single ultracold molecular hydrogen ions. *Mol Phys.* 2021;120:e2001599. DOI:10.1080/00268976.2021.2001599
- [16] Kienzler D. Conf. on trapped charged particles. Germany: Glashütten; 2022
- [17] König CM, Heiße F, Morgner J, et al. Hyperfine spectroscopy of single molecular hydrogen ions in a Penning trap at ALPHATRAP. International Conference on Precision Physics of Simple Atomic Systems. 2022.
- [18] Carrington A, McNab IR, Montgomerie CA, et al. Electronic spectrum ($2p\sigma_u - 1s\sigma_g$) of the D_2^+ ion. *Mol Phys.* 1989;67:711–738. DOI:10.1080/00268978900101401
- [19] Hunter G, Yau AW, Pritchard HO. Rotation-vibration level energies of the hydrogen and deuterium molecules. *At Data Nucl Data Tables.* 1974;14:11–20. DOI:10.1016/S0092-640X(74)80027-6
- [20] Moss R. Calculations for vibration-rotation levels of HD^+ , in particular for high N. *Mol Phys.* 1993;78:371–405. DOI:10.1080/00268979300100291
- [21] Korobov VI, Karr J-P. Rovibrational spin-averaged transitions in the hydrogen molecular ions. *Phys Rev A.* 2021;104:032806. DOI:10.1103/PhysRevA.104.032806

- [22] Korobov VI. Coulomb three-body bound-state problem: variational calculations of nonrelativistic energies. *Phys Rev A*. 2000;61:064503. DOI:10.1103/PhysRevA.61.064503
- [23] Schnitzler H. Development of an experiment for trapping, cooling, and spectroscopy of molecular hydrogen ions [Ph.D. thesis]. Universität Konstanz; 2001. available at <https://kops.uni-konstanz.de/handle/123456789/9199>
- [24] Blythe P, Roth B, Fröhlich U, et al. Production of ultracold trapped molecular hydrogen ions. *Phys Rev Lett*. 2005;95:183002. DOI:10.1103/PhysRevLett.95.183002
- [25] Aznabayev DT, Bekbaev AK, Korobov VI. Leading-order relativistic corrections to the rovibrational spectrum of H_2^+ and HD^+ molecular ions. *Phys Rev A*. 2019;99:012501. DOI:10.1103/PhysRevA.99.012501
- [26] Schiller S, Korobov VI. Canceling spin-dependent contributions and systematic shifts in precision spectroscopy of molecular hydrogen ions. *Phys Rev A*. 2018;98:022511. DOI:10.1103/PhysRevA.98.022511
- [27] Korobov VI. Variational Methods in the Quantum Mechanical Three-Body Problem with a Coulomb Interaction. *Physics of Particles and Nuclei*. 2022;53:1–20. DOI:10.1134/S1063779622010038
- [28] Paz G. An introduction to NRQED. *Mod Phys Lett A*. 2015;30:1550128. DOI:10.1142/S021773231550128X
- [29] Jentschura UD, Mohr PJ, Soff G. Electron self-energy for the K and L shells at low nuclear charge. *Phys Rev A*. 2001;63:042512. DOI:10.1103/PhysRevA.63.042512
- [30] Karshenboim SG, Ozawa A, Shelyuto VA, et al. The Lamb shift of the 1s state in hydrogen: Two-loop and three-loop contributions. *Phys Lett B*. 2019;795:432–437. DOI:10.1016/j.physletb.2019.06.023
- [31] Dalgarno A, Patterson TNL, Somerville WB. The hyperfine structure of the hydrogen molecular ion. *Proc R Soc Lond A: Math Phys Eng Sci*. 1961;259:100–109. DOI:10.1098/rspa.1960.0213
- [32] Jefferts KB. Hyperfine structure in the molecular ion H_2^+ . *Phys Rev Lett*. 1969;23:1476–1478. DOI:10.1103/PhysRevLett.23.1476
- [33] Bakalov D, Korobov VI, Schiller S. High-precision calculation of the hyperfine structure of the HD^+ ion. *Phys Rev Lett*. 2006;97:243001. DOI:10.1103/PhysRevLett.97.243001
- [34] Korobov VI, Hilico L, Karr J-P. Hyperfine structure in the hydrogen molecular ion. *Phys Rev A*. 2006;74:040502. DOI:10.1103/PhysRevA.74.040502
- [35] Korobov VI, Hilico L, Karr J-P. Relativistic corrections of $m\alpha^6(m/M)$ order to the hyperfine structure of the H_2^+ molecular ion. *Phys Rev A*. 2009;79:012501. DOI:10.1103/PhysRevA.79.012501
- [36] Bekbaev AK, Korobov VI, Dineykh M. Hyperfine structure and relativistic corrections to ro-vibrational energies of HT^+ ions. *J Phys B: At. Mol. Opt. Phys*. 2013;46:175101. DOI:10.1088/0953-4075/46/17/175101
- [37] Korobov VI, Koelemeij JCJ, Hilico L, et al. Theoretical hyperfine structure of the molecular hydrogen ion at the 1 ppm level. *Phys Rev Lett*. 2016;116:053003. DOI:10.1103/PhysRevLett.116.053003
- [38] Korobov VI, Karr J-P, Haidar M, et al. Hyperfine structure in the H_2^+ and HD^+ molecular ions at order $m\alpha^6$. *Phys Rev A*. 2020;102:022804. DOI:10.1103/PhysRevA.102.022804
- [39] Haidar M, Zhong Z-X, Korobov VI, et al. Nonrelativistic QED approach to the fine- and hyperfine-structure corrections of order $m\alpha^6$ and $m\alpha^6(m/M)$: application to the hydrogen atom. *Phys Rev A*. 2020;101:022501. DOI:10.1103/PhysRevA.101.022501
- [40] Danev P, Bakalov D, Korobov VI, et al. Hyperfine structure and electric quadrupole transitions in the deuterium molecular ion. *Phys Rev A*. 2021;103:012805. DOI:10.1103/PhysRevA.103.012805
- [41] Korobov VI. Precision spectroscopy of the hydrogen molecular ions: present status of theory and experiment. *Phys Part Nucl*. 2022;53:787–789. DOI:10.1134/S1063779622040086
- [42] Bakalov D, Korobov V, Schiller S. Magnetic field effects in the transitions of the HD^+ molecular ion and precision spectroscopy. *J Phys B: At Mol Opt Phys*. 2011;44:025003. DOI:10.1088/0953-4075/44/2/025003
- [43] Kortunov IV, Alighanbari S, Hansen MG, et al. Proton–electron mass ratio by high-resolution optical spectroscopy of ion ensembles in the resolved-carrier regime. *Nat Phys*. 2021;17:569–573. DOI:10.1038/s41567-020-01150-7
- [44] Korobov VI, Karr J-P. Spin-orbit interaction in the HD^+ ion. *Eur Phys J D*. 2022;76:197. DOI:10.1140/epjd/s10053-022-00522-3
- [45] Alighanbari S, Giri GS, Constantin FL, et al. Precise test of quantum electrodynamics and determination of fundamental constants with HD^+ ions. *Nature*. 2020;581:152–158. DOI:10.1038/s41586-020-2261-5
- [46] Karr J-P, Haidar M, Hilico L, et al. Higher-order corrections to spin–spin scalar interactions in HD^+ and H_2^+ . *Phys Rev A*. 2020;102:052827. DOI:10.1103/PhysRevA.102.052827
- [47] Haidar M, Korobov VI, Hilico L, et al. Higher-order corrections to the spin–orbit and spin–spin tensor interactions in HD^+ . *Phys Rev A*. 2022;106:042815. DOI:10.1103/PhysRevA.106.042815
- [48] Schiller S, Kortunov I, Hernández Vera M, et al. Quantum state preparation of homonuclear molecular ions enabled via a cold buffer gas: an ab initio study for the H_2^+ and the D_2^+ case. *Phys Rev A*. 2017;95:043411. DOI:10.1103/PhysRevA.95.043411
- [49] Korobov VI. private communications 2018, 2021.
- [50] Korobov VI, Hilico L, Karr J-P. Fundamental transitions and ionization energies of the hydrogen molecular ions with few ppt uncertainty. *Phys Rev Lett*. 2017;118:233001. DOI:10.1103/PhysRevLett.118.233001
- [51] Alighanbari S, Kortunov IV, Giri GS, et al. Test of charged baryon interaction with high-resolution vibrational spectroscopy of molecular hydrogen ions. *Nat Phys*. 2022. DOI:10.1038/s41567-023-02088-2
- [52] Bishop DM, Cheung LM. Calculation of transition frequencies for H_2^+ and its isotopes to spectroscopic accuracy. *Phys Rev A*. 1977;16:640–645. DOI:10.1103/PhysRevA.16.640
- [53] Schiller S, Korobov V. Test of time-dependence of the electron and nuclear masses with ultracold molecules. *Phys Rev A*. 2005;71:032505. DOI:10.1103/PhysRevA.71.032505

- [54] Karr J-P, Hilico L, Koelemeij JCJ, et al. Hydrogen molecular ions for improved determination of fundamental constants. *Phys Rev A*. 2016;94:050501. DOI:10.1103/PhysRevA.94.050501
- [55] Hegstrom RA. g factors and related magnetic properties of molecules. Formulation of theory and calculations for H_2^+ , HD^+ , and D_2^+ . *Phys Rev A*. 1979;19:17–30. DOI:10.1103/PhysRevA.19.17
- [56] Karr J-P. Leading-order relativistic corrections to the g factor of H_2^+ . *Phys Rev A*. 2021;104:032822. DOI:10.1103/PhysRevA.104.032822
- [57] Puchalski M, Komasa J, Pachucki K. Hyperfine structure of the first rotational level in H_2 , D_2 and HD molecules and the deuteron quadrupole moment. *Phys Rev Lett*. 2020;125:253001. DOI:10.1103/PhysRevLett.125.253001
- [58] Bates DR, Poots G. Properties of the hydrogen molecular ion I: quadrupole transitions in the ground electronic state and dipole transitions of the isotopic ions. *Proc Phys Soc Sect A*. 1953;66:784–792. DOI:10.1088/0370-1298/66/9/302
- [59] Schenkel MR, Alighanbari S, Schiller S. (Universität Düsseldorf), unpublished.
- [60] Karr J-P, Bielsa F, Douillet A, et al. Vibrational spectroscopy of H_2^+ : hyperfine structure of two-photon transitions. *Phys Rev A*. 2008;77:063410. DOI:10.1103/PhysRevA.77.063410
- [61] Korobov VI, Danev P, Bakalov D, et al. Laser-stimulated electric quadrupole transitions in the molecular hydrogen ion H_2^+ . *Phys Rev A*. 2018;97:032505. DOI:10.1103/PhysRevA.97.032505
- [62] Amitay Z, Zajfman D, Forck P. Rotational and vibrational lifetime of isotopically asymmetric homonuclear diatomic molecular ions. *Phys Rev A*. 1994;50:2304–2308. DOI:10.1103/PhysRevA.50.2304
- [63] Olivares Pilón H, Baye D. Dipole transitions in the bound rotational-vibrational spectrum of the heteronuclear molecular ion HD^+ . *Phys Rev A*. 2013;88:032502. DOI:10.1103/PhysRevA.88.032502
- [64] Colbourn EA, Bunker PR. Accurate theoretical vibration-rotation energies and transition moments for HD^+ , HT^+ , and DT^+ . *J Mol Spectrosc*. 1976;63:155–163. DOI:10.1016/0022-2852(76)90001-1
- [65] Posen AG, Dalgarno A, Peek JM. The quadrupole vibration-rotation transition probabilities of the molecular hydrogen ion. *At Data Nucl Data Tables*. 1983;28:265–277. DOI:10.1016/0092-640X(83)90017-7
- [66] Olivares Pilón H, Baye D. Quadrupole transitions in the bound rotational-vibrational spectrum of the hydrogen molecular ion. *J Phys B: At Mol Opt Phys*. 2012;45:065101. DOI:10.1088/0953-4075/45/6/065101
- [67] Fink DJ, Myers EG. Deuteron-to-proton mass ratio from simultaneous measurement of the cyclotron frequencies of H_2^+ and D^+ . *Phys Rev Lett*. 2021;127:243001. DOI:10.1103/PhysRevLett.127.243001
- [68] Karr J-P. Stark quenching of rovibrational states of H_2^+ due to motion in a magnetic field. *Phys Rev A*. 2018;98:062501. DOI:10.1103/PhysRevA.98.062501
- [69] Koelemeij JCJ, Roth B, Schiller S. Blackbody thermometry with cold molecular ions and application to ion-based frequency standards. *Phys Rev A*. 2007;76:023413. DOI:10.1103/PhysRevA.76.023413
- [70] Schneider T, Roth B, Duncker H, et al. All-optical preparation of molecular ions in the rovibrational ground state. *Nat Phys*. 2010;6:275–278. DOI:10.1038/NPHYS1605
- [71] Fröhlich U, Roth B, Antonini P, et al. Ultracold trapped molecules: Novel systems for tests of the time-independence of the electron-to-proton mass ratio. *Astrophysics, Clocks and Fundamental Constants*. 2004:297–307. DOI:10.1007/978-3-540-40991-5_18
- [72] Gosh PK. Ion traps. Clarendon Press: Oxford; 1995.
- [73] Werth G, Gheorghe VN, Major FG. Charged particle traps II. Berlin: Springer; 2009. DOI:10.1007/978-3-540-92261-2
- [74] Knoop M, Madsen N, Thompson RC. Trapped charged particles: a graduate textbook with problems and solutions. Singapore: World Scientific Publishing Co.; 2016. DOI:10.1142/q0004
- [75] Roth B, Schiller S. Cold Molecules, Taylor and Francis, 2009, Ch. Sympathetically cooled molecular ions: from principles to first applications. p. 651–704. available at <http://arxiv.org/abs/0812.1154>
- [76] Schiller S, Lämmerzahl C. Molecular dynamics simulation of sympathetic crystallization of molecular ions. *Phys Rev A*. 2003;68:053406. DOI:10.1103/PhysRevA.68.053406
- [77] Fröhlich U, Roth B, Schiller S. Ellipsoidal Coulomb crystals in a linear radio-frequency trap. *Phys Plasmas*. 2005;12:073506. DOI:10.1063/1.1976605
- [78] Berkeland DJ, Miller JD, Bergquist JC, et al. Minimization of ion micromotion in Paul trap. *J Appl Phys*. 1998;83:5025–5033. DOI:10.1063/1.367318
- [79] Hornekaer L, Kjærgaard N, Thommesen AM, et al. Structural properties of two-component Coulomb crystals in linear Paul traps. *Phys Rev Lett*. 2001;86:1994–1997. DOI:10.1103/PhysRevLett.86.1994
- [80] Carrington A, McNab IR, Montgomerie-Leach CA, et al. Vibration-rotation spectroscopy of the HD^+ ion near the dissociation limit. *Mol Phys*. 1991;72:735–762. DOI:10.1080/00268979100100531
- [81] Critchley ADJ, Hughes AN, McNab IR. Direct measurement of a pure rotation transition in H_2^+ . *Phys Rev Lett*. 2001;86:1725–1728. DOI:10.1103/PhysRevLett.86.1725
- [82] Patra S, Germann M, Karr J-P, et al. Proton-electron mass ratio from laser spectroscopy of HD^+ at the part-per-trillion level. *Science*. 2020;369:1238–1241. DOI:10.1126/science.aba0453
- [83] Alighanbari S, Hansen MG, Korobov VI, et al. Rotational spectroscopy of cold and trapped molecular ions in the Lamb-Dicke regime. *Nat Phys*. 2018;14:555–559. DOI:10.1038/s41567-018-0074-3
- [84] Schiller S, Roth B, Lewen F, et al. Ultra-narrow-linewidth continuous-wave THz sources based on multiplier chains. *Appl Phys B*. 2009;95:55–61. DOI:10.1007/s00340-008-3279-9
- [85] Germann M, Patra S, Karr J-P, et al. Three-body QED test and fifth-force constraint from vibrations and rotations of HD^+ . *Phys Rev Res*. 2021;3:L022028. DOI:10.1103/physrevresearch.3.L022028
- [86] Schiller S, Bakalov D, Bekbaev AK, et al. Static and dynamic polarizability and the Stark and blackbody-radiation frequency shifts of the molecular hydrogen

- ions H_2^+ , HD^+ , and D_2^+ . *Phys Rev A*. 2014;89:052521. DOI:10.1103/PhysRevA.89.052521
- [87] Bakalov D, Schiller S. The electric quadrupole moment of molecular hydrogen ions and their potential for a molecular ion clock. *Appl Phys B*. 2014;114:213–230. DOI:10.1007/s00340-013-5703-z
- [88] Menasian SC, Dehmelt HG. High-resolution study of $(1, 1/2, 1/2) - (1, 1/2, 3/2)$ HFS transition in H_2^+ . *Bull Am Phys Soc*. 1973;18:408–408.
- [89] Haidar M, Korobov VI, Hilico L, et al. Higher-order corrections to spin-orbit and spin-spin tensor interactions in hydrogen molecular ions: theory and application to H_2^+ . *Phys Rev A*. 2022;106:022816. DOI:10.1103/PhysRevA.106.022816
- [90] Bressel U, Borodin A, Shen J, et al. Manipulation of individual hyperfine states in cold trapped molecular ions and application to HD^+ frequency metrology. *Phys Rev Lett*. 2012;108:183003. DOI:10.1103/PhysRevLett.108.183003
- [91] Korobov VI, Karr J-P. Spin-orbit interaction in the HD^+ ion. *Eur Phys J D*. 2022;76:197. DOI:10.1140/epjd/s10053-022-00522-3
- [92] Köhler F, Sturm S, Kracke A, et al. The electron mass from g -factor measurements on hydrogen-like carbon $^{12}\text{C}^{5+}$. *At Mol Opt Phys*. 2015;48:144032. DOI:10.1088/0953-4075/48/14/144032
- [93] Rau S, Heiße F, Köhler-Langes F, et al. Penning trap mass measurements of the deuteron and the HD^+ molecular ion. *Nature*. 2020;585:43–47. DOI:10.1038/s41586-020-2628-7
- [94] Heiße F, Rau S, Köhler-Langes F, et al. High-precision mass spectrometer for light ions. *Phys Rev A*. 2019;100:022518. DOI:10.1103/PhysRevA.100.022518
- [95] Weinberg S, Lindblad decoherence in atomic clocks. *Phys Rev A*. 2016;94:042117. DOI:10.1103/PhysRevA.94.042117
- [96] Schiller S, Bakalov D, Korobov VI. Simplest molecules as candidates for precise optical clocks. *Phys Rev Lett*. 2014;113. DOI:10.1103/PhysRevLett.113.023004
- [97] Karr J-P. H_2^+ and HD^+ : candidates for a molecular clock. *J Mol Spectrosc*. 2014;300:37–43. DOI:10.1016/j.jms.2014.03.016
- [98] Schmidt PO, Rosenband T, Langer C, et al. Spectroscopy using quantum logic. *Science*. 2005;309:749–752. DOI:10.1126/science.1114375
- [99] Myers EG. CPT tests with the antihydrogen molecular ion. *Phys Rev A*. 2018;98:010101. DOI:10.1103/PhysRevA.98.010101
- [100] Sinhal M, Meir Z, Najafian K, et al. Quantum-nondemolition state detection and spectroscopy of single trapped molecules. *Science*. 2020;367:1213–1218. DOI:10.1126/science.aaz9837
- [101] Schmidt J, Louvradoux T, Heinrich J, et al. Trapping, cooling, and photodissociation analysis of state-selected H_2^+ ions produced by $(3 + 1)$ multiphoton ionization. *Phys Rev Appl*. 2020;14:024053. DOI:10.1103/PhysRevApplied.14.024053
- [102] Filin AA, Möller D, Baru V, et al. High-accuracy calculation of the deuteron charge and quadrupole form factors in chiral effective field theory. *Phys Rev C*. 2021;103:024313. DOI:10.1103/PhysRevC.103.024313
- [103] Vanasse J. Triton charge radius to next-to-next-to-leading order in pionless effective field theory. *Phys Rev C*. 2017;95:024002. DOI:10.1103/PhysRevC.95.024002
- [104] Filin A. private comm. 2023. Available at <https://indico.uis.no/event/2/contributions/523/>
- [105] Lange R, Huntemann N, Rahm JM, et al. Improved Limits for Violations of Local Position Invariance from Atomic Clock Comparisons. *Phys Rev Lett*. 2021;126:011102. DOI:10.1103/PhysRevLett.126.011102
- [106] Schiller S. Hydrogenlike Highly Charged Ions for Tests of the Time Independence of Fundamental Constants. *Phys. Rev. Lett*. 2007;98:180801. DOI:10.1103/PHYSREVLETT.98.180801
- [107] Dehmelt H. Economic synthesis and precision spectroscopy of anti-molecular hydrogen ions in Paul trap. *Phys Scr*. 1995;T59:423–423. DOI:10.1088/0031-8949/1995/t59/060
- [108] Zammit MC, Charlton M, Jonsell S, et al. Laser-driven production of the antihydrogen molecular ion. *Phys Rev A*. 2019;100:042709. DOI:10.1103/PhysRevA.100.042709

1
2
3
4
5
6

Supplemental Material for: Precision spectroscopy of molecular hydrogen ions: an introduction

7
8
9
10
11

S. Schiller
*Institut für Experimentalphysik, Heinrich-Heine-Universität Düsseldorf, 40225 Düsseldorf, Germany**
(Dated: July 1, 2023)

12

A. Hyperfine structure of HD^+

13
14
15
16

Suitable basis states for diagonalizing the spin hamiltonian are the pure spin (angular momentum) states $|G_1 G_2 F m_F\rangle$. They have well-defined values of \mathbf{G}_1^2 , \mathbf{G}_2^2 , \mathbf{F}^2 , F_z . The spin hamiltonian commutes only with \mathbf{F}^2 and with F_z . In zero magnetic field the energies are degenerate with respect to the magnetic quantum number m_F , so it is not displayed in this section.

17

1. Hyperfine structure in levels having $N = 0$.

18
19

The “rotationless” levels $N = 0$ have the simplest hyperfine structure and are treated as follows. The hyperfine hamiltonian in levels having $N = 0$ and arbitrary v is simply

$$H_{\text{spin}}(v, N = 0) = \mathcal{E}_4(v, N = 0) \mathbf{s}_e \cdot \mathbf{I}_p + \mathcal{E}_5(v, N = 0) \mathbf{s}_e \cdot \mathbf{I}_d.$$

20
21
22

A basis for representing the spin structure are the four pure states $|G_1 G_2 F\rangle : \{|100\rangle, |011\rangle, |111\rangle, |122\rangle\}$. Note the ordering with increasing value of F . The spin structure hamiltonian is given by

$$H_{\text{spin}}(v, 0) = \frac{1}{4} \begin{pmatrix} \mathcal{E}_4 - 4\mathcal{E}_5 & 0 & 0 & 0 \\ 0 & -3\mathcal{E}_4 & -2\sqrt{2}\mathcal{E}_5 & 0 \\ 0 & -2\sqrt{2}\mathcal{E}_5 & \mathcal{E}_4 - 2\mathcal{E}_5 & 0 \\ 0 & 0 & 0 & \mathcal{E}_4 + 2\mathcal{E}_5 \end{pmatrix}$$

23
24
25
26
27

Its diagonalization is trivial: the four spin energies and spin eigenstates can be expressed in elementary form. The eigenenergies are also special cases of those presented in eqs. (1,3,4).

28

2. Hyperfine structure in levels having $N = 1$.

29
30

The basis for expressing the spin structure hamiltonian in matrix form are the 10 pure states that can be obtained by coupling the four angular momenta of electron, proton, deuteron and rotation,

$$\{|010\rangle, |110\rangle, |011\rangle, |101\rangle, |111\rangle, |121\rangle, |012\rangle, |112\rangle, |122\rangle, |123\rangle\}.$$

31
32
33
34
35
36
37

Here, too, the ordering is with increasing F . The spin hamiltonian matrix is given in the Appendix of this Supplemental Material. The matrix is easily diagonalized using standard mathematical software, yielding the spin energies and eigenstates in zero magnetic field. Three eigenenergies and eigenstates can be expressed in elementary form, see below. The energies of all other states are solutions of cubic and quartic equations and cannot be given in elementary form.

38

3. Special states

39
40

Since the basis states are states of well-defined total angular momentum magnitude, $F(F + 1)\hbar^2$, and since the spin hamiltonian commutes with the total angular momentum operator squared \mathbf{F}^2 , the hamiltonian matrix elements

* step.schiller@hhu.de

are nonzero only between pure spin states having equal value of F . (Proof: $[H, \mathbf{F}^2] = 0 \Rightarrow \langle p|[H, \mathbf{F}^2]|p' \rangle = 0 = \langle p'|HF(F+1)|p \rangle - \langle p'|F'(F'+1)H|p \rangle = [F(F+1) - F'(F'+1)]\langle p'|H|p \rangle \Rightarrow \langle p'|H|p \rangle \propto \delta_{FF'}$). The hamiltonian matrix therefore has block form, see tables. This has the consequence that the energies of some spin states can be expressed in relatively simple form [1–3].

(1) For any N , there is only one pure spin state with the maximum angular momentum $F = N + 2$. These may be called “stretched” states. Thus, they do not couple to any other pure spin state; they are eigenstates of the hamiltonian. Their other quantum numbers are $G_1 = 1, G_2 = 2$ and in this case are also exact quantum numbers. The energies of the stretched states were first given by [2],

$$E_{\text{spin}}(v, N, G_1 = 1, G_2 = 2, F = N + 2) = \frac{1}{4}\mathcal{E}_4 + \frac{1}{2}\mathcal{E}_5 + \frac{N}{2}(\mathcal{E}_1 + \mathcal{E}_2 + 2\mathcal{E}_3 - (2N - 1)(\mathcal{E}_6 + 2\mathcal{E}_7 + 2\mathcal{E}_8 + \mathcal{E}_9)). \quad (1)$$

These levels have been addressed in the experiments in refs. [4–6].

(2) For $N \neq 1$, there exists another pure spin state that is an eigenstate of the hamiltonian. It is the pure state with *minimum* angular momentum $F = N - 2$ or, if $N = 0$, $F = 0$. It might be called “folded” state. Its energy is

$$E_{\text{spin}}(v, N \geq 2, G_1 = 1, G_2 = 2, F = N - 2) = \frac{1}{4}\mathcal{E}_4 + \frac{1}{2}\mathcal{E}_5 - \frac{1}{2}(N + 1) \times (\mathcal{E}_1 + \mathcal{E}_2 + 2\mathcal{E}_3 + (2N + 3)(\mathcal{E}_6 + 2\mathcal{E}_7 + 2\mathcal{E}_8 + \mathcal{E}_9)), \quad (2)$$

$$E_{\text{spin}}(v, N = 0, G_1 = 1, G_2 = 0, F = 0) = \frac{1}{4}\mathcal{E}_4 - \mathcal{E}_5. \quad (3)$$

Here, G_1 and G_2 are also exact quantum numbers. The level (3) has been addressed in the experiments in refs. [4, 5]. The pure states (1), (2) were already pointed out in ref. [7], within the framework of an approximate spin hamiltonian. A consequence of the expressions is that there are two types of favored E1 transitions whose spin frequency contribution has a simple form, a linear function of the spin hamiltonian coefficients,

$$|v, N, G_1 = 1, G_2 = 2, F = N + 2\rangle \leftrightarrow |v', N' = N + 1, G'_1 = 1, G'_2 = 2, F' = N' + 2\rangle, \text{ all } N, \\ |v, N, G_1 = 1, G_2 = 2, F = N - 2\rangle \leftrightarrow |v', N' = N + 1, G'_1 = 1, G'_2 = 2, F' = N' - 2\rangle, N \geq 2.$$

The first is a stretched-states transition (addressed in the experiments in refs. [5, 6]), the second is a folded-states transition.

(3) For $N = 0(1)$ levels there is one value of F that is taken on by two pure spin states: $F = 1(0)$. This means that the hamiltonian matrix contains one 2×2 block, which describes the coupling between the pure spin states, see the hamiltonian matrices. The eigenvalues of this block give two eigenenergies and eigenstates as solutions of a quadratic equation. They were first given in in Ref. [2] for $N = 0$ and are here generalized for $N = 1$,

$$E_{\text{spin}}(v, N = 0(1), G_1 = 0, G_2 = 1, F = 1(0)) = \frac{1}{2} \left(E_{11} + E_{22} - \sqrt{E_{11}^2 - 2E_{11}E_{22} + 4E_{12}^2 + E_{22}^2} \right), \\ E_{\text{spin}}(v, N = 0(1), G_1 = 1, G_2 = 1, F = 1(0)) = \frac{1}{2} \left(E_{11} + E_{22} + \sqrt{E_{11}^2 - 2E_{11}E_{22} + 4E_{12}^2 + E_{22}^2} \right), \\ E_{11} = -2\mathcal{E}_3 - \frac{3}{4}\mathcal{E}_4 - 5\mathcal{E}_9, \\ E_{22} = \frac{1}{4}(-2\mathcal{E}_1 - 2\mathcal{E}_2 - 4\mathcal{E}_3 + \mathcal{E}_4 - 2\mathcal{E}_5 + 10\mathcal{E}_6 - 20\mathcal{E}_7 - 20\mathcal{E}_8 + 10\mathcal{E}_9), \\ E_{12} = \frac{1}{\sqrt{2}}(\mathcal{E}_1 - \mathcal{E}_2 - \mathcal{E}_5 + 5\mathcal{E}_7 - 5\mathcal{E}_8). \quad (4)$$

(For $N = 0$, only \mathcal{E}_4 and \mathcal{E}_5 are nonzero). These levels have been addressed in the experiments in refs. [4, 5, 8].

B. Zeeman effect in HD⁺

The interaction of the molecule with a magnetic field B aligned with the z axis is approximately given by

$$H_{\text{Zeeman}}(v, N) = -(g_e s_{ez} + g_p I_{p,z} + g_d I_{d,z} + g_l(v, N)N_z)\mu_B B,$$

neglecting additional terms [9]. The last term describes (if $N > 0$) the effect of a magnetic moment induced by molecular rotation. The rotational g-factor $g_l(v, N)$ is nonzero if $N \geq 1$ and is presented in ref. [2]. It is weakly v -dependent. The signs are as follows: μ_B , g_p , g_d , g_l are positive, $g_e \simeq -2$ is negative. The g-factors of proton, deuteron and nuclear rotation are small, of order m_e/m_p .

In first approximation one can use for g_e , g_p , g_d the values of the free particles. For a precision calculation one must take into account that the electron is bound and that the proton and deuteron are shielded by the electron cloud. The g-factor of an electron bound to the MHI and the shielding has been approximately evaluated in ref. [9]. The main correction is a reduction of the free-space g-factor by approximately 2×10^{-5} fractionally, where the reduction is also (weakly) dependent on the rovibrational state (v, N) .

The Zeeman splitting of the spin structure is found by adding spin and Zeeman hamiltonians. Even in the presence of a magnetic field, we may still use the basis introduced earlier, but extended to include the magnetic quantum number. (An altogether different basis could also be used.) The total hamiltonian does not commute any more with \mathbf{F}^2 , but only with F_z . Therefore, the total hamiltonian does not have matrix elements between basis states having different value of magnetic quantum number m_F . Thus, to find the spin structure in a nonzero magnetic field B one proceeds to compute separately the eigenenergies and eigenstates for each value of m_F .

1. Zeeman effect in levels having $N = 0$.

For each value of $m_F = -F_{\text{max}}, \dots, +F_{\text{max}} = -2, \dots, 2$, the basis states are

$$|G_1 G_2 F m_F\rangle = \{|100m_F\rangle, |011m_F\rangle, |111m_F\rangle, |122m_F\rangle\},$$

where one drops from the list those states where $F < |m_F|$.

The above spin structure hamiltonian also applies to this basis, and is independent of m_F . The Zeeman hamiltonian corresponding to a particular m_F is $H_{\text{Zeeman}}(N = 0, m_F) = \mu_B B h(0, m_F)$, with the appropriate columns and rows dropped. The h are as follows:

$$h(0, 0) = \frac{1}{2\sqrt{3}} \begin{pmatrix} 0 & g_p - g_e & \sqrt{2}(-2g_d + g_e + g_p) & 0 \\ g_p - g_e & 0 & 0 & \sqrt{2}(g_e - g_p) \\ \sqrt{2}(-2g_d + g_e + g_p) & 0 & 0 & -2g_d + g_e + g_p \\ 0 & \sqrt{2}(g_e - g_p) & -2g_d + g_e + g_p & 0 \end{pmatrix}$$

$$h(0, 1) = \frac{1}{4} \begin{pmatrix} 0 & 0 & 0 & 0 \\ 0 & -4g_d & \sqrt{2}(g_e - g_p) & \sqrt{2}(g_e - g_p) \\ 0 & \sqrt{2}(g_e - g_p) & -2g_d - g_e - g_p & -2g_d + g_e + g_p \\ 0 & \sqrt{2}(g_e - g_p) & -2g_d + g_e + g_p & -2g_d - g_e - g_p \end{pmatrix}$$

$$h(0, -1) = \frac{1}{4} \begin{pmatrix} 0 & 0 & 0 & 0 \\ 0 & 4g_d & \sqrt{2}(g_p - g_e) & \sqrt{2}(g_e - g_p) \\ 0 & \sqrt{2}(g_p - g_e) & 2g_d + g_e + g_p & -2g_d + g_e + g_p \\ 0 & \sqrt{2}(g_e - g_p) & -2g_d + g_e + g_p & 2g_d + g_e + g_p \end{pmatrix}$$

$$h(0, 2) = \frac{1}{2} \begin{pmatrix} 0 & 0 & 0 & 0 \\ 0 & 0 & 0 & 0 \\ 0 & 0 & 0 & 0 \\ 0 & 0 & 0 & -2g_d - g_e - g_p \end{pmatrix}$$

$$h(0, -2) = \frac{1}{2} \begin{pmatrix} 0 & 0 & 0 & 0 \\ 0 & 0 & 0 & 0 \\ 0 & 0 & 0 & 0 \\ 0 & 0 & 0 & 2g_d + g_e + g_p \end{pmatrix}$$

There is no dependence of v , since g_l does not appear if $N = 0$.

76 In the case $m_F = 0$, one diagonalizes $H_{\text{spin}}(v, 0) + \mu_B B h(0, 0)$, a 4×4 matrix.

77 For $m_F = \pm 1$, one considers the subspace formed by the basis states having $F \geq 1$, i.e. one drops the first row and
78 first column of the matrix $H_{\text{spin}}(v, 0) + \mu_B B h(0, \pm 1)$, since they correspond to the basis state $|G_1 G_2 F\rangle = |100\rangle$ that
79 can only have the $m_F = 0$ Zeeman component.

80 The next case is $m_F = \pm 2$, and one drops the first three rows and columns. This case also corresponds to
81 $m_F = \pm \text{Max}(F)$. In general (i.e. also for nonzero N) the spin plus Zeeman hamiltonian matrix is then just a 1×1
82 matrix, and thus the matrix element is the corresponding eigenenergy. The Zeeman shift is strictly linear. The
83 eigenstates are the stretched states.

84 Figure 1 presents the Zeeman effect for the case $v = 0$.

85 2. Zeeman effect in levels having $N = 1$

86 The computation of the eigenstates in nonzero magnetic field proceeds analogously to the case $N = 0$: when
87 treating the case $|m_F|$ one drops those rows and columns from the matrix sum $H_{\text{spin}}(v, N = 1) + \mu_B B h(v, 1, m_F)$
88 corresponding to $F < |m_F|$. The matrices $h(v, 1, m_F)$ are given in the Appendix of this Supplemental Material. They
89 are v -dependent, since they involve g_l .

90 The total hamiltonian is easily diagonalized using standard mathematical software. The Zeeman shift is strictly
91 linear for the stretched states $|G_1 = 1, G_2 = 2, F = 3, m_F = \pm 3\rangle$.

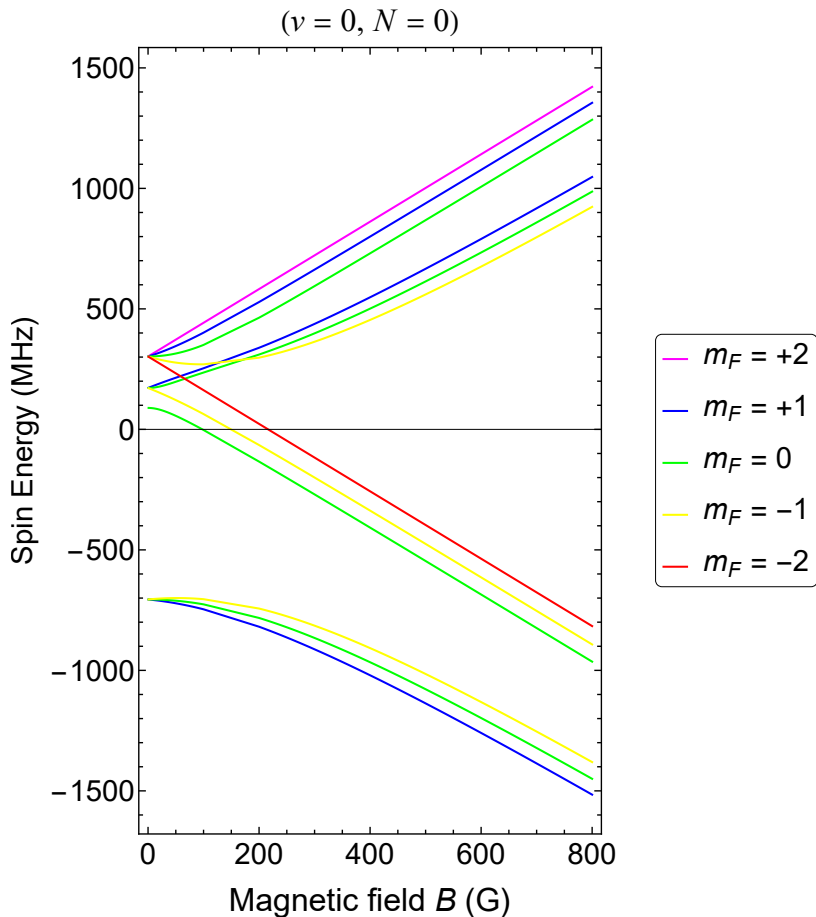


FIG. 1. The spin structure of HD^+ in the ground rovibrational level $v = 0, N = 0$. Red and magenta curves are the stretched states.

C. Hyperfine structure of H_2^+

The hyperfine structure is simpler than that of HD^+ . The spin hamiltonian contains 5 spin coefficients that have been calculated *ab initio* [10]. The general hamiltonian matrix can be found in explicit form in ref. [1]. Eigenstates and eigenenergies are discussed at some length in ref. [11].

In any rovibrational level, the most appropriate basis are the pure angular momentum states $|IGFm_F\rangle$, with fixed value of the total nuclear spin I , definite values of coupled electron spin and total nuclear spin G , and the total angular momentum of the molecule $F = \text{Max}(\{|G - N|, 0\}), \dots, G + N$. Consider first the absence of magnetic field, hence we drop the quantum number m_F .

For even N (para- H_2^+) the spin structure is particularly simple (Fig. 6 of main text): the total nuclear spin has to vanish, $I = 0$. We then have the analog of the well-known problem of the hyperfine structure of an atom with an electronic spin doublet configuration: a single electron spin coupling to another angular momentum. In the present case it is not a nuclear spin but a (integer only) rotational angular momentum.

If $N = 0$ there results a single spin state, $|I = 0, G = 1/2, F = 1/2\rangle$ and the spin energy is zero.

Otherwise, the hamiltonian simplifies to $H_{\text{spin}}(v, N > 0, \text{even}) = c_e(v, N \text{ even}) \mathbf{s}_e \cdot \mathbf{N}$. There are only two pure basis states, $|I = 0, G = 1/2, F = N \pm 1/2\rangle$. The spin hamiltonian is already diagonal in this basis (see listing below). The energies are given by the simple expressions

$$E_{\text{spin}}(v, N \geq 2, G = \frac{1}{2}, F = N - \frac{1}{2}) = -\frac{N+1}{2}c_e,$$

$$E_{\text{spin}}(v, N \geq 2, G = \frac{1}{2}, F = N + \frac{1}{2}) = \frac{N}{2}c_e.$$

For odd N (ortho- H_2^+), the situation is slightly more intricate. The basis states are $|I = 1, G = 1/2, F = N \pm 1/2\rangle$, $|I = 1, G = 3/2, F = N \pm 1/2\rangle$, $|I = 1, G = 3/2, F = N \pm 3/2\rangle$. They are six in number except in the case $N = 1$, where there are only five. The hamiltonian matrix is block diagonal, with two diagonal entries and two 2×2 blocks. Thus, two hyperfine states (or one if $N = 1$), including the stretched state $F = N + 3/2$, are pure angular momentum states and have energies that are linear functions of the spin coefficients, and four are solutions of two quadratic equations. The explicit expressions for the energies appear to have first been given in ref. [12].

D. Zeeman effect in para- H_2^+

115
116 The treatment is particularly simple for even N [13]. The approximate Zeeman hamiltonian is

$$H_{\text{Zeeman}}(v, N \text{ even}) = -(g_e s_{e,z} + g_l(v, N) N_z) \mu_B B ,$$

117 with the same nomenclature as for HD^+ . Except in $N = 0$ levels, it is v -dependent. The values for the g-factors are
118 given in refs. [9, 13]. The total hamiltonian in finite magnetic field B is the sum $H_{\text{spin}}(v, N \text{ even}) + H_{\text{Zeeman}}(v, N \text{ even})$.
119 It commutes with F_z . The matrix hamiltonians for different values of magnetic quantum number m_F are listed below.
120 Rows and columns refer to the two states $|0, 1/2, N - 1/2, m_F\rangle, |0, 1/2, N + 1/2, m_F\rangle$. Eigenvalues and eigenstates
121 are trivially found. Figure 2 displays an example of the spin structure.

m_F	$H_{\text{spin}}(v, N = 0)/c_e(v, N = 0)$	$H_{\text{Zeeman}}(v, N = 0, m_F)/(\mu_B B)$
$-\frac{1}{2}$	0	$\frac{g_e}{2}$
$\frac{1}{2}$	0	$-\frac{g_e}{2}$

m_F	$H_{\text{spin}}(v, N = 2)/c_e(v, N = 2)$	$H_{\text{Zeeman}}(v, N = 2, m_F)/(\mu_B B)$
$-\frac{5}{2}$	1	$\frac{1}{2}(g_e + 4g_l)$
$-\frac{3}{2}$	$\begin{pmatrix} -\frac{3}{2} & 0 \\ 0 & 1 \end{pmatrix}$	$\frac{1}{10} \begin{pmatrix} -3(g_e - 6g_l) & 4(g_e - g_l) \\ 4(g_e - g_l) & 3(g_e + 4g_l) \end{pmatrix}$
$-\frac{1}{2}$	$\begin{pmatrix} -\frac{3}{2} & 0 \\ 0 & 1 \end{pmatrix}$	$\frac{1}{10} \begin{pmatrix} 6g_l - g_e & 2\sqrt{6}(g_e - g_l) \\ 2\sqrt{6}(g_e - g_l) & g_e + 4g_l \end{pmatrix}$
$\frac{1}{2}$	$\begin{pmatrix} -\frac{3}{2} & 0 \\ 0 & 1 \end{pmatrix}$	$\frac{1}{10} \begin{pmatrix} g_e - 6g_l & 2\sqrt{6}(g_e - g_l) \\ 2\sqrt{6}(g_e - g_l) & -g_e - 4g_l \end{pmatrix}$
$\frac{3}{2}$	$\begin{pmatrix} -\frac{3}{2} & 0 \\ 0 & 1 \end{pmatrix}$	$\frac{1}{10} \begin{pmatrix} 3(g_e - 6g_l) & 4(g_e - g_l) \\ 4(g_e - g_l) & -3(g_e + 4g_l) \end{pmatrix}$
$\frac{5}{2}$	1	$\frac{1}{2}(-g_e - 4g_l)$

m_F	$H_{\text{spin}}(v, N = 4)/c_e(v, N = 4)$	$H_{\text{Zeeman}}(v, N = 4, m_F)/(\mu_B B)$
$-\frac{9}{2}$	2	$\frac{1}{2}(g_e + 8g_l)$
$-\frac{7}{2}$	$\begin{pmatrix} -\frac{5}{2} & 0 \\ 0 & 2 \end{pmatrix}$	$\frac{1}{18} \begin{pmatrix} 70g_l - 7g_e & 4\sqrt{2}(g_e - g_l) \\ 4\sqrt{2}(g_e - g_l) & 7(g_e + 8g_l) \end{pmatrix}$
$-\frac{5}{2}$	$\begin{pmatrix} -\frac{5}{2} & 0 \\ 0 & 2 \end{pmatrix}$	$\frac{1}{18} \begin{pmatrix} 50g_l - 5g_e & 2\sqrt{14}(g_e - g_l) \\ 2\sqrt{14}(g_e - g_l) & 5(g_e + 8g_l) \end{pmatrix}$
$-\frac{3}{2}$	$\begin{pmatrix} -\frac{5}{2} & 0 \\ 0 & 2 \end{pmatrix}$	$\frac{1}{6} \begin{pmatrix} 10g_l - g_e & 2\sqrt{2}(g_e - g_l) \\ 2\sqrt{2}(g_e - g_l) & g_e + 8g_l \end{pmatrix}$
$-\frac{1}{2}$	$\begin{pmatrix} -\frac{5}{2} & 0 \\ 0 & 2 \end{pmatrix}$	$\frac{1}{18} \begin{pmatrix} 10g_l - g_e & 4\sqrt{5}(g_e - g_l) \\ 4\sqrt{5}(g_e - g_l) & g_e + 8g_l \end{pmatrix}$
$\frac{1}{2}$	$\begin{pmatrix} -\frac{5}{2} & 0 \\ 0 & 2 \end{pmatrix}$	$\frac{1}{18} \begin{pmatrix} g_e - 10g_l & 4\sqrt{5}(g_e - g_l) \\ 4\sqrt{5}(g_e - g_l) & -g_e - 8g_l \end{pmatrix}$
$\frac{3}{2}$	$\begin{pmatrix} -\frac{5}{2} & 0 \\ 0 & 2 \end{pmatrix}$	$\frac{1}{6} \begin{pmatrix} g_e - 10g_l & 2\sqrt{2}(g_e - g_l) \\ 2\sqrt{2}(g_e - g_l) & -g_e - 8g_l \end{pmatrix}$
$\frac{5}{2}$	$\begin{pmatrix} -\frac{5}{2} & 0 \\ 0 & 2 \end{pmatrix}$	$\frac{1}{18} \begin{pmatrix} 5(g_e - 10g_l) & 2\sqrt{14}(g_e - g_l) \\ 2\sqrt{14}(g_e - g_l) & -5(g_e + 8g_l) \end{pmatrix}$
$\frac{7}{2}$	$\begin{pmatrix} -\frac{5}{2} & 0 \\ 0 & 2 \end{pmatrix}$	$\frac{1}{18} \begin{pmatrix} 7(g_e - 10g_l) & 4\sqrt{2}(g_e - g_l) \\ 4\sqrt{2}(g_e - g_l) & -7(g_e + 8g_l) \end{pmatrix}$
$\frac{9}{2}$	2	$\frac{1}{2}(-g_e - 8g_l)$

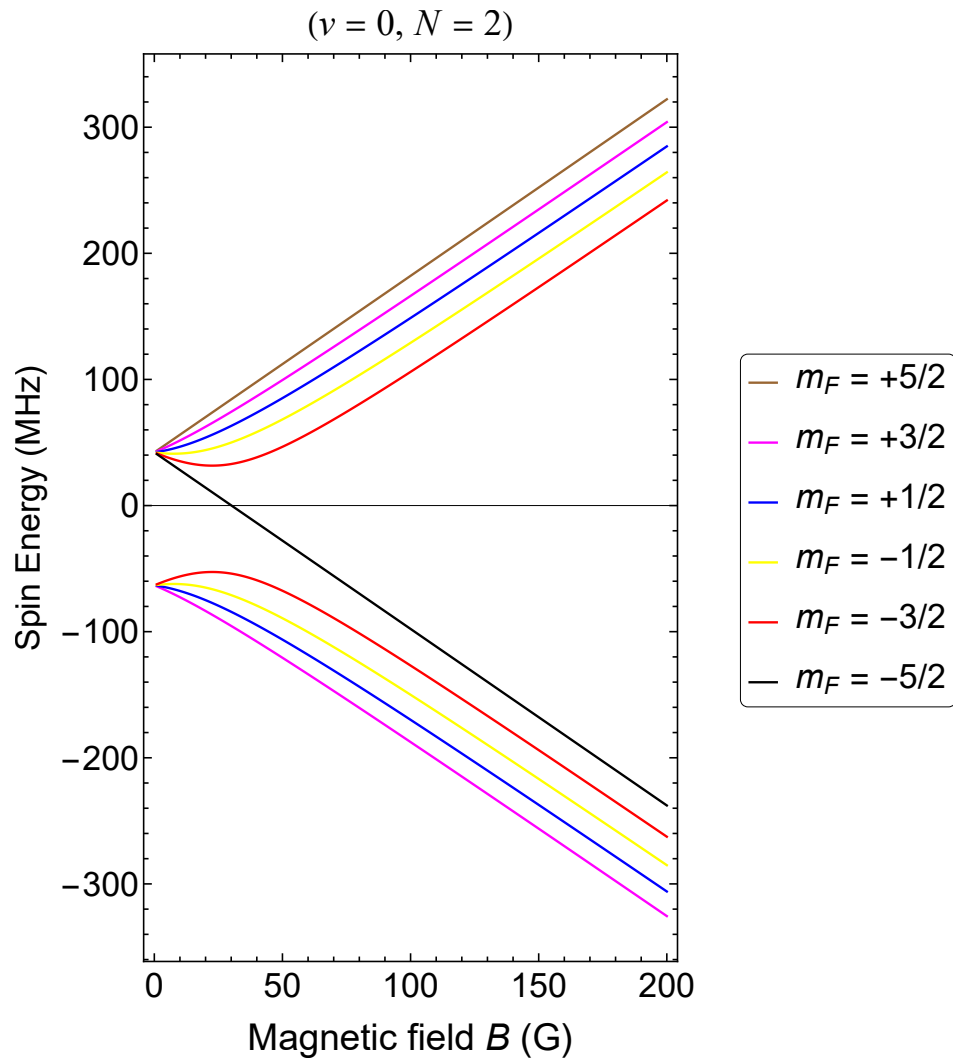


FIG. 2. The spin structure of para- H_2^+ in the rovibrational level $v = 0, N = 2$. Black and brown curves are the stretched states.

-
- 133 [1] J.-P. Karr, F. Bielsa, A. Douillet, J. Pedregosa Gutierrez, V. I. Korobov, L. Hilico, Vibrational spectroscopy of H_2^+ :
134 Hyperfine structure of two-photon transitions, *Phys. Rev. A* 77 (2008) 063410. doi:10.1103/PhysRevA.77.063410.
- 135 [2] D. Bakalov, V. Korobov, S. Schiller, Magnetic field effects in the transitions of the HD^+ molecular ion and precision
136 spectroscopy, *J. Phys. B: At. Mol. Opt. Phys.* 44 (2011) 025003. doi:10.1088/0953-4075/44/2/025003.
- 137 [3] P. Danev, D. Bakalov, V. I. Korobov, S. Schiller, Hyperfine structure and electric quadrupole transitions in the deuterium
138 molecular ion, *Phys. Rev. A* 103 (2021) 012805. doi:10.1103/PhysRevA.103.012805.
- 139 [4] U. Bressel, A. Borodin, J. Shen, M. Hansen, I. Ernsting, S. Schiller, Manipulation of individual hyperfine states in
140 cold trapped molecular ions and application to HD^+ frequency metrology, *Phys. Rev. Lett.* 108 (2012) 183003. doi:
141 10.1103/PhysRevLett.108.183003.
- 142 [5] S. Alighanbari, G. S. Giri, F. L. Constantin, V. I. Korobov, S. Schiller, Precise test of quantum electrodynamics and
143 determination of fundamental constants with HD^+ ions, *Nature* 581 (2020) 152 – 158. doi:10.1038/s41586-020-2261-5.
- 144 [6] I. V. Kortunov, S. Alighanbari, M. G. Hansen, G. S. Giri, V. I. Korobov, S. Schiller, Proton-electron mass ratio by
145 high-resolution optical spectroscopy of ion ensembles in the resolved-carrier regime, *Nat. Phys.* 17 (2021) 569–573. doi:
146 10.1038/s41567-020-01150-7.
- 147 [7] A. Carrington, R. A. Kennedy, Vibration-rotation spectroscopy of the HD^+ ion near the dissociation limit. III. Measure-
148 ments of the $v = 17 - 15$ and $20 - 17$ bands: demonstration of an asymmetric electron distribution, *Molecular Physics* 56
149 (1985) 935–975. doi:10.1080/00268978500102821.
- 150 [8] S. Alighanbari, I. V. Kortunov, G. S. Giri, S. Schiller, Test of charged baryon interaction with high-resolution vibrational
151 spectroscopy of molecular hydrogen ions, *Nat. Phys.* (2023). doi:10.1038/s41567-023-02088-2.
- 152 [9] R. A. Hegstrom, g factors and related magnetic properties of molecules. Formulation of theory and calculations for H_2^+ ,
153 HD^+ , and D_2^+ , *Phys. Rev. A* 19 (1979) 17–30. doi:10.1103/PhysRevA.19.17.
- 154 [10] V. I. Korobov, L. Hilico, J.-P. Karr, Hyperfine structure in the hydrogen molecular ion, *Phys. Rev. A* 74 (2006) 040502.
155 doi:10.1103/PhysRevA.74.040502.
- 156 [11] V. I. Korobov, P. Danev, D. Bakalov, S. Schiller, Laser-stimulated electric quadrupole transitions in the molecular hydrogen
157 ion H_2^+ , *Phys. Rev. A* 97 (2018) 032505. doi:10.1103/PhysRevA.97.032505.
- 158 [12] D. A. Varshalovich, A. V. Sannikov, Molecular H_2^+ ions in the interstellar medium, *Astronomy Letters* 19 (1993) 290–293.
159 URL <http://articles.adsabs.harvard.edu/pdf/1993AstL...19..290V>
- 160 [13] J.-P. Karr, V. I. Korobov, L. Hilico, Vibrational spectroscopy of H_2^+ : Precise evaluation of the Zeeman effect, *Phys. Rev.*
161 *A* 77 (2008) 062507. doi:10.1103/PhysRevA.77.062507.